Université de Toulouse

THÈSE

En vue de l'obtention du

DOCTORAT DE L'UNIVERSITÉ DE TOULOUSE

Délivré par **l'Institut Supérieur de l'Aéronautique et de l'Espace**
Spécialité : Optoélectronique et hyperfréquence

Présentée et soutenue par **Ahmad Akhtar HAYAT**
le 12 octobre 2009

Verrouillage optique des VCSELs émettant à 1.3µm et à 1.5µm : expériences et modélisation

Optical Injection-Locking of 1.3µm and 1.5µm VCSELs : experiments and Modeling

---

JURY

M. Eli Kapon, président du jury
M. Pascal Besnard, rapporteur
M. Philippe Gallion, rapporteur
M. Jean-Claude Mollier, co-directeur de thèse
Mme Angélique Rissons, directrice de thèse
M. Henry White

École doctorale : **Génie électrique, électronique et télécommunications**

Unité de recherche : **Équipe d'accueil ISAE-ONERA OLIMPES**

Directrice de thèse : **Mme Angélique Rissons**
Co-directeur de thèse : **M. Jean-Claude Mollier**

Optical Injection-Locking of 1.3μm and 1.5μm VCSELs: Experiments and Modeling

Ahmad HAYAT

November 5, 2009

Contents

List of Figures

List of Tables

Introduction

Since the telecommunication revolution in the early 90s, that saw massive deployment of optical fiber for high bit rate communications, coherent optical sources have made tremendous technological advances. The technological improvement has been multi dimensional; component sizes have been reduced, conversion efficiencies increased, power consumptions decreased and integrability into compact optoelectronic sub-modules improved. Semiconductor lasers, emitting in the 1.1-1.6 μm range, have been the most prominent beneficiaries of these technological advances. This progress is a result of research efforts, that consistently came up with innovative solutions and components, to meet the market demand. This in-phase, demand and supply, problem and solution and consumer need and innovation cycle, has ushered us in to the present information technology era, where stable high speed data links make the backbone of almost every aspect of life, from economy to entertainment and from health sector to defense production.

By the start of twenty-first century, a new, low cost, low power consumption and miniaturized generation of lasers had started to capture its own market share. These lasers, named Vertical-Cavity Surface-Emitting Lasers (VCSELs) due to the presence of an optical cavity which is normal to the fabrication plane , have established themselves as premier optical sources in short-haul communications such as Gigabit ethernet, in optical computing architectures and in optical sensors. While shorter wavelength VCSEL ($< 1\mu$m) fabrication technology was readily mastered, due to the ease in manipulation of AlGaAs-based materials, long wavelength VCSELs especially VCSELs emitting in the 1.3-1.5 μ range have encountered several technical challenges. There importance as low-cost coherent optical sources for the telecommunication systems is primordial, since they are compatible with the existing infrastructure.

VCSEL utilization in low-cost systems imply the application of direct modulation for high bit rate data transmission which engenders the problems of frequency chirping which increases laser linewidth and severely limits the system performance. Furthermore, relatively lower VCSEL intrinsic cut-off frequencies translated in to impossibility of achieving high bit rates. Optical injection-locking is proposed as a solution to these problems. It enhances the intrinsic component bandwidth and reduces frequency chirp considerably [1].

The motivation of this research work is the demonstration of long wavelength VCSEL optical injection-locking phenomena under different varying system parameters and conditions. The research work was undertaken in the context of a European project in collaboration with Ecole Polytechnique Fédérale de Lausanne (EPFL), D-Lightsys, a French company which specializes in optical sub-assembly integration and BeamExpress, a Swiss VCSEL fabrication spin-off. Most of the VCSELs used in the injection-locking experiments in the course of this work have been provided by BeamExpress [2]. VCSELs fabricated by the South Korean manufacturer RayCan have also been employed [3]. The experimental studies have been complemented by undertaking the development of a comprehensive, VCSEL intrinsic parameter-based mathematical model. The experimental results and the mathematical model have been used simultaneously to investigate optical injection-locking phenomena.

The first chapter introduces the historical background on optical injection-locking. It then explains the evolution of optical injection-locking experiments and techniques since the discovery of laser itself. Optical injection-locking in the context of in-plane lasers is then introduced which then logically leads to the optical injection-locking of VCSELs. Several different applications of VCSEL optical injection-locking vis à vis its different operation regimes are then discussed.

The second chapter is dedicated to the mathematical modeling of optically injection-locked VCSELs. A modified rate-equation based mathematical model is presented. This model uses the VCSEL intrinsic parameters values to calculate the system frequency response. System S_{21} response under various injection conditions as well as for different frequency detuning values have been investigate. Stable VCSEL optical injection-locking operation range, in terms of detuning frequency and injected optical power, have been calculated. A comparison between free-running and injection-locked VCSEL models has also been presented.

The third chapter deals with the experimental studies of optically injection-locked VCSELs. Results obtained by the optical injection-locking of on-chip VCSELs have been presented. Several different operation regimes have been investigated. Finally a comparison between the injection-locking measurements and the simulations developed in the second chapter is presented.

The fourth chapter deals with the injection-locking of fibered VCSELs and the Relative Intensity Noise (RIN) of VCSELs. An extraction methodology has been developed in order to extract the component S_{21} response from the noisy system response. This methodology is implemented on both free-running and injection-locked VCSELs. RIN measurements of free-running and injection-locked VCSELs have been presented. RIN measurements have been used to observe the resonance peaks of fibered VCSELs which were otherwise unobservable. A comparison of free-running and injection-locked VCSEL RINs is presented.

Bibliography

[1] C.-H. Chang, L. Chrostowski, and C. Chang-Hasnain, "Injection locking of VCSELs," *IEEE Journal of Selected Topics in Quantum Electronics*, vol. 9, no. 5, pp. 1386–1393, Sept.-Oct. 2003.

[2] V. Iakovlev, G. Suruceanu, A. Caliman, A. Mereuta, A. Mircea, C.-A. Berseth, A. Syrbu, A. Rudra, and E. Kapon, "High-Performance Single-Mode VCSELs in the 1310-nm Waveband," *IEEE Photonics Technology Letters*, vol. 17, no. 5, pp. 947–949, May 2005.

[3] M.-R. Park, O.-K. Kwon, W.-S. Han, K.-H. Lee, S.-J. Park, and B.-S. Yoo, "All-epitaxial InAlGaAs-InP VCSELs in the 1.3-1.6-μm Wavelength Range for CWDM Band Applications," *IEEE Photonics Technology Letters*, vol. 18, no. 16, pp. 1717–1719, Aug. 2006.

Chapter 1 Long Wavelength VCSEL Optical Injection-Locking

1.1 Optical Injection Locking

1.1.1 Introduction and Historical Background

In 1665 Christiaan Huygens, the eminent Dutch mathematician, scientist and astronomer, later to become famous for the discovery of Saturn Rings [1], while confined to bed through illness, remarked that the pendulums of two clocks in his bedroom locked synchronously if they were hung close to each other but became free-running when the distance between them was increased. Huygens concluded through this thought experiment that the mechanical vibrations transferred from one clock to the other via the wall were responsible for this synchronization, thus providing the first observation of coupling of two oscillators. One pendulum injected small perturbations through the wall to the other pendulum eventually locking the phase and the frequency of the two pendulums together. Huygens later detailed this idea in his work **"Horologium Oscillatorium"** [1].

Huygens observations provided the basis for locking of mechanical oscillators. Although Huygens did contribute enormously to wave and light propagation theories, he never tried to apply the concepts of mechanical oscillator synchronization to light sources. This can of course be explained by the inexistence, at that time, of electronic and optoelectronic oscillator devices. Approximately 300 years later, in 1946, Adler [2] published his seminal works on the synchronization and therefore locking of two electronic oscillators.

He injection-locked a crystal oscillator with an external frequency source. Adler extrapolated the mechanical oscillator synchronization principles observed by Huygens to the electrical domain. He showed that when an external signal of frequency ω_{ext} is injected into an oscillator with an oscillation frequency of ω_0, the circuit now oscillates at the injected frequency, given that the injected frequency ω_{ext} is close to the natural oscillation frequency ω_0 of the circuit. Injection-Locking of electronic oscillators was thus brought to the fore.

Optical Injection-Locking, however, had to wait another 20 years for its first experimental demonstration. In 1965, Pantell expanded Adler's theory to include a generalized behavioral model for lasers under optical injection-locking mechanisms [3] and finally in 1966

[1] The brighter interior of the "Orion Nebula" bears the name of the **Huygens Region** in his honor.

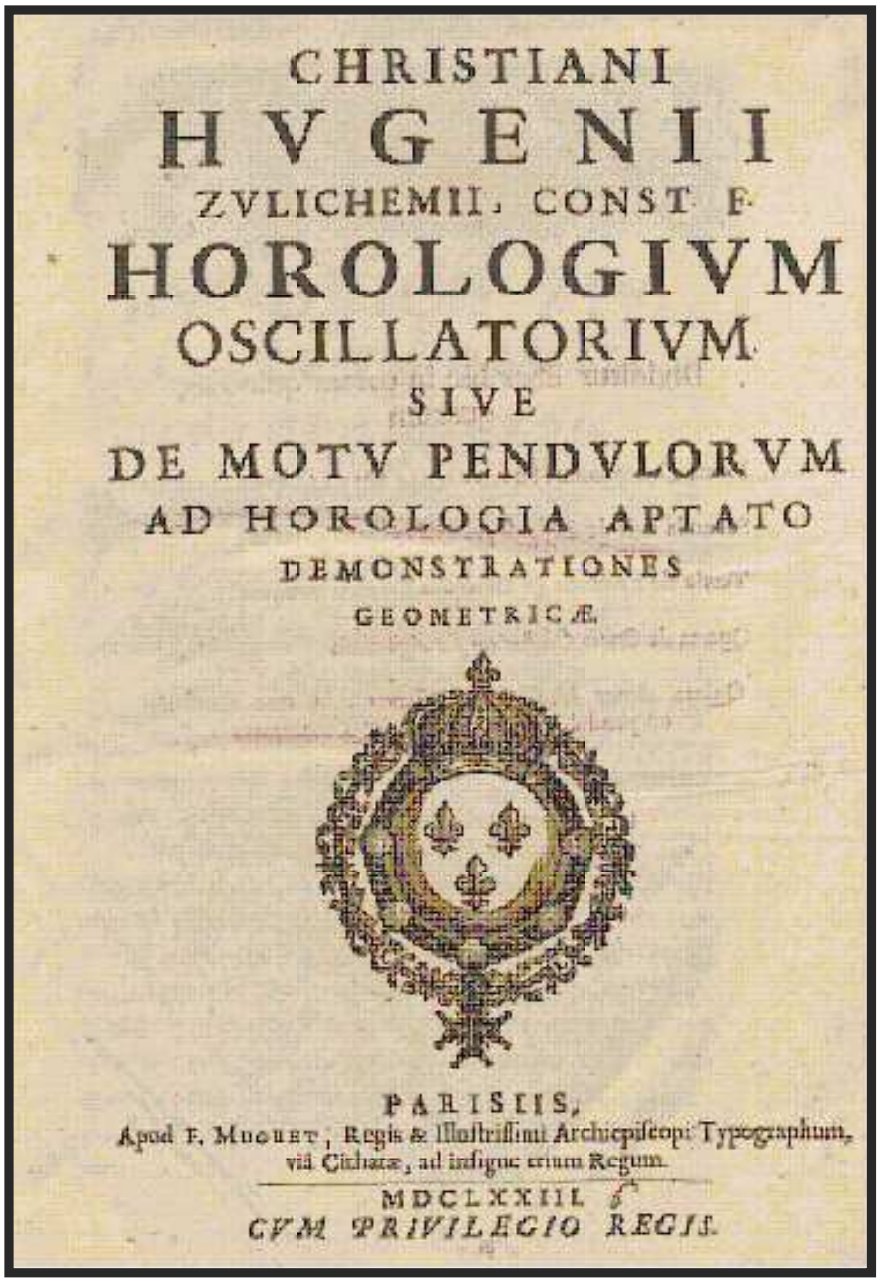
CHRISTIANI
HVGENII
ZVLICHEMII, CONST. F.
HOROLOGIVM
OSCILLATORIVM
SIVE
DE MOTV PENDVLORVM
AD HOROLOGIA APTATO
DEMONSTRATIONES
GEOMETRICÆ.
PARISIIS,
Apud F. MUGUET, Regis & Illustrissimi Archiepiscopi Typographum,
viâ Citharæ, ad insigne trium Regum.
MDCLXXIII.
CVM PRIVILEGIO REGIS.

Figure 1.1: Title of Christiaan Huygens' "Horlogium Oscillatorium": An early 18th century reprint (1723).

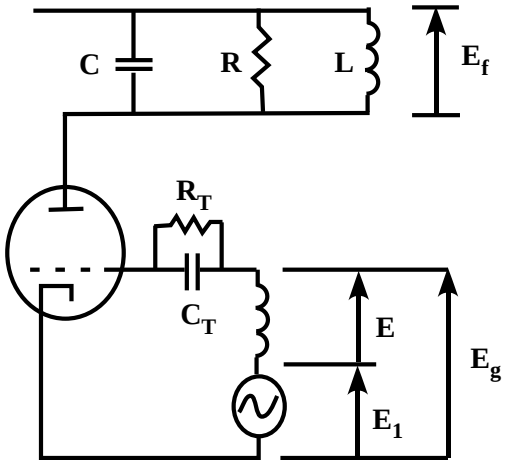

Figure 1.2: Locking setup of two electronic oscillators proposed by Adler.

Stover and Steier demonstrated the optical injection-locking for the first time using two He-Ne lasers emitting in the 650nm range [4]. In this experiment the beam from one He-Ne laser was directly injected into the cavity of another He-Ne laser operating at the same wavelength.

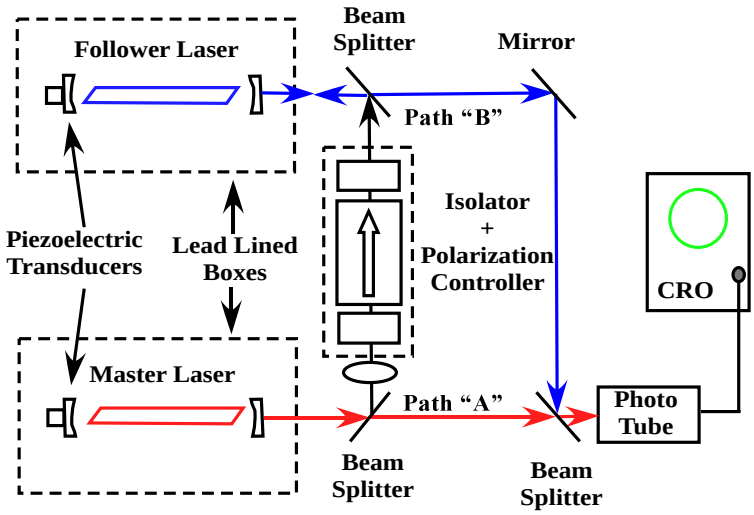

Figure 1.3: The test bench proposed by Stover and Stier for the first Optical Injection-Locking experiment using two He-Ne lasers emitting in the 650nm range.

Optical Injection-Locking, after its first demonstration, slowed down considerably for the next decade. This can be explained by the fact that lasers themselves were incipient at that time and new materials and techniques for laser fabrication were being developed. Furthermore, laser systems used crystals, gases or dyes as gain components which rendered the systems bulky and inefficient. Attempts to injection-lock these optical oscillators were thus few and far between and energies were focused more on the development of compact, lighter and efficient optical sources. Throughout the 70's the progress on the optical injection-

locking remained rather slow. The major emphasis was to apply Stover and Steier's He-Ne optical injection-locking demonstration to other laser systems. In 1972, for example, Buczek and Freiburg demonstrated the optical injection-locking using two CO_2 lasers [5].

The development, arrival and maturation of optical fibers in the mid and late 70's acted as a catalyst for the conception, development and mass fabrication of semiconductor lasers. This opened-up an explosive growth potential in telecommunications and in related fields such as direct and coherent detection. As a consequence of the availability of cheaper, compact and relatively more efficient GaAs and InP based semiconductor lasers, the optical injection-locking research took-off in the 80's. Subsequent to these developments almost all the injection-locking experiments were carried-out using the semiconductor lasers.

The 1980's experienced a rapid development in the optical injection-locking domain. Kobayashi and Kimura revived the injection-locking research when, in 80, they demonstrated for the first time the optical injection-locking using two AlGaAs lasers emitting at 840nm[6]. The 80's also saw an increase in the employment of injection-locking techniques in the coherent detection of modulated optical signals. Coherent detection of a modulated signal was particularly popular throughout the 80's until the discovery of optical fiber amplifiers in the early 90's. The follower laser emission wavelength (and therefore frequency) is fixed due to injection from the master laser. A small variation in the follower laser current therefore changes the locking conditions and causes the master-follower phase difference to shift. This phase-shifting by follower laser current modulation provided a means to establish a phase shift keying (PSK) system using optical injection-locking. In 1982 Kobayashi et al. presented an optical phase modulation scheme in an injection-locked system by modulating the slave laser current [7]. Kasapi later utilised a power enhancement technique using optical injection-locking proposed by Kobayashi and Kimura [8] to develop a sub-shot noise frequency modulation spectroscopy technique [9].

In 1985, Gallion et.al presented a thorough experimental study complemented with a theoretical analysis of the reduction in linewidth of injection-locked lasers [10]. Fig.1.4 shows the measured linewidth against the laser's reciprocal output power both the free-running and injection-locked states. It can be argued intuitively that since one of the properties of an optically injection-locked system is the locking of follower laser emission to the master laser, optical injection-locking might help reduce the chirp introduced in directly modulated laser diodes by holding the slave laser frequency close to the master laser frequency. Lin and Mengel effectively demonstrated the chirp reduction in 1984 [11] by the application of this principle. A year later, in 1985, Olsson et al. further applied this discovery to demonstrate chirp-free transmission over a distance of 82.5 km at a rate of 2 Gbps to achieve a then record BandWidth-Length (B-L) product with single mode injection-locked semiconductor lasers [12]. A simultaneous demonstration of an injection-locked 2.2 Gbps system by multiplexing four 560 Mbps channels was presented by Lin et al. shortly afterward [13].

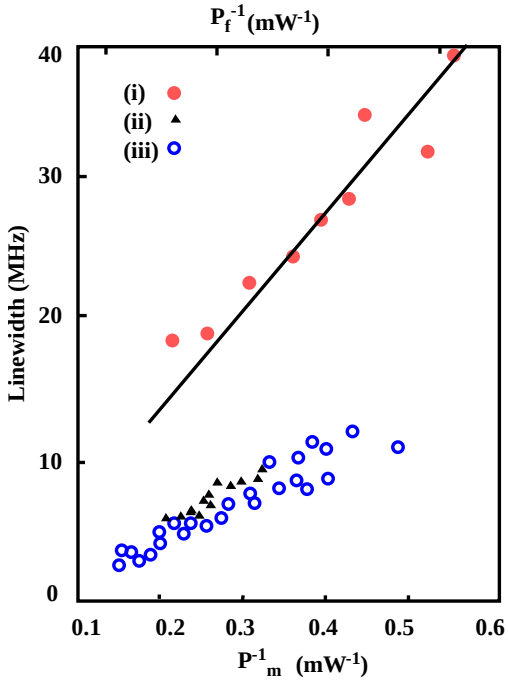

Figure 1.4: (i) Free-running follower linewidth against its reciprocal output power P_f^{-1} (ii) Master linewidth against its reciprocal output power P_m^{-1} (iii) Injection-locked follower linewidth against reciprocal output power P_m^{-1} [10].

The major theoretical works in the optical injection-locking domain were published in the 1980's as the above mentioned applications were developed. In 1982, Lang published his landmark paper that detailed the locking properties of semiconductor lasers [14]. Lang was the first to notice that the follower laser refractive index was subject to variations due to injection of external optical power.

The techniques to calculate the locking range for microwave oscillators were already published by several scientists, such as Kurokawa [15] 1973, but Lang was the first one to demonstrate the inherent asymmetry in the locking range of a semiconductor laser based optical injection-locking system. He argued that since the follower laser refractive index undergoes a non-negligible change following the optical power injection from the master laser, the locking range must depend upon the refractive index variation and the subsequent phase-amplitude coupling.

In 1985, Henry neatly formulated Lang's theory in his now famous paper by introducing the linewidth enhancement factor, currently known as Henry's factor, in the locking range calculations[16]. He also extended the conventional two-equation model used to simulate semiconductor laser small signal behavior to a three-equation model. The third equation taking into account the phase perturbations due to the injection of external optical power.

Henry determined the mathematical relationship explaining the increase in resonance frequency of an injection-locked laser but he concentrated more on the physical factors governing the determination of locking range and the stability of an injection-locked system than further exploring the bandwidth enhancement related to optical injection-locking. Mogensen et al. [17] published several works in the same period presenting the injection-locked system rate equations with Langevin noise sources. They also calculated the maximum phase tuning limits of a master-follower system.

After a burst in research efforts on optical injection-locking in the 80's, a rather slow period was encountered in the early and mid 90's. The reason for this can be explained with the advent of erbium-doped fiber amplifiers (EDFAs). Most of the injection-locking applications until then were focused on developing better ways to detect a modulated signal coherently. The EDFA made the possibility of in-fiber optical amplification a reality and brought the direct detection schemes to the foreground. Consequently optical injection-locking found itself a minor player in the booming telecoms revolution which was led principally by external light modulators, high-speed photodiodes and optical fiber amplifiers.

This situation started changing in mid to late 90's when first Simpson [18] and then Meng et al. [19] demonstrated the increase in modulation bandwidths and resonance frequencies of optically injection-locked semiconductor lasers. It was believed that injection-locking along with the bandwidth enhancement, chirp reduction and linewidth improvement could act as a major driving factor in the development of directly modulated long-haul high bit rate telecommunication systems: But this was not to be. In fact the utilization of EDFAs and external modulators had brought into market extremely reliable long-haul telecommunication systems functioning at high bit rates. The deployment of external modulators (e.g. of the Mach-Zhender type) not only avoided the chirp and linewidth related problems but also helped to achieve very high modulation rates by gaining independence from the intrinsic laser cavity parameters. The emergence of such an apparatus that achieved all the benefits proposed by the injection-locking techniques without actually using two lasers and the relevant circuitry made the optical injection-locking redundant. It is for this reason that since late 90's almost no further interest has been shown in the optical injection-locking of lasers for long-haul telecommunication systems.

With the advances in long-haul telecommunication due to the emergence of optical fibers, semiconductor lasers, photodiodes and fiber amplifiers, a vast optical fiber based infrastructure was laid out and developed through out the world especially in the Western European countries, in the United States and Canada and in the Asian economic powerhouses such as Japan, South Korea, Hong Kong and Singapore. A powerful optical fiber backbone system replaced the intercontinental submarine cables so much so that radio and satellite communications were effectively evicted from the consumer telecommunication domain and started serving either as a backup or in proprietary applications.

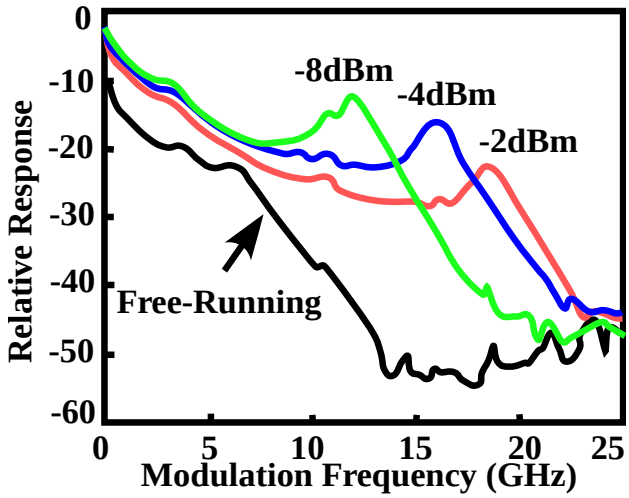

Figure 1.5: Demonstration of frequency response improvement of an injection-locked laser with increasing injected optical power by Meng et. al [19].

It might sound a bit strange but the optical fiber led high bit rate telecommunication revolution came to an abrupt end and by the first few years of the 21^{st} century the optical fiber based communications market was saturated. The reason was that once the optical fiber based backbone networks were laid out, the telecommunication companies realized that an optical fiber link to the subscriber would be utterly unfeasible economically due to very high costs of the electro-optic equipment such as lasers, photodiodes and related circuitry required for every subscriber. Optical fiber based telecommunication had economic utility only over very large distances and very high bit rates such as Wide Area Networks (WANs), Metropolitans Area Network (MANs) or inter continental links.

The economic bottleneck that halted the growth of optical fiber based communications posed a very challenging (and somewhat embarrassing) problem to researchers and developers. The absence of Fiber To The Subscriber (FTTX) networks decreed that the consumer remain on a copper-based or wireless systems (in fact POTS: Plain Old Telephone System). Despite the giant leaps in optical fiber communications the Metropolitan Area Networks (MANs) and the Local Area Networks (LANs) continued to operate using electrical-electrical infrastructures and interfaces. This meant that despite the ability of optical fiber based telecommunication networks to allow very high bit rates, the end-user continued to suffer the meager bandwidths offered by the copper based systems. Attempts were made to conceive high speed LANs using optical fibers but the cost of coherent light sources always remained an insurmountable factor. The high cost of coherent light sources for short-haul communications always translated into economic unfeasibility and underutilization of the telecommunication system. Light Emitting Diodes (LEDs) were used in some such optical fiber based LANs albeit more for want of anything suitable than as a conscious

choice.

It is clear that the FTTX project needed a cheap, low-power, coherent light source, compatible with the existing optical fiber infrastructure. The absence of such a source translated into the continued utilization of older, low bit rate communication schemes and infrastructures by the end-user.

1.2 Emergence of Vertical-Cavity Lasers

1.2.1 Historical Background and Motivation

It must be noted that the Vertical-Cavity Surface-Emitting Lasers (VCSELs) or simply SELs (Surface-Emitting Lasers, as they were referred to as at that time) were not proposed to overcome the bottlenecks that had hindered the progress of FTTX systems. The lasers usually used for long-haul telecommunications have cleaved structures with edge emission. Consequently they are referred to as Edge Emitting Lasers (EELs). This structure does pose some problems, e.g. the initial probe testing of these devices is impossible before there separation into individual chips. Their monolithic integration is also limited due to finite cavity length. The cavity length implies generation of undesirable longitudinal modes and the non-monolithic fabrication process implies the impossibility of fabricating laser arrays and matrices. It was specifically in order to overcome these problems that , K. Iga, a professor at that time at Tokyo University, proposed a vertical-cavity laser in 1977.

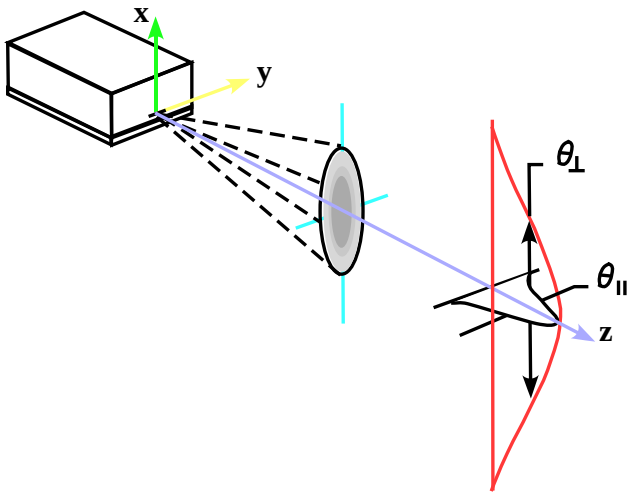

Figure 1.6: Schematic representation of far-field emission of a stripe-geometry Double Heterostructure (DH) laser. The full angles at half power, perpendicular to and along the junction plane, are indicated [20].

These surface-emitting lasers provided following advantages

- Probe-testing during the manufacturing process.

- Fabrication of a large number of devices by fully monolithic processes yielding a very low-cost chip-production.
- Very small cavity length guaranteeing longitudinal single mode operation.
- Possibility of production as arrays and matrices.
- Very low threshold currents due to ultra small cavity volume.
- Monolithic integration compatibility with other devices.
- Circular far-field pattern as compared to elliptical pattern for EELs.

A pulsed operation at 77K with a threshold current of 900mA was demonstrated in 1979 with a $GaInAsP$-InP vertical-cavity laser emitting at 1.3μm [21]. However, more pressing issues regarding the delivery of higher bit rates using the conventional EELs meant that the research into vertical-cavity lasers progressed very slowly. Consequently VCSEL research and development stagnated through out the decade that followed its first demonstration.

Continuous Wave (CW) operation of a VCSEL was presented in 1989, by Jewell et. al, for a device emitting at 850nm [22]. This VCSEL presented two unique features as compared to the previous generation of components. It had a QW-based active region and the semiconductor DBR mirrors were grown by means of Molecular Beam Epitaxy (MBE) which replaced the dielectric mirrors previously being used. The VCSEL technology then progressed steadily over the next ten years. A 2mA threshold quantum-well device was presented in 1989 [23]. In 1993 CW operation for a VCSEL emitting at 1.3μm was demonstrated [24]. A high power VCSEL emitting at 960nm and with an output of 20mW CW output was reported in 1996 [25].

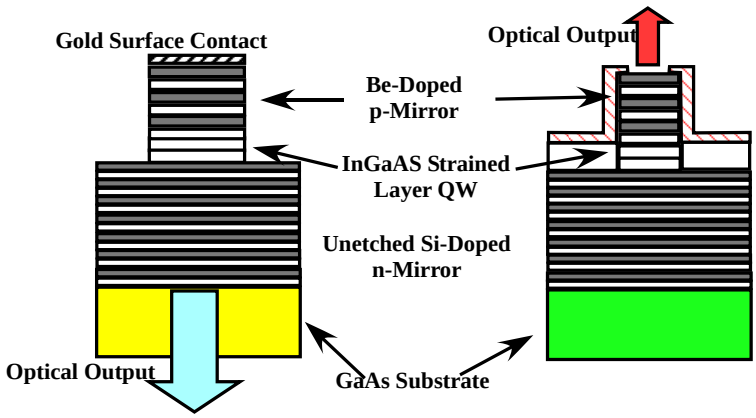

Figure 1.7: An early design schematic for top-emitting and botton-emitting VCSELs presented by Jewell et. al. in 1989.

The polarisation properties of VCSELs emitting in the near infra-red ranges were investigated, for the first time, by Besnard et. al in 1996 [26], [27]. It wasšshown that commercial VCSELs' emission switches between two eigenstates with the injection of polarized light inside the VCSEL optical cavity. This technique could then be utilised for switching applications in telecommunication networks. Bondiou et. al demonstrated the push-pull effects, hysteresis phenomena, chaos and phase and frequenct-locking using injection-locking in long wavelength single-mode VCSELs [28].

Despite these advances and maturity in fabrication technology, the VCSELs could not replace the EELs as optical sources for long-haul telecommunications and were hence confined to other applications such as optical computing, sensors, barcode scanners and data storage etc.

The reason for this shortcoming lies in the VCSEL physical structure that gives priority to

- Monolithic integration favoring vertical emission
- Low threshold current
- On chip testing

These priorities impose a set of design guidelines for VCSEL fabrication which, when implemented, induce certain unwanted and unforeseen traits in the device behavior. These undesirable characteristics rendered the VCSEL unsuitable for utilization in prevalent telecommunication systems.

Following is a concise analysis of these shortcomings. We would present the basic VCSEL structure that would try to achieve the above given objectives. Following this discussion we would present the drawbacks in the device performance related to the realization of design objectives. Certain remedies and improvements would then be presented in order to render the device more performing and efficient.

1.2.2 VCSEL Structure

A VCSEL is essentially a gain medium based active region vertically stacked between two Distributed Bragg Reflectors (DBRs). In order to achieve a single mode operation it is proposed that the length of the active region be very small: Effectively of the order of the desired lasing wavelength. A short cavity eliminates the generation of longitudinal modes associated to Fabry-Perot cavities. This however imposes a severe restriction on VCSEL DBR design. The threshold gains for the surface-emitting and edge-emitting devices must be comparable regardless of the cavity length. The threshold gain of an EEL is approximately $100cm^{-1}$.

For a VCSEL of active layer thickness of 0.1 μm, this value corresponds to a single-pass gain of about 1%. Thus for a VCSEL to lase with a threshold current density comparable to that of an EEL, the mirror reflectivities must be greater than 99% in order to ensure that the available gain exceeds the cavity losses during a single-pass.

Achieving a reflectivity of 99% with DBRs is a formidable task and thus central to the conception of low threshold VCSELs is the capacity to fabricate high reflectivity mirrors. Let's consider the example of a VCSEL operating at 850nm. The active region would consist of several ultra thin layers composed alternately of GaAs and AlGaAs materials. The difference between the refractive index of layers of a pair determines the number of pairs required to achieve a reflectivity of 99% or more. In the case of $AlAs$-$Al_{0.1}Ga_{0.9}As$ the refractive index difference between two alternate layers is 0.6 (cf. Fig.1.8) [29]. Consequently, as shown in fig. 1.9, only 12 pairs are needed to achieve a reflectivity of 99% or more [30].

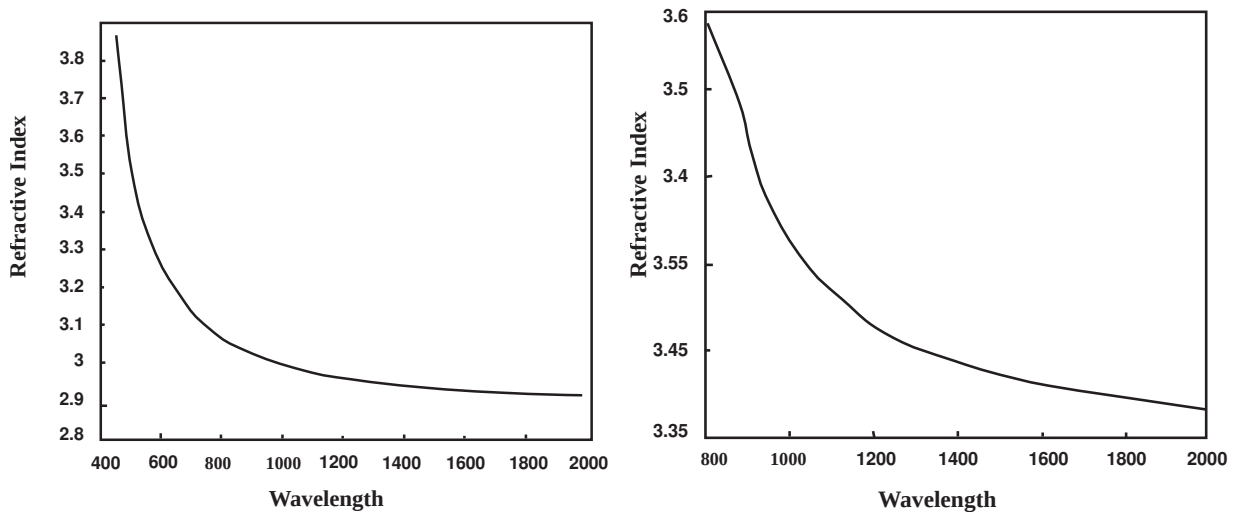

(a) Refractive Index of AlAs

(b) Refractive Index of $Al_{0.1}Ga_{0.9}As$

Figure 1.8: Refractive indices of AlAs and $Al_{0.1}Ga_{0.9}As$ as a function operating wavelengths.

As far as AlAs and $Al_xGa_{1-x}As$ alloys go, the situation is conducive, even desirable, for the fabrication of VCSELs using these materials. The band gap energy of $AlAs-Al_xGa_{1-x}As$ alloys is about $1.5eV$ which eventually corresponds to a wavelength in the 800-900nm region. Fabrication technology for VCSELs emitting in this wavelength band therefore has perfectly been mastered since monolithic growth of 12-15 DBR pairs does not pose serious fabrication challenges. Furthermore $AlAs$-$GaAs$ alloy DBRs have an excellent thermal conductivity which allows the dissipation of heat fairly rapidly and avoids device heating which eventually could have been responsible for VCSEL underperformance.

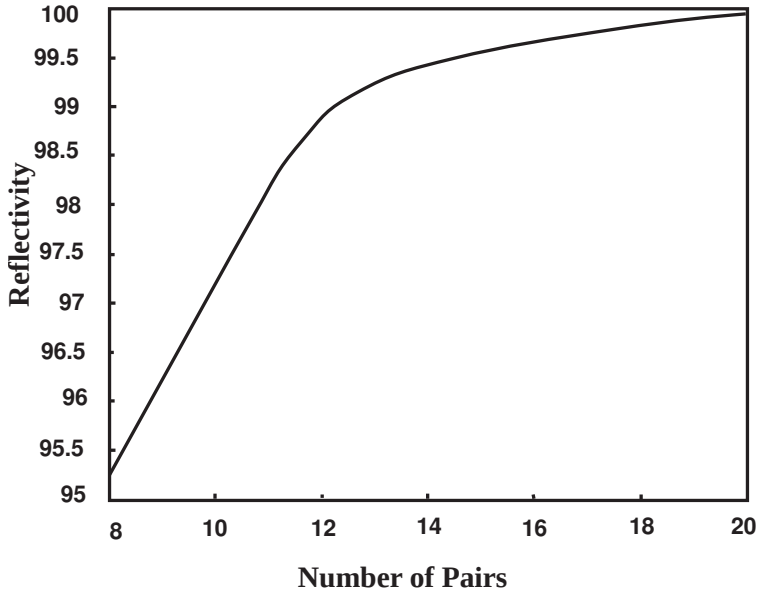

Figure 1.9: Calculated reflectivity of an $AlAs$-$Al_{0.1}Ga_{0.9}As$ multilayer semiconductor Bragg reflector as a function of the number of pairs [30].

1.2.3 Performance Drawbacks

As far as the fabrication of near infrared VCSELs was concerned, the existing technologies and fabrication processes proved to be quite adequate. However, applying a similar methodology to telecommunication wavelength VCSELs proved to be much more challenging. Long wavelength VCSELs operating in the 1.1μm-1.6μm range are of considerable interest for optical fiber telecommunications since the hydroxyl absorption and pulse dispersion nulls for silicon optical fibers are found at 1.5μm and 1.3μm respectively. Although several material systems were considered, the combination $InGaAsP$-InP turned out to be the most suitable in view of the near perfect lattice match. The active layer is composed of the $In_{1-x}Ga_xAs_yP_{1-y}$ quaternary alloy. By varying mole fractions x and y, almost any wavelength within the $1.1-1.6\mu$m can be selected.

1.2.3.1 DBR Growth

Only $12-15$ $AlAs-Al_xGa_{1-x}As$ pairs are needed to fabricate a DBR with a 99% reflectivity (cf. Figures.1.8 and 1.9). By contrast, the refractive index difference between an InP-$InGaAsP$ pair is only 0.3 and hence more than 40 pairs would be needed to achieve a reflectivity of 99%. The problem consequently encountered concerns thermal properties of InP−based materials that intervene to affect the process in following ways [31], [32]:

- For the fabrication of long wavelength VCSELs, there are mainly $In_{1-x}Ga_xAs_yP_{1-y}$ alloys available which have to be grown on InP substrates. Due to the effects of

non negligible Auger's recombination effects and intravalence band absorption, these materials suffer from temperature-dependent losses.

- The thermal conductivity is greatly reduced due to alloy disorders which causes phonon scattering. This reduction in thermal conductivity is particularly adverse for effective heat sinking through the VCSELs' DBRs usually having a thickness of several μms.
- $AlAs$-$Al_xGa_{1-x}As$ DBRs have a good thermal conductivity and could be thinner but due to lattice mismatch could not be grown on the InP substrate.

DBR growth has been one of the fundamental problems regarding the fabrication of long wavelength VCSELs that has hampered the entry of VCSELs in high-speed data, command and telecommunications domain.

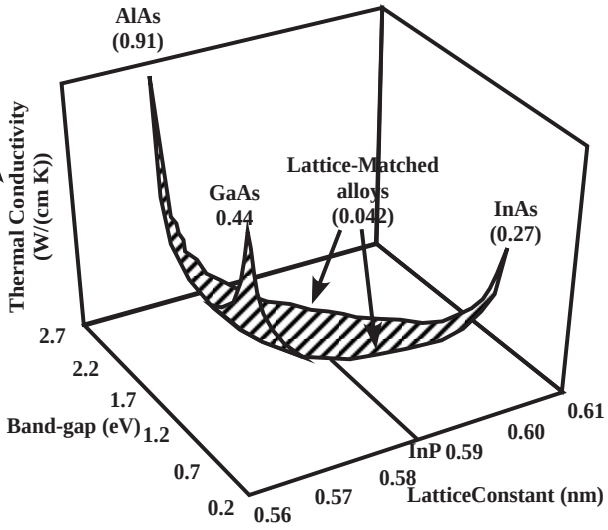

Figure 1.10: Thermal conductivity of the various alloy compositions of the $InGaAlAs$ Material System plotted versus free lattice constant and band gap energy. The line indicates the quaternary compositions that can be used for DBRs on InP. [32]

It can be seen in the Fig.1.10 that the values of thermal conductivity for InP−based materials lattice matched alloys are very feeble as compared to those of $GaAs$, $AlAs$ or $InAs$ alloys.

1.2.3.2 Optical and Electrical Confinement

Growing stacks of DBRs was not the only problem encountered by VCSEL manufacturers. One of the primary objectives of VCSEL design was to fabricate short cavity single mode devices. The short cavity did eliminate the undesirable longitudinal modes but it gave birth to another unforeseen problem. Initial VCSEL designs suggested that the carriers and the photons share a common path traversing the DBRs. This led to the heating of certain zones

of the DBRs due to carrier flow and resulted in a variable refractive index distribution inside the VCSEL optical cavity. This phenomenon is known as "Thermal Lensing". Instead of being concentrated in the center in the form of a single transverse mode, the optical energy is repartitioned azimuthally inside the optical cavity. This particular optical energy distribution is observed in the form of transverse modes. Higher bias currents therefore imply high optical power and in consequence a higher number of transverse modes.

An oxide-aperture is employed, principally in shorter wavelength emission VCSELs, in order to block the unwanted transverse modes. The oxide-aperture diameter then determines the multimode or single mode character of a VCSEL. VCSELs having oxide aperture diameters greater than 5μm exhibit multimode behavior. It can also be inferred from the above discussion that for the type of VCSELs employing the oxide-aperture technology for optical confinement, single mode VCSELs almost always have emission powers less than those of multimode VCSELs.

The problem of optical and electrical confinement are hence interrelated. It is evident that in order to attain single mode emission the thermal lens effect must be avoided. This can only be achieved by segregating the carrier and photon paths. Although challenging technically, it can be achieved using a tunnel junction. The concept and functioning of a tunnel junction is explained in the following sub-section.

1.2.4 The Tunnel Junction

The "Tunnel Junction" was discovered by L. Esaki in 1951 [33] and the tunnel junction diodes used to be labeled "Esaki Diodes" for quite some time after this discovery [34], [35], [36]. Esaki observed the tunnel junction functioning while working on Ge layers but soon after his discovery, tunnel junction diodes were presented by other researchers on other semiconductor materials such as $GaAs$ [37], $InSb$ [34], Si [35] and InP [36].

The tunnel junction is formed by joining two highly doped (degenerate) "p" and "n" layers. It has a particular current-voltage characteristic curve. A negative differential resistance region ($-\frac{dI}{dV}$) over part of the forward characteristics can be observed. Fig.1.11 presents the static current-voltage characteristics of a typical tunnel-junction diode.

In the case of a VCSEL the tunnel junction serves a "Hole Generator". Under the tunnel effect, the electrons move from valence band (doped p^{++}) to conduction band (doped n^{++}), leaving holes in their place. Fig.1.12 shows the schematic diagram of a tunnel diode in reverse bias conditions. The existence of a tunnel junction in a VCSEL presents following advantages:

- It reduces the intra valence band absorption due to P doping.
- It serves to reduce the threshold current, by improving the carrier mobility.

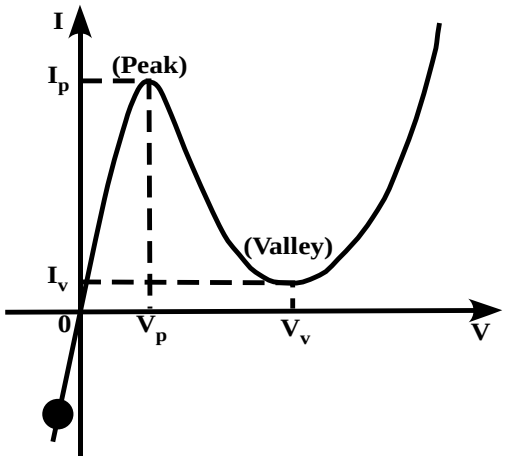

Figure 1.11: Static current-voltage characteristics of a typical tunnel diode. I_p and V_p are the peak current and peak voltage. I_v and V_v are the valley current and valley voltage. The balck circle signifies operation in reverse bias conditions.[20].

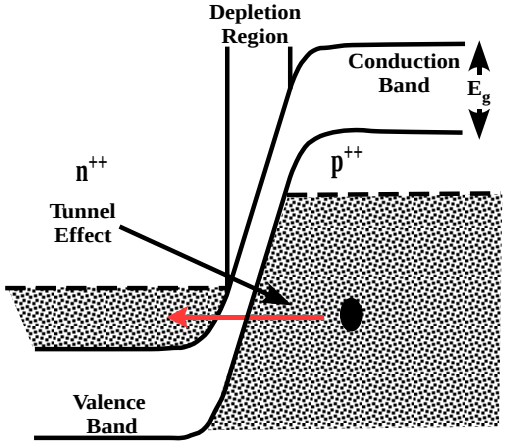

Figure 1.12: Energy-band diagram of tunnel diode in reverse bias state [20].

- It is used for electrical as well as optical confinement.

Due to these properties, the tunnel junction has become an integral part of long wavelength VCSELs.

1.2.5 Technological Breakthroughs and Advances in Long Wavelength VCSEL Fabrication

Although by the start of the 21^{st} century serial production and delivery of VCSELs was in full flow for diverse applications, they had failed to fulfill the two following essential criteria for utilization in optical networks.

- They did not emit in the 1.3μm and 1.5μm range: The so-called "Telecoms Wavelengths". This meant not only definition and standardization of new standards at 850nm wavelength but also the deployment and manufacturing of a host of optical components such as optical fibers, couplers, multiplexers and photodiodes compatible with the 850nm emission range.
- As has been explained above, transverse-mode operation starts to manifest itself from a few milliamperes above the threshold current rendering the VCSELs multimode in character. This multimodality is disconcerting in two ways:
  - It reduces the effective channel bandwidth hence reducing the maximum deliverable bit rate.
  - It requires the utilization of multimode optical fiber which although being less expensive than the single mode fiber, affects the VCSEL operation in another way. When high optical powers are injected in a multimode fiber, several undesired fiber modes are excited thus reducing the effective bandwidth.

It is clear from the above discussion that a suitable substitute for EELs, for applications in short to medium distance optical fiber networks, must possess the following properties

- It must emit at either 1.3μm or at 1.5μm wavelength so that the existing standards, infrastructure, optoelectronic components and devices could be utilized.
- It must have a single mode emission spectrum so as to profit from the high bandwidths offered by the employment of single mode optical fibers.

As late as 2000, there were no serial production and mass deployment of VCSELs that fulfilled these two essential criteria. As has been discussed above, this was due to the technical challenges posed by a combination of several different factors which rendered the fabrication of long wavelength VCSEL devices very difficult.

1.3 Emergence of Long Wavelength VCSELs

Regarding the manufacturing of long wavelength VCSELs, several different research groups kept trying to realize long wavelength emission devices. In 1993, Iga et al. demonstrated the CW operation of a 1.3μm $InGaAs$-InP based VCSEL at 77K [21]. The upper DBR consisted of 8.5 pairs of p-doped MgO-Si material with Au-Ni-Au layers at the top while the bottom DBR consisted of 6 pairs of n-doped SiO-Si material (Dielectric Mirror).

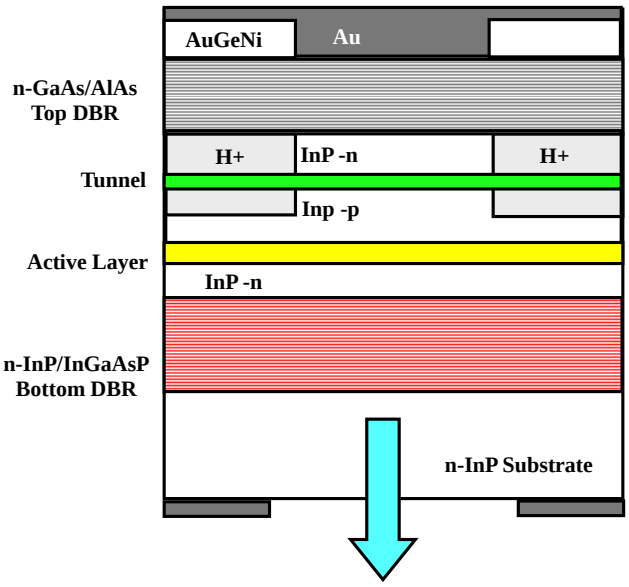

Figure 1.13: A long wavelength VCSEL with a tunnel junction emitting at 1.55μm presented by Boucart et. al in 1999.

In 1997, Salet et.al demonstrated the pulsed room-temperature operation of a single mode $InGaAs$-InP VCSEL emitting at 1277nm. The bottom mirror consisted of n-doped $InGaAsP$-InP material grown epitaxially to form a 50 pair DBR mirror with a 99.5% reflectivity. The device threshold current at 300K was 500mA [38]. The top mirror was realized using p-doped SiO_2-Si reflectors. A year later, in 1998, Dias et al. reported the growth of $InGaAsP$-InP, $AlGaInAs$-$AlInAs$ and $AlGaAsSb$-$AlAsSb$ based DBRs on InP substrates to achieve reflectivities up to 99.5% [39].

Soon afterward, in 1999, Boucart et. al extended their previous work to demonstrate the room temperature CW operation of a 1.55μm VCSEL [40]. In this case the top DBRs consist of 26.5 n-doped $GaAs$-$AlAs$ pairs which were grown directly on an n-InP substrate (Metamorphic mirrors). A tunnel junction was fabricated to localize the current injection. The bottom mirror consisted of 50 pairs of n-doped $InGaAsP$-InP layers having a reflectivity of 99.7%. The device had a threshold current of only 11mA and had been fabricated using gas-based Molecular Beam Epitaxy (MBE). The tunnel junction proved benificial in two ways:

- It enabled the utilization of two n-doped DBRs;

- Once the conductive properties of the tunnel junction were neutralized using H^+ ion implantation, it served to localize the current injection without having to etch a mesa. The resulting device was therefore coplanar in structure

It can be ascertained from Table.1.1 that several different materials such as $InGaAsP$, $InGaAsAl$, $InGaAsSb$ and $InGaAsN$ were chosen to fabricate the active layer. The material choice for DBRs and the fabrication processes were equally diverse. Although most of the research groups chose "Monolithic Integration Techniques" for the fabrication of VCSELs, "Wafer Fusion" , and "Fusion Bonding" were also applied.

Meanwhile, in 1998, the Institute of Electrical and Electronics Engineers (IEEE) defined the "1000BASEX-Gbps Ethernet over Fiber-Optic at 1Gbit/s" standard. This standard for the transmission of "Ethernet Frames" at a rate of at least one Gbps was defined using light sources emitting at 850nm. The definition of Gigabit Ethernet standards using 850nm optical sources boosted the research and development of near infrared emission VCSELs. By the year 2000, 850nm VCSELs had firmly established themselves as standard optical sources for short-haul communication applications. This development was a setback for ongoing research in long wavelength VCSELs and as a result many research groups shifted their focus from long wavelength VCSEL development to other emerging fields. Furthermore, the research focus, even in the long wavelength VCSEL development field, shifted toward a new dimension. Long wavelength VCSELs were no longer being developed solely as telecommunication sources, an emerging field of spectroscopy was beginning to play an increasingly important part in eventual long wavelength VCSEL applications.

1.3.1 Vertilas VCSELs

Although long wavelength VCSEL operation using a tunnel junction device was already demonstrated by Boucart et al. [40] in 1999, Ortsiefer et al. [51] presented a variation to this concept. Soon the single mode room temperature operation of an InP-based VCSEL

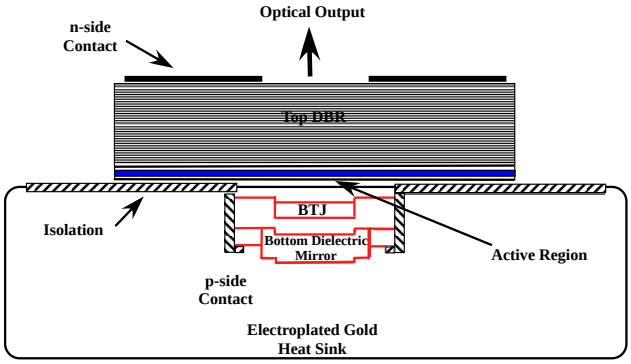

Figure 1.14: A Vertilas BTJ structure with an emission wavelength of 1.55μm [31].

operating at 1.5μm was demonstrated by the same research group [52]. The top DBR is

Active Region	**DBRs**	**Fabrictaion Process**	**Research Group**
$InGaAsP$-InP 1.3μm	8.5 pairs of p-doped MgO-Si with $Au/Ni/Au$ metal at the top and 6 pairs of n-doped SiO/Si at the bottom	Monolithic	Baba et al. 1993 [24]
$InGaAsP$-InP 1.3μm	p doped SiO_2-Si at the top and 50 pairs of n-doped $InGaAsP$-InP at the bottom	Monolithic	Salet et. al 1997 [38]
$AlGaInAs$-InP 1.3μm	27 pairs of p and n-doped $GaAs$-$AlAs$ layers at the top and at the bottom respectively	Double Fusion Bonding	Qian et al. 1997 [41]
$GaInAsN$-$GaAs$ 1.8μm	21 and 25.5 pairs of p and n-doped $GaAs$-$AlAs$ layers at the top and at the bottom respectively	Monolithic	Larson et. al 1998 [42]
$InGaAsP$-InP 1.5μm	30 pairs of p-doped $GaAs$-$Al_{0.67}Ga_{0.33}As$ at the top and undoped $GaAS$-$AlAs$ at the bottom	Wafer Fusion	Margalit et. al 1998 [43]
$InGaAsP$-InP 1.55μm	26.5 pairs of n-doped $GaAs$-$AlAs$ at the top and 50 pairs of n-doped $InGaAsP$-InP at the bottom	Monolithic	Boucart et al. 1999 [40]
$InGaAsP$-InP 1.55μm	30 pairs of p doped $GaAs$-$Al_{0.85}As_{0.15}Ga$ at the top and 50 pairs of n-doped $InGaAsP$-InP at the bottom	Wafer Fusion and Epitaxy	Rapp et. al 1999 [44]
$InGaAlAs$ 1.56μm	35 pairs of p-doped $InGaAlAs$-$InAlAs$ at the top and 43.5 pairs of n-doped $InGaAlAs$-$InAlAs$ at the bottom	Monolithic	Kazmierski et. al 1999 [45]
$AlInGaAs$ 1.55μm	45 and 35 pairs of n-doped $Al_{0.09}Ga_{0.38}In_{0.53}As$-$Al_{0.48}In_{0.52}As$ at the top and at the bottom respectively	Monolithic	Hall et. al 1999 [46]
$AlInGaAs$ 1.55μm	30 and 23 pairs of n-doped $AlAs_{0.56}Sb_{0.44}$-$Al_{0.2}Ga_{0.8}As_{0.58}Sb_{0.42}$ at the top and at the bottom respectively	Monolithic	Hall et. al 1999 [47]
$GaAsSb$ 1.23μm	19 and 30.5 pairs of p and n-doped $GaAs$-$AlAs$ at the top and at the bottom respectively	Monolithic	Yamada et. al 2000 [48]
$GaInNAs$-$GaAs$ 1.18μm	24 and 35 pairs of p-doped and n-doped $Al_{0.7}Ga_{0.3}As$-$GaAs$ at the top and at the bottom respectively	Monolithic	Kageyama et. al 2001 [49]
$AlInGaAs$ 1.55μm	32 and 23 pairs of n-doped $AlAs_{0.56}Sb_{0.44}$-$Al_{0.2}Ga_{0.8}As_{0.52}Sb_{0.48}$	Monolithic	Hall et al. 2001 [50]

Table 1.1: Long Wavelength VCSEL Fabrication Development Chronology

composed of 34.5 $InGaAlAs$-$InAlAs$ pairs. The bottom mirror is comprised of 2.5 pairs of CaF_2-Si with Au-coating. The gold coating, apart from serving as a high reflectivity mirror (99.75%), serves as an integrated heat sink [31]. The successful incorporation of tunnel junction in the long wavelength VCSEL design proved to be the technical breakthrough that would present VCSELs as standard devices for short to medium distance optical fiber communications. By 2002 Vertilas was delivering 1.55μm single mode VCSELs for 10Gbps operation.

1.3.2 BeamExpress VCSELs

1.3.2.1 Wafer Fusion

The manufacturing of a long wavelength VCSEL requires the growth of an InP-$InGaAsP$ alloy active region on an InP substrate. These alloys however are difficult to grow as DBR stacks above and below the active region since the restrictions imposed by the material thermal conductivity render proper device functioning impossible. On the other hand, $AlAs$-$Al_xGa_{1-x}As$ DBRs have a good thermal conductivity but they can not be monolithically grown on InP-based substrates due to lattice mismatch. The solution to the matching of disparate materials to optimize VCSEL performance was developed at the University of California Santa Barbara (UCSB) in 1996 by Margalit et. al [53].

The technique utilized is known as "Wafer Fusion" or "Wafer Bonding" and consists of establishing chemical bonds directly between two materials at their hetero-interface in the absence of an intermediate layer [54]. The first demonstration constituted of fabrication of a 1.55μm VCSEL. The device was fabricated by wafer fusion of MOVPE-grown $InGaAsP$ quantum well active region to two MBE-grown $AlGaAs$-$GaAs$ DBR reflectors [53].

1.3.2.2 Localized Wafer Fusion

By applying a variant of the "Wafer Fusion" technique in 2004, Kapon et. al demonstrated that it was possible to grow separate components of a VCSEL cavity on separate host substrates [55], [56]. These separate components were then bonded (fused) together to construct the complete VCSEL optical cavity. This process was developed at the Ecole Polytechnique Fédérale de Lausanne (EPFL) and patented as "Localized Wafer Fusion".

A majority of VCSELs used in this work are BeamExpress VCSELs. Fig.1.15 presents the structure of a BeamExpress VCSEL with an emission wavelength of 1.55μm. This is a double intracavity contact single-mode VCSEL with coplanar access. The InP-based optical cavity consists of five $InAlGaAs$ quantum wells. The top and bottom DBRs comprise of 21 and 35 pairs respectively and are grown by Metal-Organic Chemical Vapor Deposition (MOCVD) epitaxy method. Using the technique of localized wafer fusion, the top and the

bottom *AlGaAs-GaAs* DBRs are then bonded to the active cavity wafer and the tunnel junction mesa structures.

Using VCSELs with double intracavity contacts has its own advantages. These contacts are much nearer to the active region than the classical contacts. Their utilization combined with the presence of tunnel junction allows to have lower series resistance as compared to oxidized-aperture VCSELs. Due to this proximity of the contacts to the active region these VCSELs tend to have a high quantum efficiency. Their location near the active region results in no current passage through DBRs.

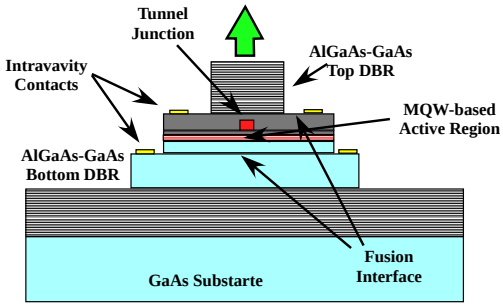

Figure 1.15: Schematic diagram of a wafer-fused Beam-Express VCSEL with an emission wavelength of 1.5μm.

The process used for the fabrication of Beam Express VCSELs is not monolithic. The bottom *AlGaAs-GaAS* DBR is grown on the *GaAs* substrate. The *InP*-based cavity is then bonded to this DBR. After the growth of an isolation layer on the active region, the epitaxially grown *AlGaAs-GaAs* top DBR is fused to complete the optical cavity. This double fusion increases the complexity of the fabrication process but it presents certain advantages. Wafer-fusion allows to replace the *InAlGaAs* DBRs by GaAs DBRs. Not only the *GaAs* DBRs have a better thermal conductivity, they are much cheaper than *InAlGaAs* DBRs which allows to increase the performance and decrease the cost of the component at the same time. The biggest advantage of "Wafer Fusion" is the possibility of serial production of VCSELs which further serves to reduce the component cost.

1.3.3 RayCan VCSELs

Starting as a spin-off company from the Korean government funded Electronics and Telecommunications Research Institute (ETRI) in 2002, RayCan launched an ambitious project for manufacturing of long wavelength VCSELs. Instead of using the above described specialized technologies for long wavelength VCSEL manufacturing, RayCan decided to embark upon a different course. They decided to monolithically grow InAlGaAs DBRs and an InGaAs-based quantum well active region on an InP substrate. As has been discussed above, this technique was previously not considered because in order to achieve 99% reflectivity using InAlGaAs-based DBRs, a growth of more than 40 pairs is needed. Fig. 1.16 presents a

comparison of the number of DBRs needed to achieve a near unity reflectivity using different materials.

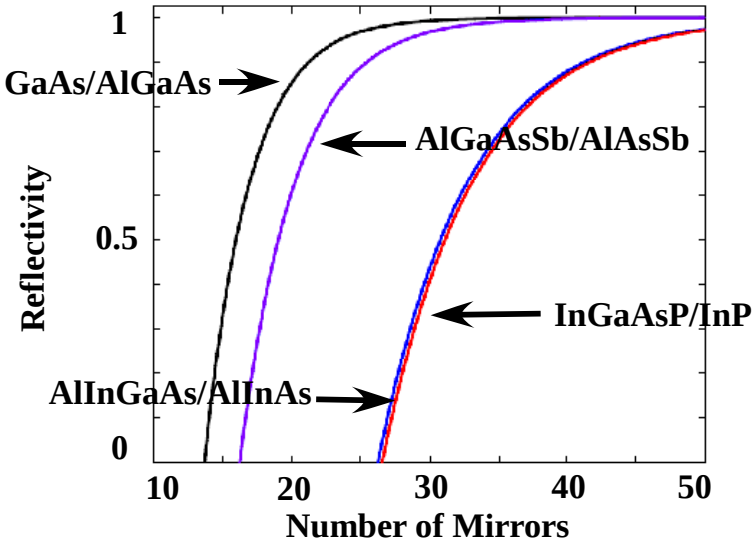

Figure 1.16: Calculated reflectivity of different materials used as semiconductor Bragg reflectors as a function of the number of pairs [57].

RayCan employed Metal-Organic Chemical Vapor Deposition (MOCVD) technique to fabricate a long wavelength VCSEL. For 1.55μm VCSELs, the top and bottom DBRs were grown as 28 and 38 pairs of undoped $InAlGaAs$-$InAlAs$ schemes. The top and bottom DBRs consisted of 33 and 50 layers respectively for 1.3μm emission VCSELs. The 0.5λ thick active region consists of seven pairs of strain-compensated (SC) InAlGaAs quantum wells [58]. The lower number of top DBRs in both the VCSELs was compensated by using an $InAlGaAs$ phase-matching layer and Au metal layer. Figure. 3.20 presents the structure of a RayCan VCSEL emitting at 1.5μm. RayCan has been shipping 1.3μm and 1.5μm VCSELs since 2004. In November 2005 RayCan shipped its first 10GBit/s long wavelength CWDM VCSEL module.

1.4 Long Wavelength VCSEL Direct Modulation

1.4.1 Need for VCSEL Optical Injection-Locking

Up to this point we have discussed the prospects of long wavelength VCSELs in the context of high bit rate data delivery over medium and short distance links. It would not be an exaggeration to state that consumer demand for multimedia and interactive applications and therefore bandwidth has increased to an unprecedented level. Current electrical-electrical infrastructures can not support this demand. The major obstacle in switching from electrical/hertzian systems to optical/fibered systems is the cost of the coherent optical source compatible with existing infrastructure. Recent advances in the fabrication, development

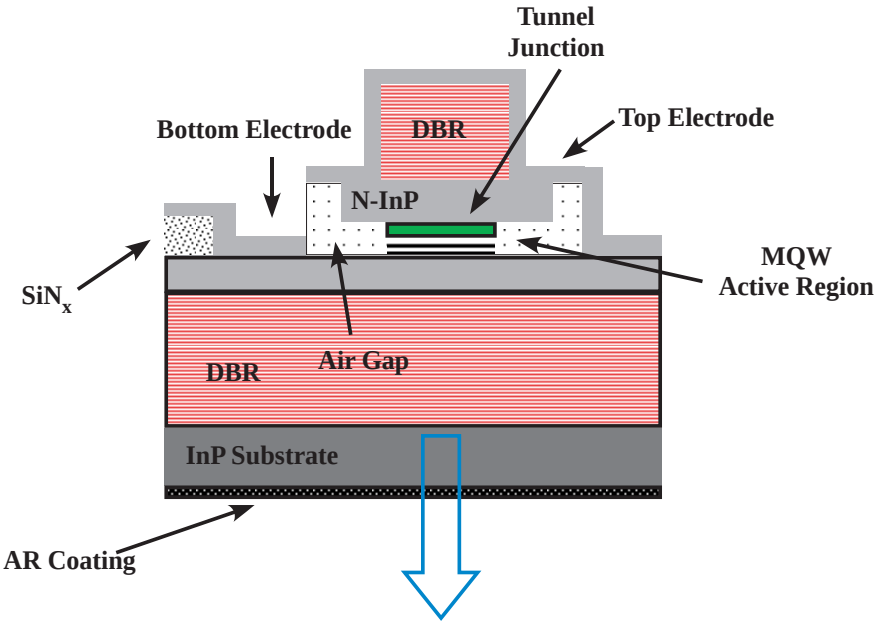

Figure 1.17: MOVCD Grown monolithic structure of a 1.5μm RayCan VCSEL.

and serial production of VCSELs emitting at 1.3μm and 1.5μm have paved the way for future FTTX systems [59].

Having been able to solve the problem at component level, by developing reliable long wavelength VCSELs, the next logical approach is the development of new systems incorporating these components. Conventionally the EELs used in the long-haul fiber links are externally modulated i.e. the photon generation process inside the cavity is independent of the modulation mechanism. While being extremely effective, this method necessitates the utilization of an external modulator which increases the system cost. Such a scheme is inherently unfeasible for FTTX systems due to the cost of the external modulators.

The elimination of external modulators as a component of choice for FTTX systems decrees the employment of direct modulation techniques. In this technique the laser diode bias current is varied to achieve the optical output intensity variation. Apparently the scheme is simple and easy to implement, but when put into practice, it presents two major problems which are detailed in the following two sub-sections.

1.4.1.1 Phase-Amplitude Coupling

Semiconductor lasers, whether EELs or VCSELs, are different from other lasers in one respect. The refractive index of a semiconductor laser depends on the carrier concentration inside the cavity. The carrier concentration variation affects the refractive index of the cavity which eventually changes the emission wavelength of the component. The consequences of

this uniqueness manifest themselves during the process of direct modulation. A variation in bias currents varies the optical output power as well as the optical frequency of the cavity. These variations are proportional to the variation in carrier concentration and therefore the bias current. The device is modulated in amplitude and frequency at the same time. This phenomenon of "Phase-Amplitude Coupling" or the dynamic shift of the lasing frequency during modulation is known as "Frequency Chirping" or simply "Chirping".

Chirping broadens the linewidth of a laser. The extent to which a pulse broadens depends upon the amplitude of the modulating signal. Larger modulation amplitudes result in linewidths of the order of GHz [1]. This spectral broadening at the time of modulation becomes more pronounced during the passage of the modulated pulse through an optical channel and the effective channel bandwidth is reduced. Direct modulation while being cost-effective proves to be **inefficient**, in terms of deliverable bit rates, when compared to external modulation.

1.4.1.2 Intrinsic Modulation Limits

A semiconductor optical cavity, in essence, is a resonator. Like every resonator, or electrical circuit for that matter, its frequency response depends on its intrinsic parameters. In case of semiconductor lasers these parameters might be cavity volume, photon and electron populations, group velocity, gain compression factor etc. When directly modulated, a laser can not better the modulation frequency response already defined by these intrinsic parameters. On the other hand, the utilization of an external modulator provides a means to bypass the laser intrinsic parameters. The modulation response (or the deliverable bit rate) of the system is then defined by the external modulator and not the laser.

1.5 Long Wavelength VCSEL Optical Injection-Locking

It is clear from the description of the two above given problems that a viable optical system must minimize the effects of "Amplitude-Phase Coupling" and "Intrinsic Modulation Limits" in order to be efficient and acceptable. Once injection-locked, the master laser holds the frequency of the follower laser and makes it immune to carrier variations. This isolation from carrier variations appears as the reduction of chirp during direct modulation. In 1984, Lin et al. [11] demonstrated the reduction of frequency chirping in a directly modulated semiconductor laser by the application of injection-locking technique.

Henry presented an approximate formula for the calculation of resonance frequency of optically injection-locked semiconductor lasers [16] but its significance was not appreciated at that time until Simpson [61] and Meng [62] demonstrated bandwidth and resonance frequency enhancements in late 90's. In 2002, a research group in University of California

[1] Typical VCSEL linewidth is of the order of tens of MHz [60].

Berkley (UCB), led by Connie J. Chang-Hasnain reported the first optical injection-locking of a long wavelength VCSEL for 2.5Gb/s transmission [63].

In 2003 long wavelength VCSEL chirp reduction and bandwidth enhancement were presented by the same research group [64] but there was a marked technical difference from their first publication. Whereas the first time optical injection-locking of a long wavelength VCSEL was carried-out using an identical VCSEL, the second demonstration used a Distributed FeedBack (DFB) laser to injection-lock a long wavelength VCSEL. The group has extensively published on the subject of the optical injection-locking of long wavelength VCSELs [65], [66], [67], but this pattern of locking a VCSEL with a DFB has remained unchanged since.

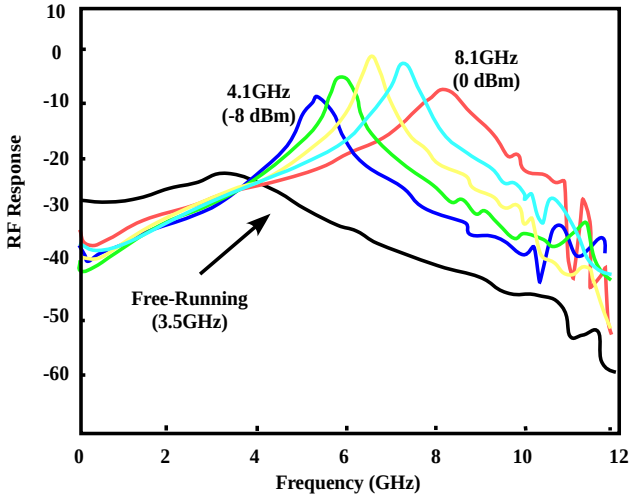

Figure 1.18: Improved frequency response of an injection-locked VCSEL emitting at 1.55μm. The VCSEL is injection-locked using a DFB laser [64].

Several optical injection-locking studies regarding semiconductor lasers have reported frequency-chirp reduction [11], [68], [66] increased RF link gain [66], [69], improved relative intensity noise [70], [71], [72], [73] and diminished non-linear distortion [66], [62].

Although the utilization of a DFB laser to injection-lock a VCSEL is excellent for demonstration of phenomena related to optical injection-locking, its practical application presents two major drawbacks. Without immediately entering into the details of these drawbacks, it can be logically inferred that both these drawbacks are related to the utilization of the DFB laser. First of all the physical symmetry of the two lasers used is not the same. The VCSELs are a vertical emission device while the DFB lasers emit in the horizontal direction. This asymmetry renders the integration of an optical injection-locking system consisting of a DFB laser and a VCSEL very difficult. The second reason, of course, is the cost. One of the reasons of employing VCSELs in optical networks for high-speed data communication is their cost-effectiveness. Utilization of a DFB laser to improve the transmission and the

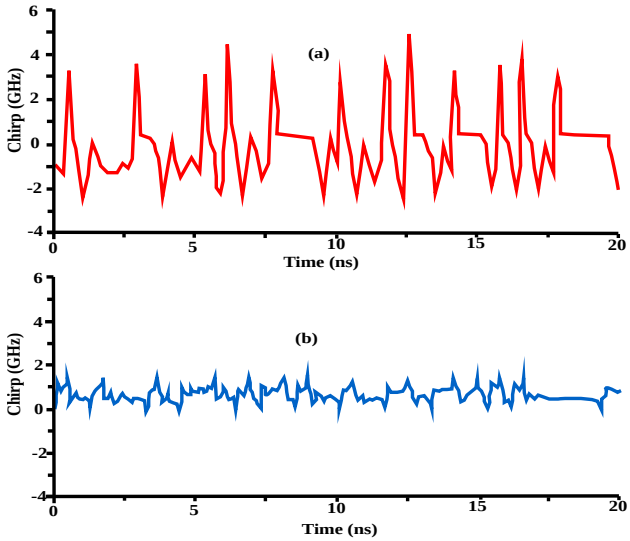

Figure 1.19: Comparison between the chirp of (a) a directly modulated free-running and (b) an injection-locked VCSEL. The VCSEL is injection-locked using a DFB laser [64].

component characteristics compromises this very objective. Due to these reasons despite all these advances regarding this very potent combination of semiconductor lasers and optical injection-locking, the phenomenon and its practical applications have not got any commercial breakthrough as yet.

With the arrival of Vertical-Cavity Surface-Emitting Lasers (VCSELs) on the commercial scene as low-cost, integrable sources, the efforts to revive the optical injection-locking phenomena were once again undertaken and follower VCSEL resonance frequencies ranging from 27 Ghz to 107 GHz have been reported in recent years [66], [74], [67], [75]. The problem of non-integrability however is still unresolved due to the utilization of a distributed feedback (DFB) laser as master optical source to injection-lock a follower VCSEL. The DFB lasers have horizontal optical cavities. This physical asymmetry renders the monolithic integration very complicated.

On the other hand the utilization of a powerful DFB laser compromises the economy of the setup by increasing the cost dramatically and fails the purpose of using a VCSEL in the first place. Clearly the solution to afore-mentioned problems would be to try a VCSEL-by-VCSEL optical injection-locking approach.

Bibliography

[1] C. Huygens, *Horologium Oscillatorium*. Observatoire de Paris, 1866.

[2] R. Adler, "A Study of Locking Phenomena in Oscillators," *Proceedings of the IEEE*, vol. 61, no. 10, pp. 1380–1385, Oct. 1973.

[3] R. Pantell, "The Laser Oscillator With An External Signal," *Proceedings of the IEEE*, vol. 53, no. 5, pp. 474–477, May 1965.

[4] H. Stover and W. Steier, "Locking of Laser Oscillators by Light Injection," *Applied Physics Letters*, vol. 8(4), p. 91, 1966.

[5] C. Buczek and R. Freiberg, "Hybrid Injection-Locking of Higher Power CO_2 Lasers," *IEEE Journal of Quantum Electronics*, vol. Vol. 8, No. 7, pp. pp. 641–650, Jul 1972.

[6] S. Kobayashi and T. Kimura, "Coherence of Injection Phase-Locked AlGaAs Semiconductor Laser," *Electronics Letters*, vol. 16, no. 17, pp. 668–670, 14 1980.

[7] ——, "Optical Phase Modulation in an Injection Locked AlGaAs Semiconductor Laser," *IEEE Transactions on Microwave Theory and Techniques*, vol. 82, no. 10, pp. 1650–1657, Oct 1982.

[8] ——, "Optical FM Signal Amplification by Injection Locked and Resonant Type Semiconductor Laser Amplifiers," *IEEE Transactions on Microwave Theory and Techniques*, vol. 82, no. 4, pp. 421–427, Apr 1982.

[9] S. Kasapi, S. Lathi, and Y. Yamamoto, "Sub-shot-noise frequency-modulation spectroscopy by use of amplitude-squeezed light from semiconductor lasers," *J. Opt. Soc. Am. B*, vol. 17, no. 2, pp. 275–279, 2000.

[10] P. Gallion, H. Nakajima, G. Debarge, and C. Chabran, "Contribution of spontaneous emission to the linewidth of an injection-locked semiconductor laser," *Electronics Letters*, vol. 21, no. 14, pp. 626–628, 4 1985.

[11] C. Lin and F. Mengel, "Reduction of Frequency Chirping and Dynamic Linewidth in High-Speed Directly Modulated Semiconductor Lasers by Injection Locking," *Electronics Letters*, vol. 20, no. 25, pp. 1073–1075, 6 1984.

[12] N. Olsson, H. Temkin, R. Logan, L. Johnson, G. Dolan, J. van der Ziel, and J. Campbell, "Chirp-Free Transmission Over 82.5 km of Single Mode Fibers at 2 Gbit/s with Injection Locked DFB Semiconductor Lasers," *Journal of Lightwave Technology*, vol. 3, no. 1, pp. 63–67, Feb 1985.

[13] C. Lin, J. Andersen, and F. Mengel, "Frequency chirp reduction in a 2.2 Gbit/s directly modulated InGaAsP semiconductor laser by CW injection," *Electronics Letters*, vol. 21, no. 2, pp. 80–81, 17 1985.

[14] R. Lang, "Injection Locking Properties of a Semiconductor Laser," *IEEE Journal of Quantum Electronics*, vol. 18, no. 6, pp. 976–983, Jun 1982.

[15] K. Kurokawa, "Injection Locking of Solid-Sate Oscillators," *Proceedings of the IEEE*, vol. Vol. 61, No. 10, pp. 1386–1410, 1973.

[16] C. Henry, N. Olsson, and N. Dutta, "Locking Range and Stability of Injection Locked 1.54μm InGaAsp Semiconductor Lasers," *IEEE Journal of Quantum Electronics*, vol. 21, no. 8, pp. 1152–1156, Aug 1985.

[17] F. Mogensen, H. Olesen, and G. Jacobsen, "Locking Conditions and Stability Properties for a Semiconductor Laser with External Light Injection," *IEEE Journal of Quantum Electronics*, vol. 21, no. 7, pp. 784–793, Jul 1985.

[18] T. Simpson, J. Liu, and A. Gavrielides, "Bandwidth enhancement and broadband noise reduction in injection-locked semiconductor lasers," *IEEE Photonics Technology Letters*, vol. 7, no. 7, pp. 709–711, Jul 1995.

[19] X. J. Meng, T. Jung, T. Chau, and M. Wu, "Gain and bandwidth enhancement of directly modulated analog fiber optic links using injection-locked gain-coupled DFB lasers," *International Topical Meeting on Microwave Photonics, 1999. MWP '99*, pp. 141–144 vol.1, 1999.

[20] S. M. Sze, *Physics of Semiconductor Devices, Second Edition.* John Wiley & Sons Inc., 1981.

[21] H. Soda, K. Iga, C. Kitahara, and Y. Suematsu, "GaInAsP/InP Surface Emitting Injection Lasers," *Japanese Journal of Applied Physics*, vol. 18, no. 12, pp. 2329–2330, 1979.

[22] J. Jewell, J. Harbison, A. Scherer, Y. Lee, and L. Florez, "Vertical-cavity surface-emitting lasers: Design, growth, fabrication, characterization," *IEEE Journal of Quantum Electronics*, vol. 27, no. 6, pp. 1332–1346, Jun 1991.

[23] Y. Lee, J. Jewell, A. Scherer, S. McCall, J. Harbison, and L. Florez, "Room-temperature continuous-wave vertical-cavity single-quantum-well microlaser diodes," *Electronics Letters*, vol. 25, no. 20, pp. 1377–1378, Sept. 1989.

[24] T. Baba, Y. Yogo, K. Suzuki, F. Koyama, and K. Iga, "Near room temperature continuous wave lasing characteristics of GaInAsP/InP surface emitting laser," *Electronics Letters*, vol. 29, no. 10, pp. 913–914, May 1993.

[25] M. Grabherr, B. Weigl, G. Reiner, and K. Ebeling, "Comparison of Proton Implanted and Selectively Oxidized Vertical-Cavity Surface-Emitting Lasers," in *Conference on Lasers and Electro-optics, 1996. CLEO/Europe.*, Sep 1996, pp. 165–165.

[26] D. L. Boiko, G. M. Weigl, G. M. Stephan, and P. Besnard, "Fast Polarization Switching with Memory Effect in a Vertical-Cavity Surface Emitting Laser Subject to Modulated Optical Injection," *Journal of Applied Physics*, vol. 86, no. 8, pp. 4096–4099, 1999.

[27] S. Blin, C. Guignard, R. Gabet, G. M. Stephan, M. Bondiou, and P. Besnard, "Phase and Spectral Properties of Optically-Injected Semi-Conductor Lasers," *Compte Rendu Physique*, vol. 4, no. 6, pp. 687–699, 2003.

[28] F. Robert, M. L. Chares, G. Stephan, and P. Besnard, "Polarization Control in a Vertical-Cavity Surface-Emitting Laser Submitted to Optical Feedback," *Annals of Telecommunications*, vol. 52, no. 11-12, pp. 575–587, 2003.

[29] S. Adachi, "GaAs, AlAs, and $Al_xGa_{1-x}As$ Material parameters for use in research and device applications," *Journal of Applied Physics*, vol. 58, no. 3, pp. R1–R29, 1985.

[30] G. P. Agrawal and N. K. Dutta, *Semiconductor Lasers*. Van Nostrand Reinhold, 1993.

[31] R. Shau, M. Ortsiefer, J. Rosskopf, G. Boehm, C. Lauer, M. Maute, and M.-C. Amann, "Long-wavelength InP-based VCSELs with buried tunnel junction: properties and applications," *Vertical-Cavity Surface-Emitting Lasers VIII*, vol. 5364, no. 1, pp. 1–15, 2004.

[32] J. Piprek, *Semiconductor Optoelectronic Devices. Introduction to Physics and Simulation*. Academic Press, 2003.

[33] L. Esaki, "Long journey into tunneling," *Proceedings of the IEEE*, vol. 62, no. 6, pp. 825–831, June 1974.

[34] R. L. Batdorf, G. C. Dacey, R. L. Wallace, and D. J. Walsh, "Esaki Diode in InSb," *Journal of Applied Physics*, vol. 31, no. 3, pp. 613–614, 1960.

[35] A. G. Chynoweth, W. L. Feldman, and R. A. Logan, "Excess Tunnel Current in Silicon Esaki Junctions," *Physics Review*, vol. 121, p. 684, 1961.

[36] C. A. Burrus, "Indium Phosphide Esaki Diodes," *Solid-State Electronics*, vol. 5, p. 357, 1962.

[37] N. Holonyak and I. Lesk, "Gallium-Arsenide Tunnel Diodes," *Proceedings of the IRE*, vol. 48, no. 8, pp. 1405–1409, Aug. 1960.

[38] P. Salet, F. Gaborit, P. Pagnod-Rossiaux, A. Plais, E. Derouin, J. Pasquier, and J. Jacquet, "Room temperature pulsed operating of 1.3 μm vertical cavity lasers including bottom InGaAsP/InP multilayer bragg mirrors," *Electronics Letters*, vol. Vol. 33 No. 24, pp. 2048–2049, 1997.

[39] I. Dias, B. Nabet, A. Kohl, J. Benchimol, and J. Harmand, "Electrical and optical characteristics of n-type-doped distributed Bragg mirrors on InP," *IEEE Photonics Technology Letters*, vol. 10, no. 6, pp. 763–765, Jun 1998.

[40] J. Boucart, C. Starck, F. Gaborit, A. Plais, N. Bouche, E. Derouin, L. Goldstein, C. Fortin, D. Carpentier, P. Salet, F. Brillouet, and J. Jacquet, "1-mW CW-RT monolithic VCSEL at 1.55 μm," *IEEE Photonics Technology Letters*, vol. 11, no. 6, pp. 629–631, Jun 1999.

[41] Y. Qian, Z. Zhu, Y. Lo, H. Hou, M. Wang, and W. Lin, "1.3-μm Vertical-cavity surface-emitting lasers with double-bonded GaAs-AlAs Bragg mirrors," *IEEE Photonics Technology Letters*, vol. 9, no. 1, pp. 8–10, Jan. 1997.

[42] M. Larson, M. Kondow, T. Kitatani, K. Nakahara, K. Tamura, H. Inoue, and K. Uomi, "GaInNAs-GaAs long-wavelength vertical-cavity surface-emitting laser diodes," *IEEE Photonics Technology Letters*, vol. 10, no. 2, pp. 188–190, Feb 1998.

[43] N. Margalit, K. Black, Y. Chiu, E. Hegblom, K. Streubel, P. Abraham, M. Anzlowar, J. Bowers, and E. Hu, "Top-emitting double-fused 1.5 μm vertical cavity lasers," *Electronics Letters*, vol. 34, no. 3, pp. 285–287, Feb 1998.

[44] S. Rapp, F. Salomonsson, J. Bentell, I. Sagnes, H. Moussa, C. Meriadec, R. Raj, K. Streubel, and M. Hammar, "Near room-temperature continuous-wave operation of electrically pumped 1.55 μm vertical cavity lasers with InGaAsP/InP bottom mirror," *Electronics Letters*, vol. 35, no. 1, pp. 49–50, Jan 1999.

[45] C. Kazmierski, J. Debray, R. Madani, J. Sagnes, A. Ougazzaden, N. Bouadma, J. Etrillard, F. Alexandre, and M. Quillec, "Pulse lasing at 1.56 μm of all-monolithic InGaAlAs-InP vertical cavity lasers," *Electronics Letters*, vol. 35, no. 10, pp. 811–812, May 1999.

[46] J. Kim, E. Hall, O. Sjolund, and L. Coldren, "Room-temperature, electrically-pumped, multiple-active-region VCSELs with high differential efficiency at 1.55 μm," *12th Annual Meeting of Lasers and Electro-Optics Society 1999. IEEE LEOS '99.*, vol. 1, pp. 141–142 vol.1, 1999.

[47] E. Hall, G. Almuneau, J. Kim, O. Sjolund, H. Kroemer, and L. Coldren, "Electrically-pumped, single-epitaxial VCSELs at 1.55 μm with Sb-based mirrors," *Electronics Letters*, vol. 35, no. 16, pp. 1337–1338, Aug 1999.

[48] M. Yamada, T. Anan, K. Kurihara, K. Nishi, K. Tokutome, A. Kamei, and S. Sugou, "Room temperature low-threshold CW operation of 1.23 μm GaAsSb VCSELs on GaAs substrates," *Electronics Letters*, vol. 36, no. 7, pp. 637–638, Mar 2000.

[49] T. Kageyama, T. Miyamoto, S. Makino, Y. Ikenaga, N. Nishiyama, A. Matsutani, F. Koyama, and K. Iga, "Room temperature continuous-wave operation of GaInNAs/GaAs VCSELs grown by chemical beam epitaxy with output power exceeding 1 mW," *Electronics Letters*, vol. 37, no. 4, pp. 225–226, Feb 2001.

[50] E. Hall, S. Nakagawa, G. Almuneau, J. Kim, and L. Coldren, "Selectively etched undercut apertures in AlAsSb-based VCSELs," *IEEE Photonics Technology Letters*, vol. 13, no. 2, pp. 97–99, Feb 2001.

[51] M. Ortsiefer, M. Lohner, R. Shau, G. Böhm, and M.-C. Amann, "Low-resistance InGaAs tunnel junctions on InP for long-wavelength VCSELs," in *Semiconductor and Integrated Optoelectronics Conference (SIOE), Cardiff*, 1999.

[52] M. Ortsiefer, R. Shau, G. Bohm, F. Kohler, and M.-C. Amann, "Room-temperature operation of index-guided 1.55 μm InP-based vertical-cavity surface-emitting laser," *Electronics Letters*, vol. 36, no. 5, pp. 437–439, Mar 2000.

[53] N. Margalit, D. Babic, K. Streubel, R. Mirin, R. Naone, J. Bowers, and E. Hu, "Submilliamp long wavelength vertical cavity lasers," *Electronics Letters*, vol. 32, no. 18, pp. 1675–, Aug 1996.

[54] A. Black, A. Hawkins, N. Margalit, D. Babic, J. Holmes, A.L., Y.-L. Chang, P. Abraham, J. Bowers, and E. Hu, "Wafer fusion: materials issues and device results," *IEEE Journal of Selected Topics in Quantum Electronics*, vol. 3, no. 3, pp. 943–951, Jun 1997.

[55] A. Syrbu, V. Iakovlev, G. Suruceanu, A. Caliman, A. Mereuta, A. Mircea, C.-A. Berseth, E. Diechsel, J. Boucart, A. Rudra, and E. Kapon, "VCSELs Emitting in the 1310-nm Waveband for Novel Optical Communication Applications," *SPIE Vertical-Cavity Surface-Emitting Lasers IX*, vol. 5737, no. 1, pp. 167–173, 2005.

[56] A. Syrbu, V. Iakovlev, G. Suruceanu, A. Caliman, A. Rudra, A. Mircea, A. Mereuta, S. Tadeoni, C.-A. Berseth, M. Achtenhagen, J. Boucart, and E. Kapon, "1.55-μm optically pumped wafer-fused tunable VCSELs with 32-nm tuning range," *IEEE Photonics Technology Letters*, vol. 16, no. 9, pp. 1991–1993, Sept. 2004.

[57] R. Koda, "All-Epitaxial, Long-Wavelength, Vertical-Cavity Surface-Emitting Lasers using Bipolar Cascaded Active Region for High Differential Quantum Efficiency," Ph.D. dissertation, UNIVERSITY OF CALIFORNIA Santa Barbara, 2005.

[58] M.-R. Park, O.-K. Kwon, W.-S. Han, K.-H. Lee, S.-J. Park, and B.-S. Yoo, "All-epitaxial InAlGaAs-InP VCSELs in the 1.3-1.6-μm Wavelength Range for CWDM Band Applications," *IEEE Photonics Technology Letters*, vol. 18, no. 16, pp. 1717–1719, Aug. 2006.

[59] A. Rissons and J. Mollier, *Optical Access Networks and Advanced Photonics: Technologies and Deployment Strategies*, G. A. Heliotis and I. P. Chochliouros, Eds. Information Science Reference, 2009, no. 978-1-60566-707-2.

[60] A. Bacou, A. Rissons, and J.-C. Mollier, "Spectral behavior of long wavelength VCSELs," *SPIE Vertical-Cavity Surface-Emitting Lasers XII*, vol. 6908, no. 1, 2008.

[61] T. Simpson, J. Liu, and A. Gavrielides, "Small-signal analysis of modulation characteristics in a semiconductor laser subject to strong optical injection," *IEEE Journal of Quantum Electronics*, vol. 32, no. 8, pp. 1456–1468, Aug 1996.

[62] X. Meng, T. Chau, D. Tong, and M. Wu, "Suppression of Second Harmonic Distortion in Directly Modulated Distributed Feedback Lasers by External Light Injection," *Electronics Letters*, vol. 34, no. 21, pp. 2040–2041, Oct 1998.

[63] C.-H. Chang, L. Chrostowski, C. Chang-Hasnain, and W. Chow, "Study of long-wavelength VCSEL-VCSEL injection locking for 2.5-Gb/s transmission," *IEEE Photonics Technology Letters*, vol. 14, no. 11, pp. 1635–1637, Nov 2002.

[64] C.-H. Chang, L. Chrostowski, and C. Chang-Hasnain, "Injection locking of VCSELs," *IEEE Journal of Selected Topics in Quantum Electronics*, vol. 9, no. 5, pp. 1386–1393, Sept.-Oct. 2003.

[65] L. Chrostowski, C.-H. Chang, and C. Chang-Hasnain, "Enhancement of Dynamic Range in 1.55μm VCSELs Using Injection Locking," *IEEE Photonics Technology Letters*, vol. 15, no. 4, pp. 498–500, April 2003.

[66] L. Chrostowski, X. Zhao, and C. Chang-Hasnain, "Microwave Performance of Optically Injection-locked VCSELs," *IEEE Transactions on Microwave Theory and Techniques*, vol. 54, no. 2, pp. 788–796, Feb. 2006.

[67] L. Chrostowski, F. B., W. Hoffman, M.-C. Amann, S. Wieczorek, and W. Chow, "40 GHz Bandwidth and 64 GHz Resonance Frequency in Injection-Locked 1.55 μm VCSELs," *IEEE Journal of Journal of Selected Topics in Quantum Electronics*, vol. Vol. 13, No. 5, 2007.

[68] H. Toba, Y. Kobayashi, K. Yanagimoto, H. Nagai, and M. Nakahara, "Injection-locking Technique Applied to a 170 km Transmission Experiment at 445.8 Mbit/s," *Electronics Letters*, vol. 20, no. 9, pp. 370–371, 26 1984.

[69] H.-K. Sung, T. Jung, D. Tishinin, K. Liou, W. Tsang, and M. Wu, "Optical Injection-Locked Gain-Lever Distributed Bragg Reflector Lasers With Enhanced RF Performance," *IEEE International Topical Meeting on Microwave Photonics. MWP'2004.*, pp. 225–228, Oct. 2004.

[70] L. Chrostowski, C.-H. Chang, and C. Chang-Hasnain, "Reduction of Relative Intensity Noise and Improvement of Spur-Free Dynamic Range of an Injection-Locked VCSEL," *The 16th Annual Meeting of the IEEE Lasers and Electro-Optics Society. LEOS 2003.*, vol. 2, pp. 706–707 vol.2, Oct. 2003.

[71] N. Schunk and K. Petermann, "Noise Analysis of Injection-Locked Semiconductor Injection Lasers," *IEEE Journal of Quantum Electronics*, vol. 22, no. 5, pp. 642–650, May 1986.

[72] M. Espana-Boquera and A. Puerta-Notario, "Noise Effects in Injection Locked Laser Simulation: Phase Jumps and Associated Spectral Components," *Electronics Letters*, vol. 32, no. 9, pp. 818–819, Apr 1996.

[73] G. Yabre, H. De Waardt, H. van den Boom, and G.-D. Khoe, "Noise Characteristics of Single-Mode Semiconductor Lasers Under External Light Injection," *IEEE Journal of Quantum Electronics*, vol. 36, no. 3, pp. 385–393, Mar 2000.

[74] X. Zhao, M. Moewe, L. Chrostowski, C.-H. Chang, R. Shau, M. Ortsiefer, M.-C. Amann, and C. Chang-Hasnain, "28 GHz Optical Injection-Locked 1.55μm VCSELs," *IEE Electronic Letters*, vol. Vol. 40 No. 8, 15 April 2004.

[75] X. Zhao, E. K. Lau, D. Parekh, H.-K. Sung, W. Hofmann, M. C. Amann, M. C. Wu, and C. J. Chang-Hasnain, "107-GHz Resonance Frequency of 1.55μm VCSELs Under Ultra-high Optical Injection Locking," in *OSA/CLEO*, 2008.

Chapter 2 Simulation of Optically Injection-Locked VCSELs

2.1 VCSEL Rate Equations

The previous chapter introduced the overall historical background of the subject and the motivation for undertaking this research work. In this chapter we will present a complete theoretical analysis of the optical injection-locking phenomenon in semiconductor lasers.

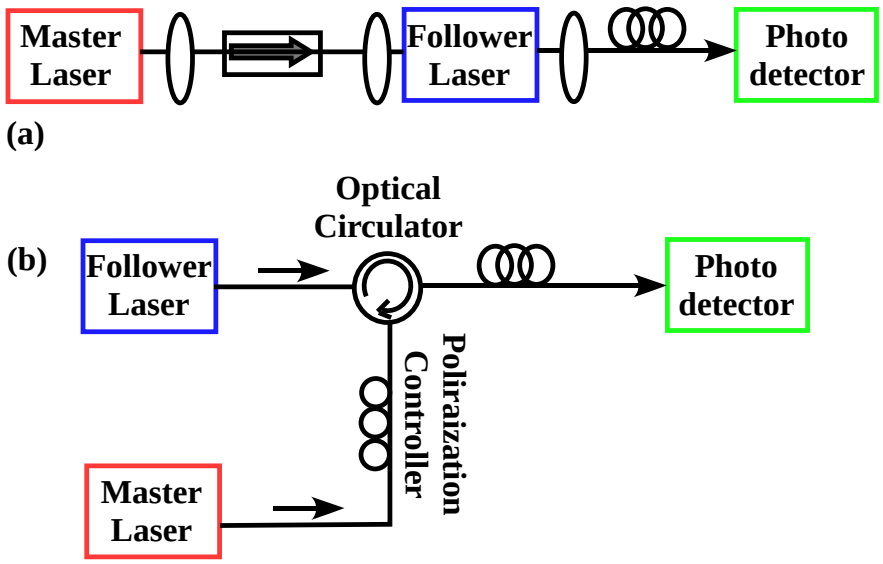

Figure 2.1: A general schematic representation of the measurement setup employed for injection-locking experiments. (a) The transmission setup, usually employed for double edge-emitting semiconductor lasers, (b) The reflection setup, usually employed for single-side emission lasers.

A semiconductor laser cavity is essentially a resonator and its input (electrons) and output (photons) can be demonstrated to be interrelated to each other via cavity parameters. Like any other resonator cavity, the quality factor "Q" and the resonance frequency of this cavity can be controlled by manipulating its physical dimensions or intrinsic parameters. Ordinarily, the only externally manipulable variable is the electron concentration that can be varied by changing the bias current. During the optical injection-locking process the internal parameters of the cavity are changed by varying the photon concentration inside the cavity. Since the locking effect is the result of interaction between two optical fields, the phase difference between the master and follower VCSELs can also be varied to achieve the desired effect.

Classical mathematical representation of the cavity parameter interdependence is in the form of two time-varying simultaneous differential equations, commonly referred to as the laser, or in our case, "VCSEL Rate Equations". The rate equations for a free-running VCSEL are as follows:

$$\frac{dN(t)}{dt} = \frac{\eta_i I}{qV_{act}} - (A + BN(t) + CN(t)^2)N(t) - v_g GS(t) \tag{2.1}$$

$$\frac{dS(t)}{dt} = \Gamma\beta BN(t)^2 + \Gamma v_g GS(t) - \frac{S(t)}{\tau_P} \tag{2.2}$$

Where $N(t)$ and $S(t)$ are the electron and photon densities, η_i the internal quantum effciency, q the electron charge, V_{act} the active region volume, v_g the group velocity, β the spontaneous emission coefficient, Γ the confinement factor and τ_P the photon lifetime.

The spontaneous emission rate, R_{sp} is defined in terms of the constants A, B and C where A represents the Shockly-Read-Hall non-radiative recombination coefficient, B the bimolecular recombination coefficient and C the Auger non-radiative recombination coefficient.

The gain G can be expressed as

$$G = a_0 \frac{N(t) - N_{tr}}{1 + \epsilon S(t)} \tag{2.3}$$

where N_{tr} is the transparency carrier density, a_0 the differential gain coefficient and ϵ the gain compression factor.

A third equation describing the phase behavior of the device can be introduced as follows:

$$\frac{d\phi(t)}{dt} = \frac{\alpha_H \Gamma v_g a_0}{2}(N(t) - N_{tr}) \tag{2.4}$$

α_H is the "Phase-Amplitude" coupling factor and is referred to as "Henry's Factor". It might be important to note here that equation 2.4 is not a coupled equation i.e. the term $\phi(t)$ does not appear in equations 2.1 and 2.2.

Lang proposed the utilization of three equations, instead of two, to model an optically injection-locked system [1]. Lang's equations coupled the electric field variations in the cavity directly to carrier and phase variations and as such rendered the physical interpretation of the phenomenon somewhat cumbersome. In 1985, P. Gallion et al. presented the optical injection-locking rate equations that replaced cavity electrical field by photon number [2], [3].

Following the injection of optical power in the optical cavity, the dynamics of the follower laser change. This change can be mathematically presented by modifying the VCSEL rate equations to compensate for optical injection.

$$\frac{dN(t)}{dt} = \frac{\eta I}{qV_{act}} - (A + BN(t) + CN(t)^2)N(t) - v_g GS(t) \tag{2.5}$$

$$\frac{dS(t)}{dt} = \Gamma v_g GS(t) - \frac{S(t)}{\tau_P} + \frac{v_g}{L}\sqrt{S(t)S_{inj}}\cos(\theta) + \Gamma B\beta N(t)^2 \tag{2.6}$$

$$\frac{d\phi(t)}{dt} = \frac{\alpha_H \Gamma v_g a_0}{2}(N(t) - N_{tr}) - \Delta\omega - \frac{v_g}{2L}\sqrt{\frac{S_{inj}}{S(t)}}\sin(\theta) \tag{2.7}$$

It must be remarked that while the equation concerning the carrier density remains unchanged, the equations regarding the phase and the photon density are modified to accommodate for the effects of external light injection. Two very important parameters of note, S_{inj} and θ, are added to equations 2.6 and 2.7. S_{inj} represents the photon density injected inside the follower VCSEL optical cavity while θ denotes the phase difference between the master and follower optical fields so that:

$$\theta = \phi_{inj} - \phi(t) \tag{2.8}$$

Another parameter of note is $\Delta\omega$ or the "Frequency Detuning". It is defined as

$$\Delta\omega = \omega_{Master} - \omega_{Follower} \tag{2.9}$$

Apart from frequency detuning, phase difference and injected optical power, the fourth parameter which characterizes an optically injection-locked system is the "coupling coefficient" of a laser. It is defined as k_c and can be expressed mathematically as

$$k_c = \frac{v_g}{2L} \tag{2.10}$$

This coefficient describes the rate at which the injected electric field adds to the follower cavity electric field as a function of the VCSEL optical cavity length. L is the length of the VCSEL optical cavity.

2.2 Locking Range Calculations

Solving equations (2.6) and (2.7) in the steady-state regime which renders $\frac{dS(t)}{dt}$ and $\frac{d\phi(t)}{dt}$ equal to zero gives the very important parametric equation:

$$\Delta\omega \;=\; k_c\sqrt{\frac{S_{inj}}{S}}\Big[sin(\theta) - \alpha_H cos(\theta)\Big] \tag{2.11}$$

The dependance of equation(2.11) on α_H can be elaborated by using the linear combination property for sines and cosines. Using this property we can write that:

$$Asin(\theta) + Bcos(\theta) \;=\; Csin(\theta + D) \tag{2.12}$$

where

$$sin(D) \;=\; \frac{A}{C} \tag{2.13}$$

$$cos(D) \;=\; \frac{B}{C} \tag{2.14}$$

$$C \;=\; \sqrt{A^2 + B^2} and \tag{2.15}$$

$$D \;=\; \tan^{-1}\left(\frac{B}{A}\right) \tag{2.16}$$

Introducing $A = 1$ and $B = \alpha_H$ and using equations 2.12 to 2.16 we can modify equation 2.11 to obtain:

$$\Delta\omega \;=\; k_c\sqrt{\frac{S_{inj}}{S}}\Big[\sqrt{1+\alpha_H^2}\Big] sin\big(\theta - \tan^{-1}\alpha_H\big) \tag{2.17}$$

This relation is important because it helps the calculation of effective locking bandwidth of an injection-locked system. Moreover it can be deduced that due to the presence of the sine function, the inequality is limited to the range of:

$$\big|\Delta\omega\big| \;\leq\; k_c\sqrt{\frac{S_{inj}}{S}}\Big[\sqrt{1+\alpha_H^2}\Big] \tag{2.18}$$

On the other hand, following the discussion in [4] and [5] it appears that the oscillation limit for θ is between $\frac{-\pi}{2}$ and $\frac{\pi}{2}$. $\Delta\omega$ is then bounded by:

$$-\,k_c\sqrt{\frac{S_{inj}}{S}}\Big[\sqrt{1+\alpha_H^2}\Big] \leq \Delta\omega \;\leq k_c\sqrt{\frac{S_{inj}}{S}} \tag{2.19}$$

The assymetry of the locking range can be explained both mathematically and physically. Mathematically speaking , if we observe (2.19), we can see that due to the multiplication with the term $\sqrt{1+\alpha_H^2}$ on the left hand side, this relation becomes asymmetric with

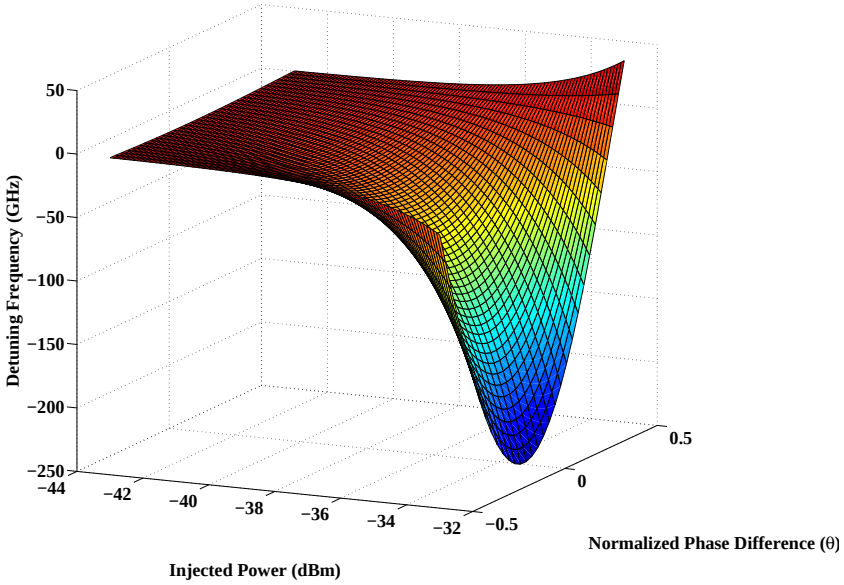

Figure 2.2: Calculated locking range of a long wavelength VCSEL with $\alpha_H = 7$.

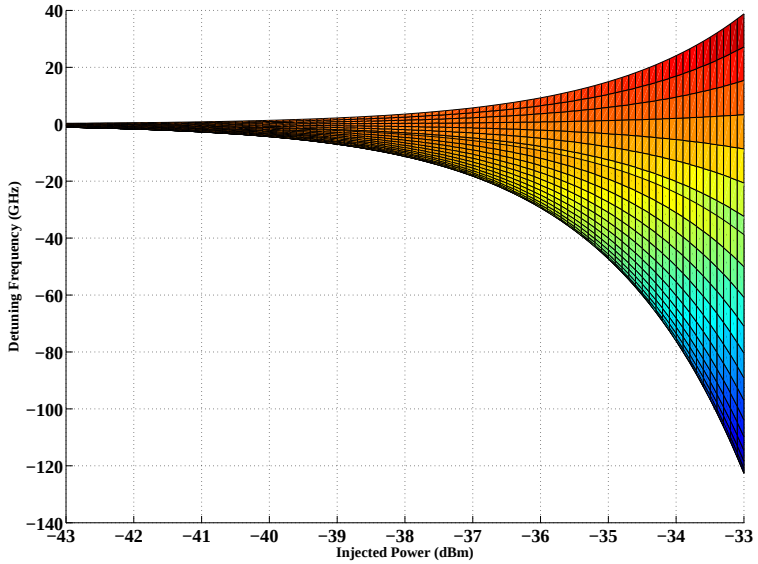

Figure 2.3: 2D presentation of calculated locking range of a long wavelength VCSEL with $\alpha_H = 3$ showing the locking-range dependence on injected optical power.

respect to α_H. Physically speaking, during the injection-locking of a semiconductor laser the increased photon population changes the refractive index and leads to a cavity wavelength shift in the longer wavelength direction and finally an asymmetric locking range. Calculated locking-ranges for two different values of α_H are presented in Figures. 2.2 and 2.3.

It can be observed from Figures. 2.2 and 2.3 that a higher value of α_H leads to higher locking-range. The same result can be obtained from observing equation (2.11). A higher value of α_H favors locking in the negative frequency detuning (or positive wavelength detuning) range.

In terms of locking-range characteristics, VCSELs are different from EELs. Locking-range determines the extent of frequency enhancement of an optically injection-locked laser. Equation (2.11) shows that the locking-range depends on injected power and coupling-coefficient k_c. Therefore mathematically it can be stated that the locking-range follows the variation of the term $k_c\sqrt{\frac{S_{inj}}{S}}$. Since a VCSEL cavity is much shorter than an EEL cavity, VCSELs have typically very high values of k_c (equation 2.10) as compared to those of conventional lasers. This implies that VCSEL locking-ranges are higher compared to EEL locking-ranges and can potentially lead to much higher resonance frequencies.

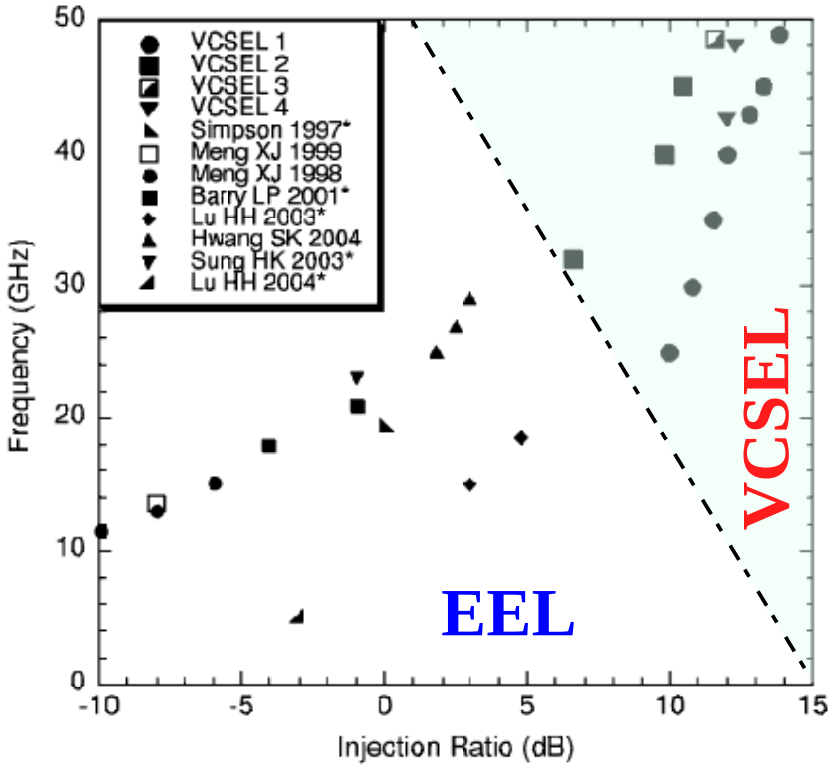

Figure 2.4: Resonance frequencies reported by different groups working on optical injection-locking of semiconductor lasers [6]. The shaded region signifies VCSELs while the un-shaded region represents the EELs.

Fig. 2.4 presents the comparison between resonance frequencies of different injection

locked systems. It is important to note that Simpson [7], Meng [8], Sung [9] and Barry [10] have presented the results of optical injection-locking of EELs. Despite the fact that EELs have larger emission windows as compared to VCSELs, which facilitate optical power injection inside the follower laser cavity, resonance frequencies reported by Chrostowski et. al for VCSELs 1, 2, 3 and 4 in Fig. 2.4 far exceed the resonance frequencies obtained using EELs [6]. This is due to difference in value of k_c for EELs and VCSELs. A typical k_c value for a VCSEL is of the order of 10^{13} while that of an EEL is of the order of 10^{10} which explains the difference in locking-ranges and consequently resonance frequencies.

2.3 Small Signal Analysis

We begin by presenting once again the "Modified VCSEL Rate Equations". The small signal analysis is performed to derive the S_{21} response of an injection-locked VCSEL.

$$\frac{dN(t)}{dt} = \frac{\eta_i I}{qV_{act}} - (A + BN(t) + CN(t)^2)N(t) - v_g G S(t) \tag{2.20}$$

$$\frac{dS(t)}{dt} = \Gamma v_g G S(t) - \frac{S(t)}{\tau_P} + \frac{v_g}{L}\sqrt{S(t)S_{inj}}\cos(\theta) + \Gamma B\beta N(t)^2 \tag{2.21}$$

$$\frac{d\phi(t)}{dt} = \frac{\alpha_H \Gamma v_g a_0}{2}(N(t) - N_{tr}) - \Delta\omega - \frac{v_g}{2L}\sqrt{\frac{S_{inj}}{S(t)}}\sin(\theta) \tag{2.22}$$

Consider that a sinusoidal signal $\Delta I e^{j\omega t}$ modulates a laser biased at current $\overline{I}$. The resulting expression for current I then becomes:

$$I(t) = \overline{I} + \Delta I e^{j\omega t} \tag{2.23}$$

Similarly, the carrier, photon and phase variations can be described as follows:

$$N(t) = \overline{N} + \Delta N e^{j\omega t} \tag{2.24}$$

$$S(t) = \overline{S} + \Delta S e^{j\omega t} \tag{2.25}$$

$$\phi(t) = \overline{\phi} + \Delta\phi e^{j\omega t} \tag{2.26}$$

By putting

$$\dot{N} = \frac{dN}{dt} \tag{2.27}$$

$$\dot{S} = \frac{dS}{dt} \tag{2.28}$$

$$\dot{\phi} = \frac{d\phi}{dt} \tag{2.29}$$

we have

$$\Delta\dot{N}(I,N,S) = \frac{\partial\dot{N}}{\partial I}\cdot\Delta I + \frac{\partial\dot{N}}{\partial N}\cdot\Delta N + \frac{\partial\dot{N}}{\partial S}\cdot\Delta S \tag{2.30}$$

$$\Delta\dot{S}(N,S,\phi) = \frac{\partial\dot{S}}{\partial N}\cdot\Delta N + \frac{\partial\dot{S}}{\partial S}\cdot\Delta S + \frac{\partial\dot{N}}{\partial\phi}\cdot\Delta\phi \tag{2.31}$$

$$\Delta\dot{\phi}(N,S,\phi) = \frac{\partial\dot{\phi}}{\partial N}\cdot\Delta N + \frac{\partial\dot{\phi}}{\partial S}\cdot\Delta S + \frac{\partial\dot{\phi}}{\partial\phi}\cdot\Delta\phi \tag{2.32}$$

The gain, as defined in equation (2.3), contains both the carrier and the photon terms. Partial differentiation of the equation (2.3), with respect to the carrier and photon densities N and S, yields two new variables G_N and G_S, where G_N and G_S are defined as:

$$G_N = \frac{\partial G}{\partial N} = \frac{a_0}{1+\epsilon S} \tag{2.33}$$

$$G_S = -\frac{\partial G}{\partial S} = \frac{a_0\epsilon(N-N_{tr})}{(1+\epsilon S)^2} \tag{2.34}$$

Differentiating equation (2.5) , with respect to N, S and ϕ, therefore results in the following set of three equations:

$$\frac{\partial\dot{N}}{\partial N}\cdot\Delta N = (-(A+2BN+3CN^2)-v_gG_NS)\Delta N \tag{2.35}$$

$$\frac{\partial\dot{N}}{\partial S}\cdot\Delta S = (-v_gG+v_gG_SS)\Delta S \tag{2.36}$$

$$\frac{\partial\dot{N}}{\partial I}\cdot\Delta I = \frac{\eta_i}{qV_{act}}\Delta I \tag{2.37}$$

Similarly if we define a new variable ρ as:

$$\rho = \frac{v_g}{2L}\sqrt{\frac{S_{inj}}{S}} \tag{2.38}$$

and differentiate equation (2.6) with respect to N, S and ϕ, we have the following set of equations:

$$\frac{\partial\dot{S}}{\partial N}\cdot\Delta N = (\Gamma v_gG_NS-2\beta BN)\Delta N \tag{2.39}$$

$$\frac{\partial\dot{S}}{\partial S}\cdot\Delta S = (-\Gamma v_gG_SS+\rho cos(\theta))\Delta S \tag{2.40}$$

$$\frac{\partial\dot{S}}{\partial\phi}\cdot\Delta\phi = (-2\cdot\rho Ssin(\theta))\Delta\phi \tag{2.41}$$

The partial differentiation of the phase equation (2.7) with respect to N, S and ϕ results in the following set of equations.

$$\frac{\partial\dot{\phi}}{\partial N}\cdot\Delta N = \frac{\alpha_H\Gamma v_g a_0}{2}\Delta N \tag{2.42}$$

$$\frac{\partial\dot{\phi}}{\partial S}\cdot\Delta S = \frac{\rho sin(\theta)}{2S}\Delta S \tag{2.43}$$

$$\frac{\partial\dot{\phi}}{\partial \phi}\cdot\Delta \phi = -\rho cos(\theta)\Delta\phi \tag{2.44}$$

Linearised rate equations can then be expressed as

$$\Delta\dot{N} = \frac{\eta_i}{qV_{act}}\Delta I - \big(A+2BN+3CN^2+v_gG_NS\big)\Delta N - \big(v_gG-v_gG_SS\big)\Delta S \tag{2.45}$$

$$\Delta\dot{S} = \big(\Gamma v_gG_NS-2\beta BN\big)\Delta N - \big(\Gamma v_gGS-\rho cos(\theta)\big)\Delta S - \big(2\cdot\rho Ssin(\theta)\big)\Delta\phi \tag{2.46}$$

$$\Delta\dot{\phi} = \big(\frac{\alpha_H\Gamma v_g a_0}{2}\big)\Delta N + \big(\frac{\rho sin(\theta)}{2S}\big)\Delta S - \big(\rho cos(\theta)\big)\Delta\phi \tag{2.47}$$

Replacing the partial derivatives by intermediate variables gives

$$\Delta\dot{N} = \frac{\eta_i}{qV_{act}}\Delta I - \gamma_{NN}\Delta N - \gamma_{NS}\Delta S \tag{2.48}$$

$$\Delta\dot{S} = \gamma_{SN}\Delta N - \gamma_{SS}\Delta S - \gamma_{S\Phi}\Delta\phi \tag{2.49}$$

$$\Delta\dot{\phi} = \gamma_{\Phi N}\Delta N + \gamma_{\Phi S}\Delta S - \gamma_{\Phi\Phi}\Delta\phi \tag{2.50}$$

which can be readily arranged into a three equation matrix system as follows:

$$\frac{d}{dt}\begin{bmatrix}\Delta S\\ \Delta N\\ \Delta\Phi\end{bmatrix} = \begin{bmatrix}-\gamma_{SS} & \gamma_{SN} & -\gamma_{S\Phi}\\ -\gamma_{NS} & -\gamma_{NN} & \gamma_{N\Phi}\\ \gamma_{\Phi N} & \gamma_{\Phi S} & -\gamma_{\Phi\Phi}\end{bmatrix}\cdot\begin{bmatrix}\Delta S\\ \Delta N\\ \Delta\Phi\end{bmatrix} + \frac{\eta_i}{qV_{act}}\cdot\begin{bmatrix}0\\ \Delta I\\ 0\end{bmatrix} \tag{2.51}$$

Taking the Laplace transform of the equation set in order to pass from time-domain to frequency-domain, and arranging, yields [1]

$$\begin{bmatrix}\gamma_{SS}+j\omega & -\gamma_{SN} & \gamma_{S\Phi}\\ \gamma_{NS} & \gamma_{NN}+j\omega & 0\\ -\gamma_{\Phi S} & -\gamma_{\Phi N} & \gamma_{\Phi\Phi}+j\omega\end{bmatrix}\cdot\begin{bmatrix}\Delta\widetilde{S}\\ \Delta\widetilde{N}\\ \Delta\widetilde{\Phi}\end{bmatrix} = \frac{\eta_i\widetilde{I}}{V_{act}}\cdot\begin{bmatrix}0\\ 1\\ 0\end{bmatrix} \tag{2.52}$$

In order to solve this three-equation matrix system we have to calculate the determinant of the intermediate variable matrix

[1] Note that since equation 2.5 does not have a phase terms, $\gamma_{N\Phi}=0$.

$$\Lambda = \begin{vmatrix} \gamma_{SS} + j\omega & -\gamma_{SN} & \gamma_{S\Phi} \\ \gamma_{NS} & \gamma_{NN} + j\omega & 0 \\ -\gamma_{\Phi S} & -\gamma_{\Phi N} & \gamma_{\Phi\Phi} + j\omega \end{vmatrix} \tag{2.53}$$

where

$$\begin{aligned} \Lambda = & -j\omega^3 \\ & - \omega^2 \left(\gamma_{NN} + \gamma_{SS} + \gamma_{\Phi\Phi}\right) \\ & + j\omega \left(\gamma_{S\Phi}\gamma_{\Phi S} + \gamma_{SS}\gamma_{NN} + \gamma_{NS}\gamma_{SN} + \gamma_{NN}\gamma_{\Phi\Phi} + \gamma_{SS}\gamma_{\Phi\Phi}\right) \\ & + \left(\gamma_{S\Phi}\gamma_{\Phi S}\gamma_{NN} - \gamma_{S\Phi}\gamma_{NS}\gamma_{\Phi N} + \gamma_{SS}\gamma_{NN}\gamma_{\Phi\Phi} + \gamma_{SN}\gamma_{NS}\gamma_{\Phi\Phi}\right) \end{aligned} \tag{2.54}$$

Using the Kramer's rule, the photon density variation can be expressed as

$$\Delta\widetilde{S} = \frac{\eta_i \widetilde{I}}{qV_{act}} \cdot \frac{\begin{vmatrix} 0 & -\gamma_{SN} & \gamma_{S\Phi} \\ 1 & \gamma_{NN} + j\omega & 0 \\ 0 & -\gamma_{\Phi N} & \gamma_{\Phi\Phi} + j\omega \end{vmatrix}}{\Lambda} \tag{2.55}$$

Simplifying equation 2.55 leads to

$$\Delta\widetilde{S} = \frac{\eta_i \widetilde{I}}{qV_{act}} \cdot \frac{\left(\gamma_{SN}\gamma_{\Phi\Phi} - \gamma_{\Phi N}\gamma_{N\Phi}\right) + j\omega\gamma_{SN}}{\Lambda} \tag{2.56}$$

Equations 2.6 and 2.7 can alternatively be solved to obtain a relation in terms of the phase difference between two lasers and is presented below:

$$\theta \;=\; \sin^{-1}\left[\frac{\Delta\omega}{k_c\sqrt{\frac{S_{inj}}{S}}\sqrt{1+\alpha_H^2}} + \tan^{-1}\alpha_H\right] \tag{2.57}$$

Using equation 2.57 we can incorporate the effects of frequency detuning into the small-signal model of an injection-locked system since $\gamma_{\Phi\Phi}$, $\gamma_{\Phi S}$, $\gamma_{S\Phi}$ and γ_{SS} depend on θ.

2.3.1 Theory and Physical Explanation

The increase in resonance frequency is a combination of two factors extraneous to the follower laser and dependent on the injected light.

- The injection of photons in the follower laser cavity changes the carrier-photon equilibrium inside the cavity. The free-running follower laser cavity resonance that is represented by the photon and carrier densities is redefined due to external light injection. The increase in photon density affects the carrier density inside the follower laser cavity. The change in cavity resonance frequency due to carrier population density variation can be quantified using α_H; the linewidth enhancement factor that indicates the carrier-variation induced refractive index change and hence the amplitude-phase coupling.
  The consequence of the external photon-injection is hence a downshift in the laser cavity resonance frequency denoted as $\omega_{Downshifted}$ in this text.

- The second factor takes into account the difference between the master and the follower lasing frequencies. This difference is known as "frequency detuning" and could be defined as

$$\Delta\omega \quad = \quad \omega_{master} - \omega_{follower} \tag{2.58}$$

The detuning is said to be positive if the master laser has an emission frequency greater than that of the follower laser and is said to be negative if the reverse is true. Once locked the follower laser emits at the same frequency as the master laser.

The follower laser, therefore, in effect is experiencing two different phenomena at the same time. The external light injection has offset the cavity mode to a lower resonance frequency while the detuning has led to a high emission frequency. It is the difference between ω_{master} and $\omega_{Downshifted}$ that determines the value of enhanced resonance frequency, $\omega_{EnhancedResonance}$ of an optically injection-locked laser. The interference between ω_{master} and $\omega_{Downshifted}$ generates a beat note whose value could be given as

$$\omega_{EnhancedResonance} \quad = \quad \omega_{master} - \omega_{Downshifted} \tag{2.59}$$

The resonance peak observed in S_{21} curves of an optically injection-locked slave laser is in fact the beat-note between the downshifted cavity resonance frequency, $\omega_{Downshifted}$, and the master laser emission frequency ω_{master}. This beat-note is amplified due to resonance when the modulating frequency becomes equal to it. Fig. 2.5 represents the physical phenomena taking place during the optical injection-locking procedure schematically.

Equation (2.59) explains the high resonance frequencies for optically injection-locked follower lasers operating in positive frequency detuning regime. A positive frequency detuning value leads to a high resonance frequency. These high resonance frequencies, however, do not help in increasing the overall 3-dB bandwidth of the system because the resonance is

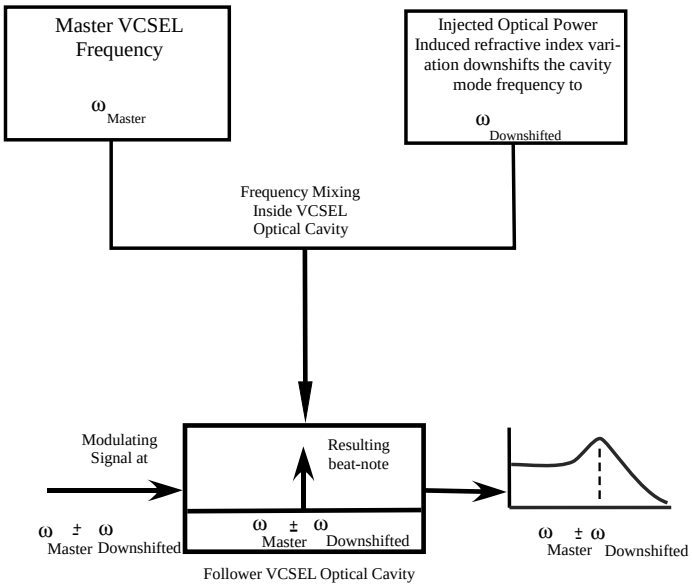

Figure 2.5: A schematic diagram representing the physical phenomenon of resonance frequency enhancement of the follower VCSEL due to optical injection-locking. The beat note $\omega_{master} - \omega_{Downshifted}$ created due to frequency-mixing inside the follower VCSEL optical cavity is amplified due to resonance when a signal with a same frequency value is applied to modulate the follower VCSEL.

pronounced so far on the frequency spectrum that the S_{21} curve has already tapered down to below 3-dB of the DC gain [11].

When the follower laser is injection-locked in the negative frequency detuning operation regime, quite logically the enhancement in the optically injection-locked follower laser frequency is not colossal. However, this resonance, by virtue of not being very high in frequency, falls within the operating limits of the lasing device and increases the overall bandwidth of the system along with the DC gain. Furthermore Murakami et al. [12] have shown that the carrier population density induced variation in the cavity resonance can be mathematically described as follows:

$$\omega_{Shifted} = \frac{\alpha_H}{2} \cdot a_0 \cdot \Delta N \tag{2.60}$$

where a_0 represents the differential gain and ΔN is the variation in the carrier population density.

Equation 2.60 shows that the value of $\omega_{Shifted}$ depends on ΔN . Since this variation is affected by injecting optical power from the master laser inside the follower laser cavity, varying the injected power varies the cavity resonance frequency of the optically injection-locked laser. An increase in photon population inside the follower laser cavity through optical injection downshifts the cavity resonance frequency and (equations (2.59) and (2.60)) increases the $\omega_{EnhancedResonance}$. The $\omega_{EnhancedResonance}$ therefore is directly proportional to the injected optical power. Numerous research groups have already presented S_{21} curves of

optically injection-locked follower lasers to demonstrate this effect [6, 13, 14].

2.4 Numerical Simulations

2.4.1 VCSEL Intrinsic Parameters

Parameter	Units	Value
η_i	-	0.8
τ_e	ns	0.61
N_{th}	cm^{-3}	5.33x10^{18}
N_{tr}	cm^{-3}	3.24x10^{18}
A	s^{-1}	1.1x10^{8}
B	cm^3/s	1x10^{-10}
C	cm^6/s	3.57x10^{-29}
a_0	cm^2	4.8x10^{-16}
v_g	cm/s	7.7x10^{9}
ϵ	cm^3	2.2x10^{-17}
τ_P	ps	6.4
S	cm^{-3}	2.5x10^{15}

Table 2.1: Long wavelength VCSEL intrinsic parameters used to simulate the small-signal injection-locking behavior[15].

The mathematical model proposed above is implemented in MATLAB in order to observe the small-signal response of an injection-locked system. Table. 2.1 summarizes the VCSEL intrinsic parameters used to calculate the S_{21} response of an injection locked system [15].

2.4.2 Simulation Results

Recently the most significant application of optical injection-locking has been in the domain of resonance frequency enhancement. The enhanced resonance frequency can lead to an extended bandwidth many times the original device bandwidth. The modulation response of an injection-locked laser can be characterized as one of the following three:

- High Resonance Frequency, Low Bandwidth
- High Resonance Frequency, High Bandwidth
- Low Resonance Frequency, Low Bandwidth

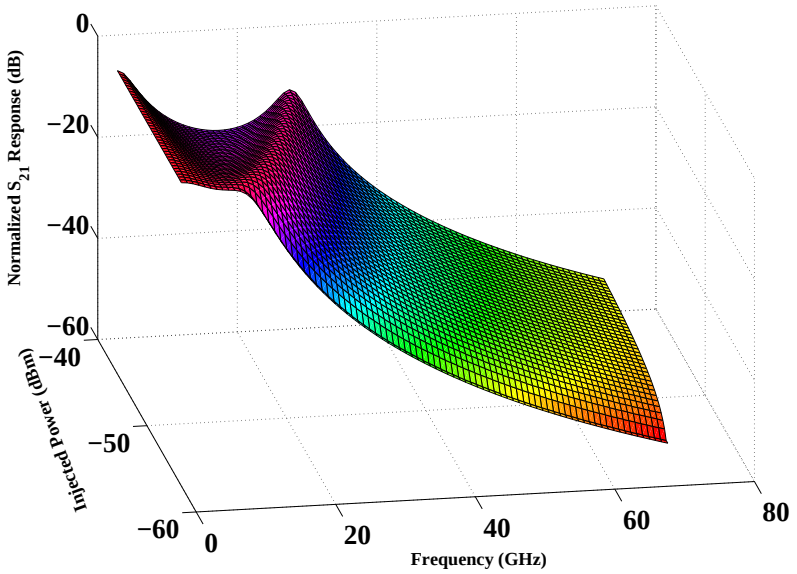

Figure 2.6: Calculated S_{21} response of an optically injection-locked VCSEL with constant frequency detuning and variable injection power from -60 dBm to -40 dBm.

Although, as presented in Fig. 2.6, the resonance frequency of an optically injection-locked laser increases with increasing injected power levels, the frequency detuning between the two lasers plays a very important role in determining the eventual characteristics of the S_{21} curve and finally the effective bandwidth. The above presented three different kinds of modulation responses depend on different locking conditions and parameters and are described in the following section.

2.4.2.1 High Resonance Frequency, Low Bandwidth

The high resonance frequency, low bandwidth operation regime can be attributed to a positive frequency detuning. Since the resonance frequency of an injection-locked system is the difference between the master laser frequency and the down shifted follower cavity frequency (equation (2.59)), positive frequency detuning results in very high resonance frequencies. On the other hand, optically injection-locked systems can be mathematically defined as third-order systems and suffer from low-frequency dips due to the presence of a parasitic pole.

Figures. 2.7 and 2.8 present the simulated S_{21} response of an optically injection-locked VCSEL operating in the positive frequency detuning regime. The injected optical power is maintained constant for this set of curves in order to study the effects of variation in positive frequency detuning. The resonance frequency increases with increasing difference between the master and follower VCSEL frequencies.

Although from a telecommunication point of view, enhancement in resonance frequency

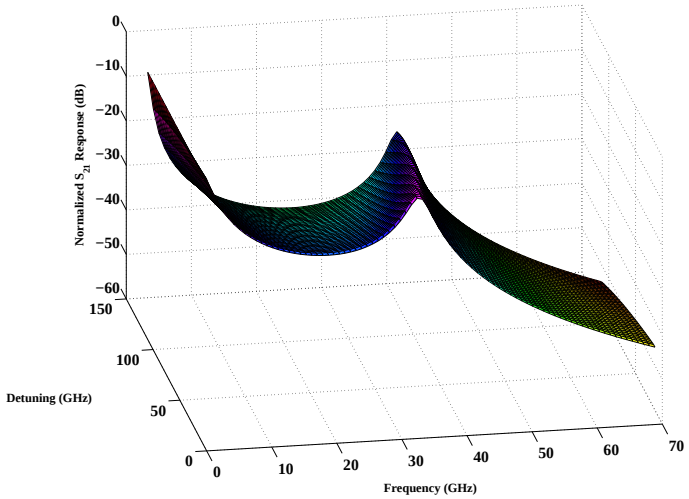

Figure 2.7: Calculated S_{21} response of an optically injection-locked VCSEL with constant injected power and variable positive frequency detuning. The detuning is varied from 10 GHz to 110 GHz.

is desired but the low frequency dip of an optically injection-locked system operating in the positive frequency detuning regime limits the effective bandwidth of the system and renders the system inefficient. This configuration therefore is not desired for operation in datacom and telecommunication environments.

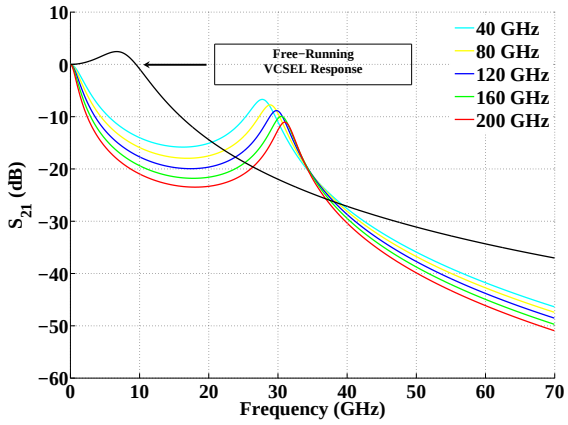

Figure 2.8: Simulated S_{21} response of an optically injection-locked VCSEL. The injected optical power is kept constantwhile the resonance frequency increases with increasing detuning frequencies.

Very high resonance frequencies however can be beneficial for another very important application i.e. the generation of millimeter-wave signals. Since the proposal of the $\backsim$ 60GHz band for the radio link frequency in broad-band cellular systems, the utilization of optical fiber for signal distribution has attracted much interest. This is due to low-loss nature of the optical fibers that are capable of transmitting data at very high bit rates. The

main obstacle in the implementation of this scheme is the conception of a high frequency oscillator. Goldberg et. al had already demonstrated the generation of microwave signals using injection-locked laser diodes in 1983 [16], but the enthusiasm in the implementation of this scheme faded away due to the incipient nature of semiconductor lasers at that time. Noel et al. presented an optical millimeter-wave generation technique in 1996 by locking an FP laser in the positive detuning frequency operation regime [17]. In 1998 Braun et al. demonstrated the generation of a low phase-noise millimeter-wave generation at 64GHz by injection-locking the optical sideband of a laser [18]. Since then several research groups have used optical injection-locking for millimeter-wave generation [9], [19], [20].

2.4.2.2 High Resonance Frequency, High Bandwidth

Positive frequency detuning can be employed to achieve very high resonance frequencies that could be useful for certain applications such as microwave and millimeter-wave signal generation but such high resonance frequencies imply very low cut-off frequencies due to low-frequency dip associated to positive frequency detuning. This situation can be improved by operating the laser at close to zero detuning.

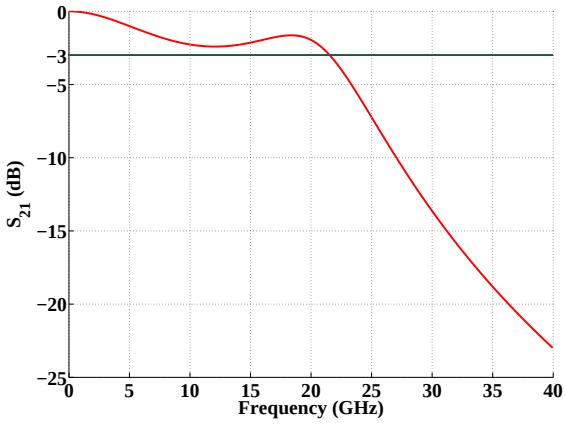

Figure 2.9: Simulated S_{21} response of an optically injection-locked follower VCSEL showing cut-off frequency enhancement.

In such a configuration, the cut-off frequency increases with increase in injected power but due to very low frequency detuning value there is no loss at low frequency values. Frequency detuning has little or no effect on the resonance frequency of such a system and the bandwidth increase is dependent only on optical injected power. This configuration can be employed for broadband digital communications that require the transmission of very high bit rates.

2.4.2.3 Low Resonance Frequency, Low Bandwidth

The third operation regime is defined by negative frequency detuning. Fig. 2.10 presents a set of simulated S_{21} curves with increasing negative frequency detuning. It is clear from Fig. 2.10 that for positive frequency detuning values, the follower VCSEL S_{21} response is undamped with high resonance frequencies. However when the detuning between the two VCSELs is varied in the negative detuning operation regime, the S_{21} response curves start to become highly damped. At the same time, the low frequency dip, exhibited due to positive frequency detuning operation regime starts to disappear. Finally at relatively high values of negative frequency detuning the S_{21} curves become over-damped and gradually the resonance peak vanishes.

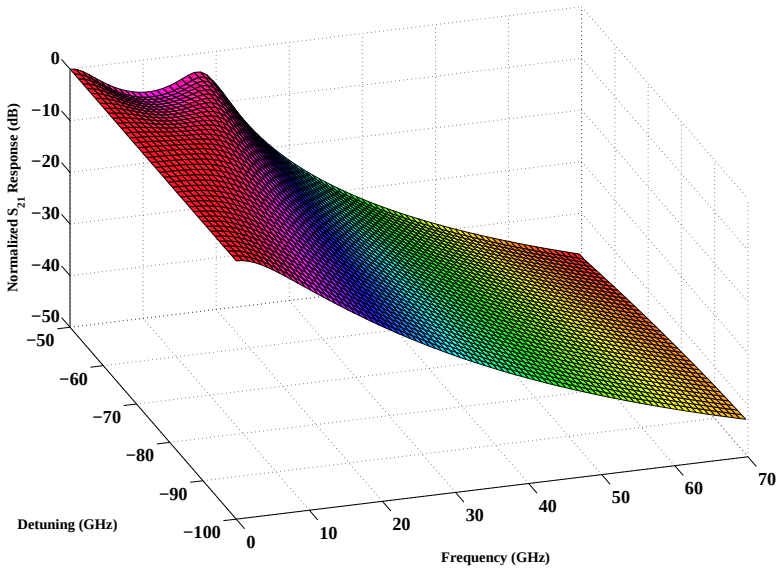

Figure 2.10: Calculated S_{21} response of an optically injection-locked VCSEL with constant injected power and variable negative detuning. The detuning is varied from 10 GHz to -190 GHz.

The negative frequency detuning can hence be used to generate high low frequency gain S_{21} curves. This is particularly important for directly modulated optical fiber links. The losses in such links, apart from coupling and connector losses, are due to Electrical-Optical (E/O) and Optical-Electrical (O/E) conversion. Sung et al. have demonstrated that by injection-locking a laser in negative frequency detuning regime the RF link gain can be improved by up to 10 dB [21].

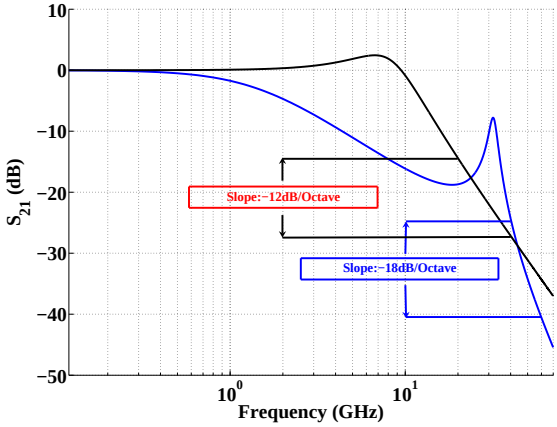

Figure 2.11: Comparison between the free-running and injection-locked transfer functions of a VCSEL.

2.5 Comparison between Free-Running and Injection-Locked VCSEL Models

Fig. 2.11 presents a comparison between the free-running and injection-locked S_{21} response of a VCSEL. The frequency responses are plotted on a logarithmic scale in order to highlight the difference between the respective slopes of the two systems. The injection-locked system has a slope of -18dB/octave as compared to a slope of -12dB/octave for a free-running VCSEL. Another important difference of note is the low frequency dip in the optically injection-locked VCSEL S_{21} response which is due to the extra pole in the transfer function denominator (ref. equation 2.56).

By putting S_{inj} and $\Delta\omega$ equal to zero the modified VCSEL rate equations (equations 2.5, 2.6, 2.7) are reduced to classical VCSEL rate equations (equations 2.1, 2.2, 2.4). Figure.2.12 presents a comparison between the S_{21} responses of a free-running and an injection-locked VCSEL using the same set of modified rate equations.

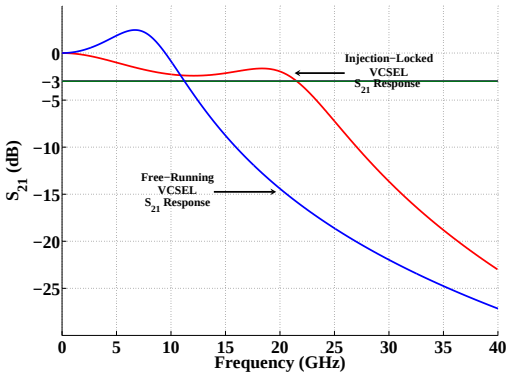

Figure 2.12: Free-Running VCSEL S_{21} response calculated by putting S_{inj} and $\Delta\omega$ equal to zero in equations 2.5, 2.6 and 2.7.

2.6 Conclusion and Discussion

The simulations, under different operating conditions, of optically injection-locked VCSELs presented in this chapter reveal certain interesting patterns. First of all, it must be noted that due to the very highly selective nature of the DBR mirrors used in the VCSEL manufacturing, a very small amount of light enters in the cavity. This is clear from the locking-range calculations presented in Figures. 2.2 and 2.3. It is therefore not the injected optical power intensity that is mainly responsible for injection-locked VCSELs' S_{21} curves variations. It is in fact the coupling factor k_c whose numerical value is responsible for high locking ranges, facility of injection-locking and high resonance frequencies.

Another important point is the S_{21} curve shape dependence on the frequency detuning value between the two VCSELs. The frequency detuning is the dominant factor in determining the shape of the S_{21} curve and whether it would be high resonance frequency under-damped response or a low resonance frequency high bandwidth flat response. This phenomenon can be explained by understanding the beat-frequency generation effect produced inside the follower VCSEL optical cavity (sub-section 2.3.1).

Finally, due to optical coupling with the master laser, the dynamic response characteristics of the follower VCSEL change. Usually a two-equation mathematical model is utilized in VCSEL dynamic response simulations. This model gives way to a three-equation system which incorporates the effect of external light injection. Due to this third equation, the presence of a 3^{rd} pole is observed in the transfer function of the optically injection-locked VCSEL (equation 2.56). At positive detuning frequency values, this pole becomes dominant at low frequencies and causes the S_{21} response to suffer dips of several dBs which in turn severely limits the effective bandwidth of the system.

Bibliography

[1] R. Lang, "Injection Locking Properties of a Semiconductor Laser," *IEEE Journal of Quantum Electronics*, vol. 18, no. 6, pp. 976–983, Jun 1982.

[2] P. Gallion and G. Debarge, "Influence of amplitude-phase coupling on the injection locking bandwidth of a semiconductor laser," *Electronics Letters*, vol. 21, no. 7, pp. 264–266, 28 1985.

[3] P. Gallion, H. Nakajima, G. Debarge, and C. Chabran, "Contribution of spontaneous emission to the linewidth of an injection-locked semiconductor laser," *Electronics Letters*, vol. 21, no. 14, pp. 626–628, 4 1985.

[4] C. Henry, N. Olsson, and N. Dutta, "Locking Range and Stability of Injection Locked 1.54μm InGaAsp Semiconductor Lasers," *IEEE Journal of Quantum Electronics*, vol. 21, no. 8, pp. 1152–1156, Aug 1985.

[5] I. Petitbon, P. Gallion, G. Debarge, and C. Chabran, "Locking bandwidth and relaxation oscillations of an injection-locked semiconductor laser," *IEEE Journal of Quantum Electronics*, vol. 24, no. 2, pp. 148–154, Feb 1988.

[6] L. Chrostowski, X. Zhao, and C. Chang-Hasnain, "Microwave Performance of Optically Injection-locked VCSELs," *IEEE Transactions on Microwave Theory and Techniques*, vol. 54, no. 2, pp. 788–796, Feb. 2006.

[7] T. Simpson, J. Liu, and A. Gavrielides, "Small-signal analysis of modulation characteristics in a semiconductor laser subject to strong optical injection," *IEEE Journal of Quantum Electronics*, vol. 32, no. 8, pp. 1456–1468, Aug 1996.

[8] X. Meng, T. Chau, D. Tong, and M. Wu, "Suppression of Second Harmonic Distortion in Directly Modulated Distributed Feedback Lasers by External Light Injection," *Electronics Letters*, vol. 34, no. 21, pp. 2040–2041, Oct 1998.

[9] H. Kee-Sung, T. Jung, M. Wu, D. Tishinin, K. Liou, and W. Tsang, "Optical generation of millimeter-waves using monolithic sideband injection locking of a two-section DFB laser," *The 16th Annual Meeting of the IEEE Lasers and Electro-Optics Society. LEOS 2003.*, vol. 2, pp. 1005–1006 vol.2, Oct. 2003.

[10] L. Barry, P. Anandarajah, and A. Kaszubowska, "Optical pulse generation at frequencies up to 20 GHz using external-injection seeding of a gain-switched commercial Fabry-Perot laser," *IEEE Photonics Technology Letters*, vol. 13, no. 9, pp. 1014–1016, Sep 2001.

[11] L. Chrostowski, F. B., W. Hoffman, M.-C. Amann, S. Wieczorek, and W. Chow, "40 GHz Bandwidth and 64 GHz Resonance Frequency in Injection-Locked 1.55 μm VCSELs," *IEEE Journal of Journal of Selected Topics in Quantum Electronics*, vol. Vol. 13, No. 5, 2007.

[12] A. Murakami, K. Kawashima, and K. Atsuki, "Cavity Resonance Shift and Bandwidth Enhancement in Semiconductor Lasers With Strong Light Injection," *IEEE Journal of Quantum Electronics*, vol. 39, no. 10, pp. 1196–1204, Oct. 2003.

[13] X. Zhao, E. K. Lau, D. Parekh, H.-K. Sung, W. Hofmann, M. C. Amann, M. C. Wu, and C. J. Chang-Hasnain, "107-GHz Resonance Frequency of 1.55μm VCSELs Under Ultra-high Optical Injection Locking," in *OSA/CLEO*, 2008.

[14] X. Zhao, M. Moewe, L. Chrostowski, C.-H. Chang, R. Shau, M. Ortsiefer, M.-C. Amann, and C. Chang-Hasnain, "28 GHz Optical Injection-Locked 1.55μm VCSELs," *IEE Electronic Letters*, vol. Vol. 40 No. 8, 15 April 2004.

[15] A. Bacou, "Caractérisation et Modélisation optoélectronique de VCSEL à grande longueur d'onde pour sous-ensembles optiques intégrés," Ph.D. dissertation, Institut Supérieur de l'Aéronautique et de l'Espace, 2008.

[16] L. Goldberg, H. Taylor, J. Weller, and D. Bloom, "Microwave signal generation with injection-locked laser diodes," *Electronics Letters*, vol. 19, no. 13, pp. 491–493, 23 1983.

[17] L. Noel, D. Marcenac, and D. Wake, "Optical millimetre-wave generation technique with high efficiency, purity and stability," *Electronics Letters*, vol. 32, no. 21, pp. 1997–1998, Oct 1996.

[18] R.-P. Braun, G. Grosskopf, D. Rohde, and F. Schmidt, "Low-phase-noise millimeter-wave generation at 64 GHz and data transmission using optical sideband injection locking," *Photonics Technology Letters, IEEE*, vol. 10, no. 5, pp. 728–730, May 1998.

[19] Z. Ahmed, H. Liu, D. Novak, Y. Ogawa, M. Pelusi, and D. Kim, "Locking characteristics of a passively mode-locked monolithic DBR laser stabilized by optical injection," *IEEE Photonics Technology Letters*, vol. 8, no. 1, pp. 37–39, Jan. 1996.

[20] J. Hong and R. Hui, "Tunable millimeter-wave generation with subharmonic injection locking in two-section strongly gain-coupled DFB lasers," *IEEE Photonics Technology Letters*, vol. 12, no. 5, pp. 543–545, May 2000.

[21] H.-K. Sung, T. Jung, D. Tishinin, K. Liou, W. Tsang, and M. Wu, "Optical Injection-Locked Gain-Lever Distributed Bragg Reflector Lasers With Enhanced RF Performance," *IEEE International Topical Meeting on Microwave Photonics. MWP'2004.*, pp. 225–228, Oct. 2004.

Chapter 3 Optical Injection-Locking Experiments

The injection-locking experiments carried-out during the course of this work evolved progressively in their complexity. The objective was to demonstrate and understand the VCSEL-by-VCSEL optical injection-locking phenomena under different operating constraints. Our focus was the study of variations in S_{21} response of injection-locked VCSELs under different injection powers and varying detuning frequencies.

3.1 Experiments using Multimode Lasers

3.1.1 Multimode Edge Emitting Lasers (EELs)

Optically injection-locked lasers are known to overcome many fundamental limitations of free-running systems. One of the very important improvements proposed by the employment of the optical injection-locking technique is the side-mode suppression of a multimode laser [1]. figure 3.1 presents the super-imposed optical spectra of a free-running and an injection-locked laser diode. The Fabry-Pérot modes, visible in the free-running regime, undergo approximately 35 dB suppression when injection-locked using a DFB laser diode.

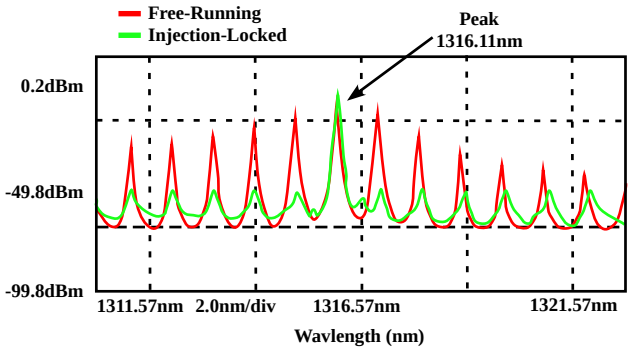

Figure 3.1: The super-imposed spectra of a free running and an injection locked Fabry-Pérot EEL. Mode suppression can be observed in the injection locked spectrum.

In the stable locking regime (figure 3.2) the follower laser frequency is locked to the master laser lasing frequency. The injection-locked Fabry-Pérot mode therefore becomes dominant and the unlocked modes are suppressed. Iwashita et. al demonstrated the utilization of this method for the suppression of mode-partition noise [1]. The employment of optical-injection locking for side-mode suppression in VCSELs however is not very effective.

This is due to the difference in the side-mode generation mechanism between the EELs and the VCSELs. A detailed analysis of side-mode generation is presented in the following section.

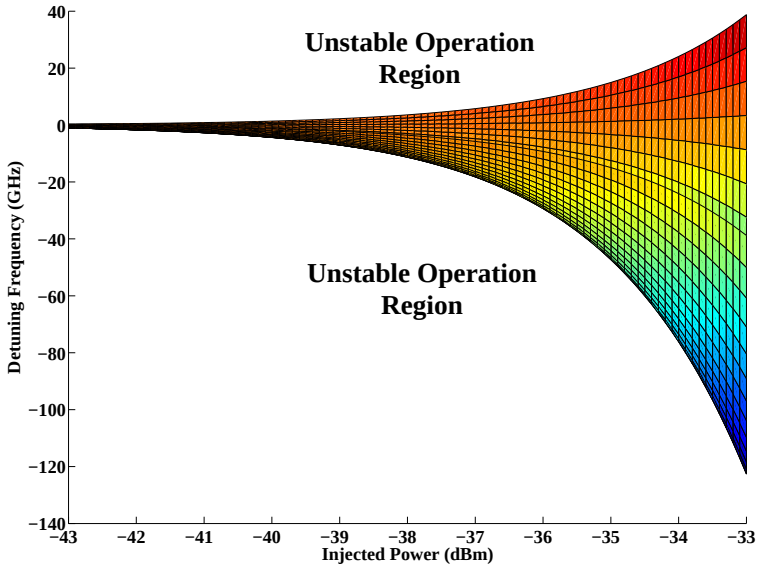

Figure 3.2: 2D presentation of calculated locking range of a long wavelength VCSEL with $\alpha_H = 3$ showing the locking-range dependence on injected optical power.

Single-mode operation of the follower laser however is highly desirable due to another very important reason. As presented in figure 3.2, the locking-range of an injection-locked laser, in the "stable operation region", is dependent on the injected optical power. This effective locking-range is exploitable only if the follower laser is single-mode. If the follower laser is multimode, the achievable detuning frequency is limited by the Free Spectral Range (FSR) of the follower laser. At large detuning frequencies, the master laser might come closer to an adjacent longitudinal mode and in that case, it will lock the adjacent longitudinal mode instead of sweeping the entire locking range with previously locked mode. This mode-hopping reduces the effective "locking" and hence "operation range" of an injection-locked system.

3.1.2 Multimode VCSELs

Figure 3.3 presents the optical spectrum of a multimode VCSEL. The VCSEL in question is manufactured by Vertials with a threshold current of 6 mA and peak output optical power of 20 mW. The VCSEL chip was powered-up using a probe-station. The master laser is single-mode Vertilas VCSEL emitting in the 1.55μm range. A comparison with figure 3.4 shows that optical injection-locking fails to produce an effect similar to that demonstrated previously on multimode EELs. Although a nominal side-mode suppression is observed in the injection-locked follower VCSEL spectrum, the emission spectrum rests multimode.

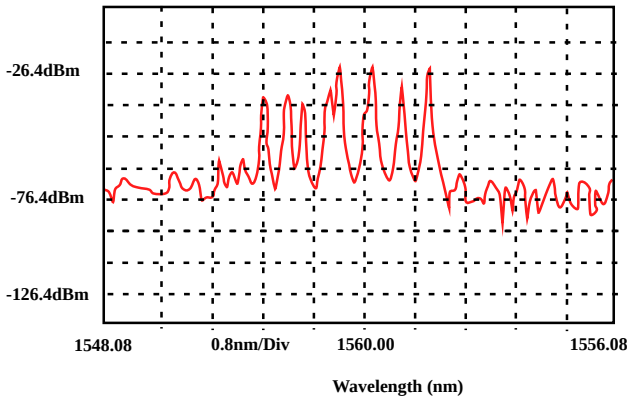

Figure 3.3: Optical spectrum of an Vertilas multimode "Power" VCSEL. The VCSEL threshold current is about 6 mA.

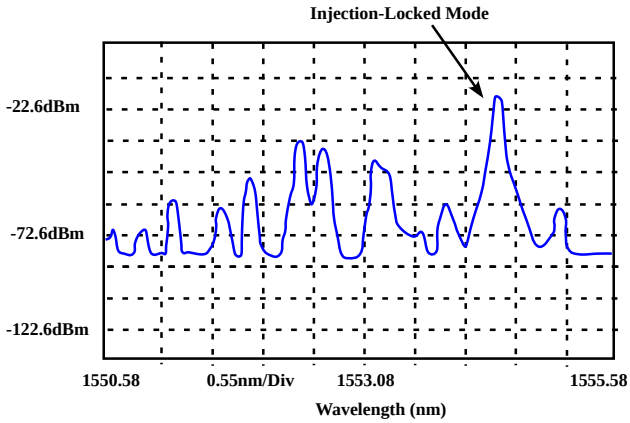

Figure 3.4: Spectrum of an optically injection-locked multimode Vertilas VCSEL. The threshold current is about 6 mA. A very feeble side-mode suppression is observed due to injection-locking.

This can be explained by developing an understanding of the side-mode generation phenomena in VCSELs. The active region of a VCSEL is very short as compared to that of an EEL, essentially of the order of the emission wavelength. Consequently, only one Fabry-Pérot mode exists in the VCSELs, since the physical dimensions of the cavity eliminate the possibility of longitudinal multi-mode lasing action. Therefore VCSELs are fundamentally single-mode emission devices. However, the confinement and guiding of the optical field thus generated is made very difficult due to a very peculiar VCSEL structural characteristic. VCSEL design suggests the sharing of a common path for photons and carriers, moving through the DBRs. This leads to the heating of the DBRs due to carrier flow and results in a variable refractive index distribution inside the VCSEL optical cavity. The creation of non-uniform refractive index zones inside the optical cavity leads to different optical paths and has an overall dispersive effect. This phenomenon is known as "Thermal Lensing".

The electrons passing through the DBRs tend to concentrate on the edge of the active zone due to the oxide aperture-based carrier guiding. A higher carrier concentration at the fringes of the active zone translates into higher photon generation at the edges of the active zone. Instead of being concentrated in the center of the optical cavity, in the form of a single transverse mode, the optical energy is repartitioned azimuthally inside the optical cavity. The creation of non-uniform refractive index zones within the VCSEL optical cavity, changes the effective optical path inside the cavity which manifests itself in the form of undesired side-modes. Since the VCSEL side-modes are a consequence of spatial energy distribution, they are referred to as "Spatial" or "Transverse Modes".

Higher bias currents therefore imply high optical power and in consequence a higher number of transverse modes. An oxide-aperture is employed in order to achieve optimal current confinement and to block unwanted transverse modes. The oxide-aperture diameter determines the multimode or single mode character of a VCSEL. VCSELs having oxide aperture diameters greater than 5μm exhibit a multimode behavior. It can also be inferred from the above discussion that for the type of VCSELs employing the oxide-aperture technology for optical confinement, single mode VCSELs almost always have emission powers less than those of multimode VCSELs. Since the Vertilas VCSEL used here is a high power device, it has a Buried Tunnel Junction (BTJ) diameter of 20μm and is therefore distinctly multimode. Since optical injection-locking favors single-mode operation by eliminating longitudinal modes and since the modes generated in VCSELs are not longitudinal, the employment of optical injection-locking for single-mode VCSEL operation is not very effective.

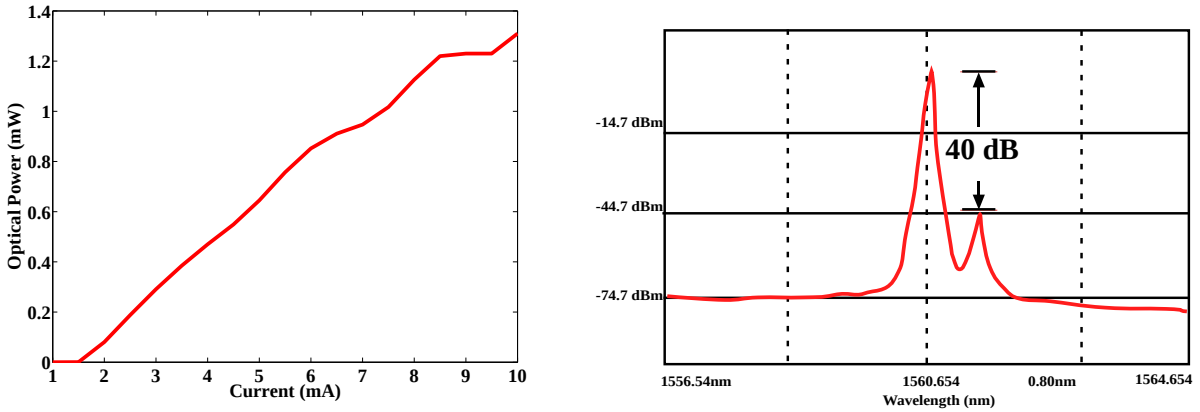

(a) L-I curve

(b) Optical spectrum

Figure 3.5: L-I curve (a) and Optical spectrum (b) of a Vertilas VCSEL with an emission wavelength of 1.55μm.

3.2 Experiments using Single-Mode VCSELs

3.2.1 Experiments Using Vertilas VCSELs

A logical step, after trying optical injection-locking of multimode VCSELs, was to attempt the injection-locking of single-mode VCSELs. The VCSELs used for initial injection-locking experiments were manufactured by Vertilas GmbH. These are single-mode, TO-46 packaged, pigtailed, Buried Tunnel Junction (BTJ) devices with an emission wavelength of 1.55μm. The L-I curve of the follower VCSEL is presented in figure 3.5 (a). The mode suppression ratio between the fundamental and the side-mode is approximately 40 dBs.

Figures. 3.6 and 3.7 present the measurement test bench and the master and follower laser spectra respectively.

The injection-locking experiments using Vertilas VCSELs were simple to carry-out due to the pigtailed nature of the components, that made the optical power-injection inside the follower VCSEL cavity relatively easy. The well known phenomenon of side-mode suppression (as demonstrated with EELs and presented in figure 3.4) was observed. When the VCSEL satellite mode is optically injection-locked, the fundamental mode undergoes a rapid diminution and the VCSEL output optical power shifts to the side-mode wavelength. However, other than being a *proof of concept* demonstration, this exercise proved to be of little significance. The real price of this ease of manipulation was paid in terms of a degraded frequency response. The TO-46 package cut-off frequency was about 5 Ghz which was well below the component cut-off frequency (11 GHz). The observation of injection-locked VCSELs' S_{21} response under various injection conditions was therefore not possible.

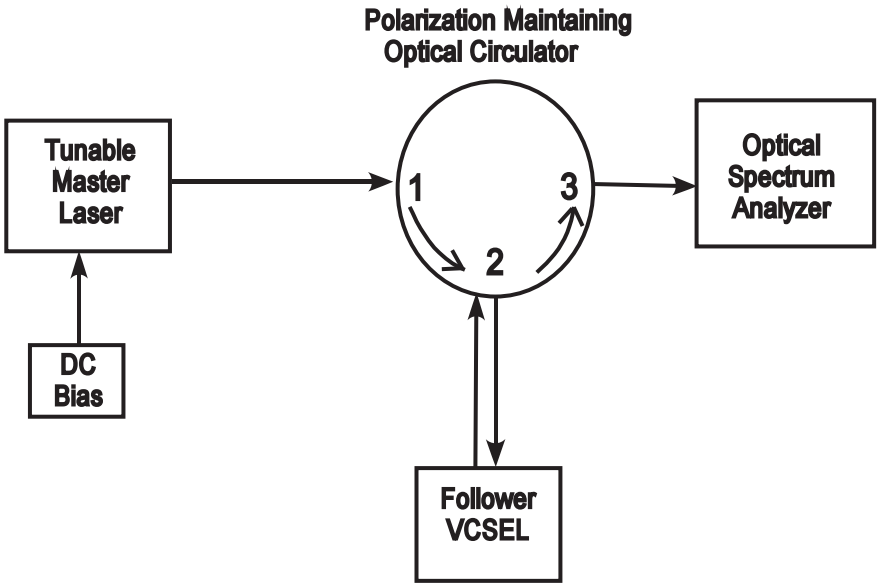

Figure 3.6: Test-bench used for Vertilas 1.55μm VCSEL optical injection-locking measurements.

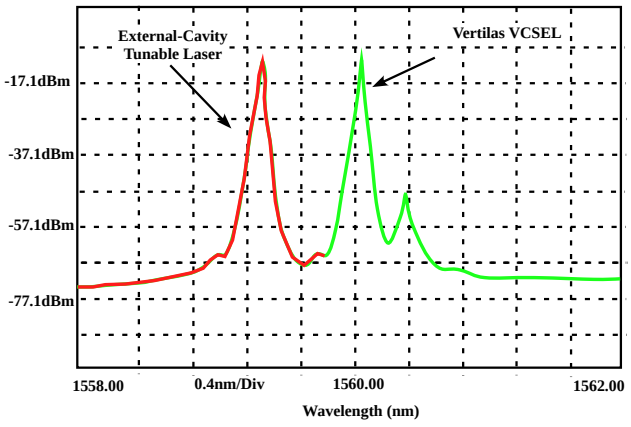

Figure 3.7: Simultaneous presentation of the master and follower laser optical spectra. The master laser is a tunable external cavity laser while the follower laser is a Vertilas single mode 1.56μm VCSEL.

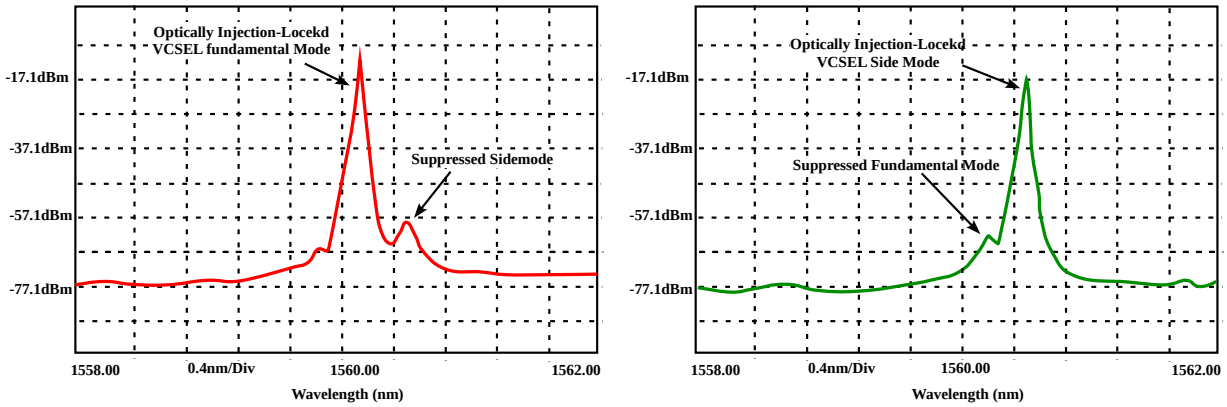

(a) (b)

Figure 3.8: (a) Optical spectrum of an optically injection-locked Vertilas VCSEL. The locking of fundamental mode further suppresses the side-mode. (b) Optical spectrum of an optically injection-locked Vertilas VCSEL. The locking of side mode has suppressed the fundamental lasing mode. Notice the position of the suppressed modes in the two different cases.

3.2.2 Experiments Using BeamExpress VCSELs

In 2007, in the context of a trans-national project [1], VCSEL injection-locking studies were undertaken using BeamExpress VCSELs. Markedly different technologically and functionally from Vertilas VCSELs, BeamExpress VCSELs opened-up very interesting and unique research possibilities. Their on-chip availability, along with a comprehensive information about their structure and their fabrication technique, presented following unparalleled advantages:

- The on-chip configuration eliminated the problems associated to parasitics introduced by packaging. This also suggested the possibility of observation of device intrinsic S_{21} response.

- The fabrication process and device structure knowledge allowed the extraction of intrinsic parameters, that in turn led to reliable injection-locking simulations [2].

- Disposal of VCSELs from the same wafer allowed to observe the identical VCSEL-by-VCSEL optical injection-locking for various applications.

Although the on-chip VCSEL-by-VCSEL optical injection-locking, as discussed above, presented many interesting possibilities, its physical implementation proved to be quite challenging. The biggest problem encountered was optical power coupling from the VCSEL

[1] The MNT Eranet Project focusing on the development of VCSEL modules for Coarse Wavelength Division Multiplexing (CWDM) and for optical networks.

[2] For a comprehensive discussion on VCSEL optical cavity intrinsic response, parasitics associated with on-chip VCSEL performance and VCSEL-chip intrinsic parameter extraction refer to [2].

emission window into the optical fiber for utilization in the fairly classical set-up proposed in figure 3.9.

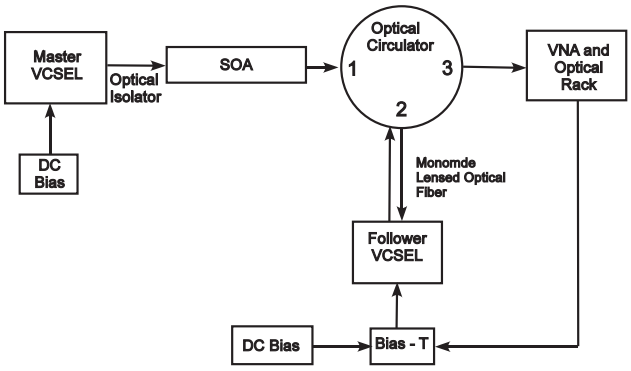

Figure 3.9: Optical injection-locking setup using a polarization maintaining optical circulator. A semiconductor optical amplifier (SOA) connected to port 1 is used to vary the injected optical power.

The VCSELs S_{21} response was observed using an HP-8510C Vector Network Analyzer (VNA) operating up to 20 GHz. An optical rack is integrated to the VNA which consists of a calibrated photodiode for Optical-Electrical conversion. The VCSEL optical output was directly provided to this calibrated photodiode. A schematic representation of the experimental set-up used to measure the S_{21} response of an on-chip VCSEL using a VNA is given in figure 3.10.

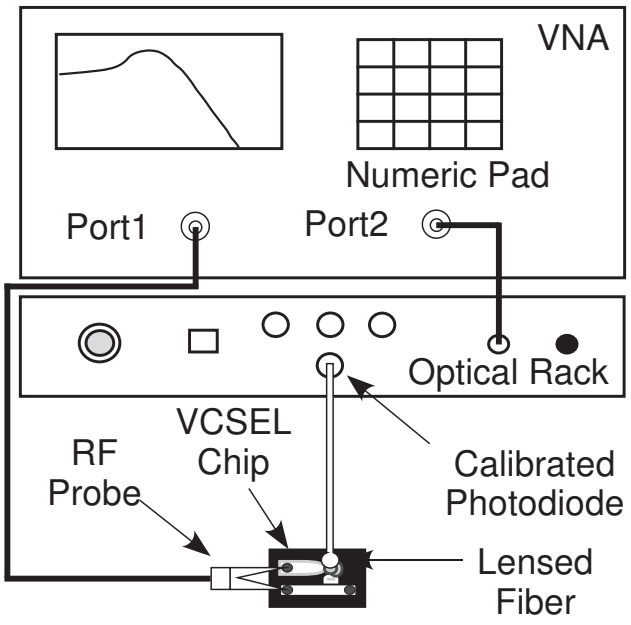

Figure 3.10: Schematic representation of the experimental setup used to measure the S_{21} response of an on-chip VCSEL using a vector network analyzer.

The L-I curves for the set of VCSELs used in this experiment are presented in figures 3.11 and 3.12. Since no temperature control was applied to the VCSELs during the course of this work, the VCSEL wavelength variation ($\delta\lambda$) was achieved by changing the bias current. Representative λ-I tuning curves are also given in figures 3.11 and 3.12. In order to vary the injected optical power, without altering the master VCSEL emission wavelength and hence the detuning frequency value, an Optical Semiconductor Amplifier (OSA) has been utilized. The maximum optical output power collected using a lensed multimode fiber is approximately 2 mW. Although 2 mW appears to be sufficient to carry-out injection-locking experiments, it must be noted that in this instance, the optical power is collected using a multimode fiber. The utilization of the polarization maintaining optical circulator requires the employment of a single-mode fiber which restricts the maximum available optical power to about 0.4 mW.

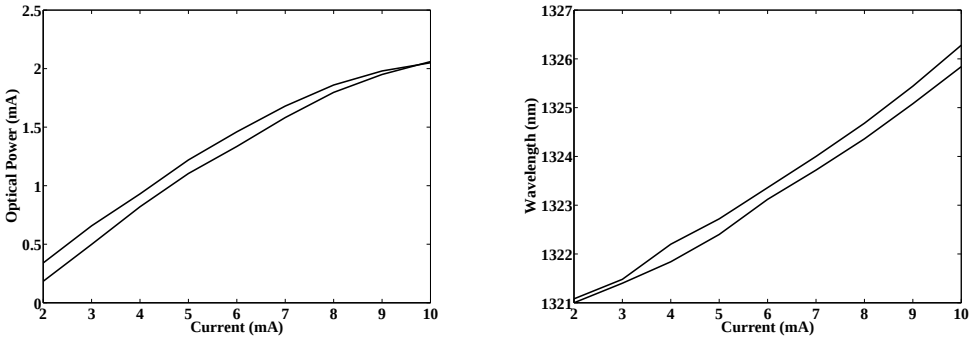

(a) Optical Power vs. Bias Current (b) Wavelength Tuning

Figure 3.11: The L-I curves for the first set of BeamExpress VCSELs used in this experiment. Representative wavelength-bias current tuning curves are also given.

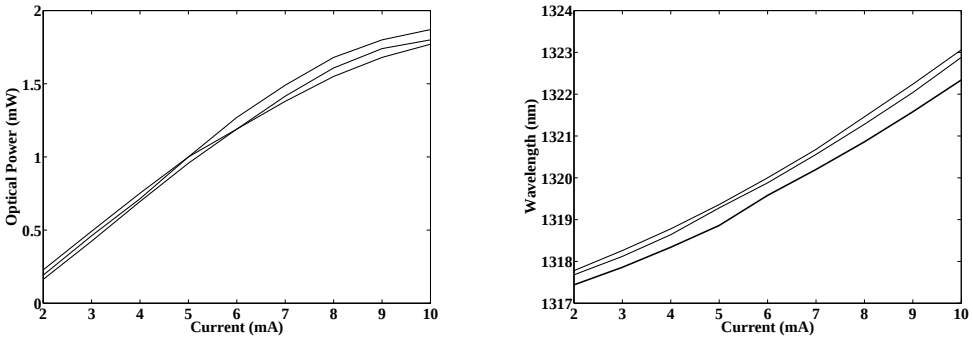

(a) Optical Power vs. Bias Current (b) Wavelength Tuning

Figure 3.12: The L-I curves for the second set of BeamExpress VCSELs used in this experiment. Representative wavelength-bias current tuning curves are also given.

3.2.2.1 Optical Injection-Locking Measurement Results

We have defined three distinct operation regimes of an optically injection-locked VCSEL system in the section 2.4.2 using the injection-locked VCSEL mathematical model. Naturally, an experimental observation of these operation regimes is desired. The experimental results are therefore presented under the following rubrics:

- High Resonance Frequency, High Bandwidth
- Low Resonance Frequency, Low Bandwidth
- High Resonance Frequency, Low Bandwidth

3.2.2.2 High Resonance Frequency, High Bandwidth

A high resonance frequency with a high bandwidth can be obtained, if the frequency detuning between the two lasers is kept negative (i.e. $\omega_{Master} < \omega Follower$). The detuning conditions thus employed lead to a flat frequency response, with a damped resonance frequency. Due to zero detuning, the optically injection-locked VCSEL S_{21} response does not suffer the low frequency dips. figure 3.13 presents the S_{21} response of an optically injection-locked BeamExpress VCSEL operating in the 1.3μm wavelength region. The master and follower VCSEL bias currents are 7 and 5.83 mA respectively. From figure3.11 it is clear that the follower VCSEL is injection-locked in the negative frequency detuning (positive wavelength detuning) mode. Consequently the resonance frequency is not very pronounced but the cut-off frequency is almost three times that of the same VCSEL operating in free-running mode. Although the lensed fiber, used to collect optical power from the VCSEL chip, is Anti-Reflection (AR) coated, a certain degree of re-injection can be observed on the optically injection-locked follower VCSEL S_{21} curves presented here.

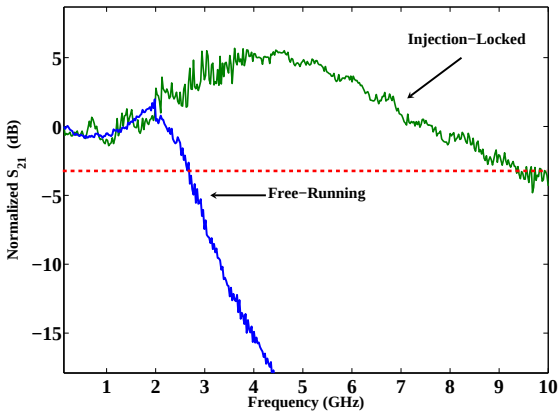

Figure 3.13: S_{21} response of an optically injection-locked single mode BeamExpress VCSEL emitting at 1.3μm.

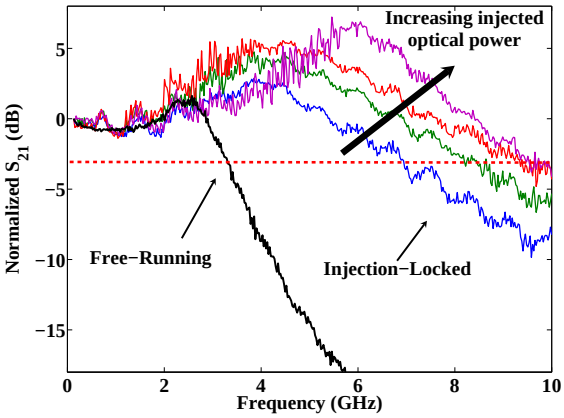

Figure 3.14: S_{21} response of an optically injection-locked single mode BeamExpress VCSEL emitting at 1.3μm. Several S_{21} curves are obtained with increasing injected optical power for a constant negative frequency detuning. $P_1 > P_2 > P_3 > P_4$

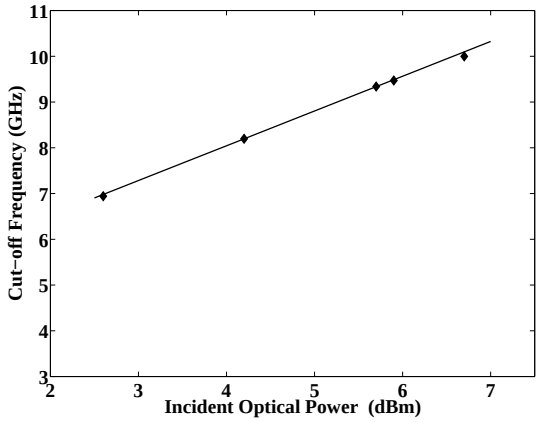

Figure 3.15: Cut-Off frequency variation of injection-locked BeamExpress VCSELs with increase in optical injected power. All the measurements were made in the negative detuning frequency operation regime.

If the injected optical power is increased under these circumstances, the resonance peak shifts toward higher frequencies thus increasing the effective bandwidth of the injection-locked system. Figure. 3.14 presents several S_{21} spectra obtained by keeping the VCSEL bias currents constant and by varying the injected optical power using the SOA. S_{21} response of a free-running VCSEL is also given for comparison. The cut-off frequency increase with respect to injected optical power is plotted in figure 3.15.

3.2.2.3 Low Resonance Frequency, Low Bandwidth

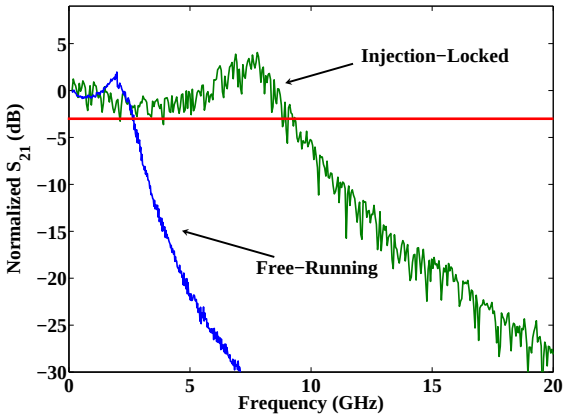

Figure 3.16: S_{21} response of an optically injection-locked single mode BeamExpress VCSEL emitting at 1.3μm. The VCSEL is injection-locked at a slightly positive detuning frequency.

If the optical injection-locking is achieved with zero or a slightly positive detuning frequency, a pronounced high resonance frequency can be obtained. Due to operation in positive frequency detuning zone of the locking-range, the injection-locked follower VCSEL S_{21} response falls off at lower frequencies. However, if the detuning is kept near zero the S_{21} response can be maintained above the 3dB limit. On the other hand, positive frequency detuning leads to a pronounced resonance frequency peak that is well above the free-running device frequency. Figure. 3.16 presents the S_{21} response of an optically injection-locked VCSEL under the above described operating conditions. The master and follower VCSEL bias currents are approximately the same (7 mA). From figure3.12 it is clear that the follower VCSEL is injection-locked in the zero or slightly positive frequency detuning (negative wavelength detuning) mode. It must be remarked that the frequency response tends to drop at low frequency but does not fall below the 3 dB line due to the detuning frequency choice.

3.2.2.4 High Resonance Frequency, Low Bandwidth

The beat note produced inside the VCSEL optical cavity is the difference between the emission frequencies of the master (ω_{Master}) and the follower ($\omega_{Follower}$) lasers respectively. When the detuning frequency between the two VCSELs is increased, the beat note thus produced

is situated farther and farther toward the higher frequencies on the spectrum. This affects the resulting S_{21} response of the injection-locked follower VCSEL in following ways:

- When the follower VCSEL is modulated with a signal having the same frequency as the beat note produced inside the cavity, a resonance is observed at this frequency on the VNA.
- The frequency response suffers a dip at lower frequencies due to the presence of an extra pole in the denominator of the injection-locked transfer function (ref. equation 2.56) [3].

Consequently, the frequency responses thus obtained have very high resonance frequencies that are in proportion with the positive frequency detuning values. However, the bandwidths of these S_{21} curves are very low as compared to those of free-running VCSELs, due to the presence of the low frequency roll-off.

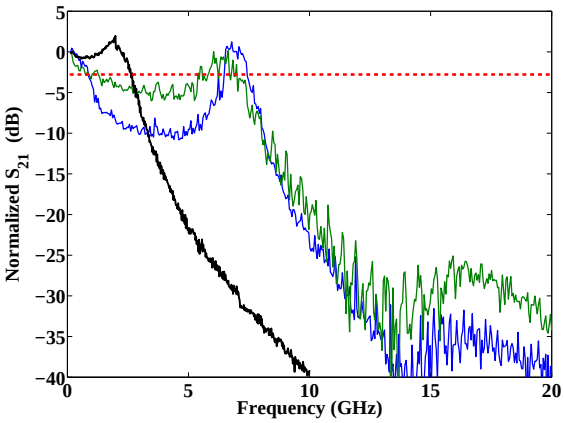

Figure 3.17: S_{21} response of an optically injection-locked single mode BeamExpress VCSEL emitting at 1.3μm and operating in the positive detuning frequency regime. The master and follower VCSEL bias currents are 6.75mA and 7.4 mA respectively.

Figure. 3.17 presents the optically injection-locked follower VCSEL S_{21} responses, obtained by working in the positive frequency detuning regime. From figure3.11 it is clear that the follower VCSEL is injection-locked in the positive frequency detuning (negative wavelength detuning) mode. Due to operation in positive frequency detuning regime, the resonance frequency value is very big (about 4 times) as compared to that of the same VCSEL operating in free-running mode. The S_{21} response experiences a dip at low frequency which reduces the cut-off frequency of the injection-locked system. These curves present the characteristic undamped resonance frequency peaks, associated with the positive detuning injection-locking regime.

It might be inferred from figure 3.2 that the resonance frequency value can be controlled by adjusting the injected optical power and the detuning frequency between the two VCSELs. Working at higher injection power levels allows for a greater degree of liberty in the choice of detuning frequency since the locking-range increases with increasing injected optical power. Figures. 3.18 and 3.19 present optical injection-locking in the positive frequency detuning regime with higher frequency detuning values made possible by increasing injected power levels. As a result, the resonance frequencies thus obtained are even higher than those presented in figure 3.17. Quite logically, the S_{21} frequency response at lower frequencies suffers higher power penalties than the S_{21} responses that were obtained with lower values of frequency detuning.

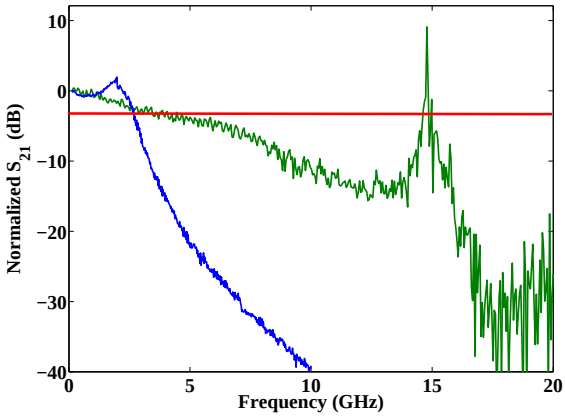

Figure 3.18: S_{21} response of an optically injection-locked single mode BeamExpress VCSEL emitting at 1.3μm and operating in the positive detuning frequency regime. The master and follower VCSEL bias currents are 6.75 and 7.84 mA respectively.

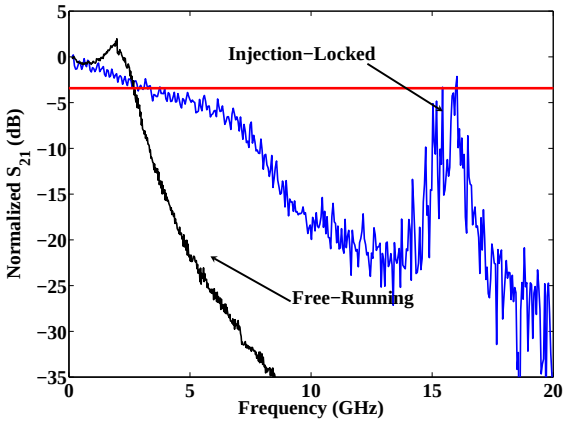

Figure 3.19: S_{21} response of an optically injection-locked single mode BeamExpress VCSEL emitting at 1.3μm and operating in the positive detuning frequency regime.

3.2.3 Experiments Using RayCan VCSELs

The optically injection-locked follower VCSEL S_{21} responses presented above, using BeamExpress VCSELs, provide very interesting results. Especially the availability of on-chip components allows the observation of parasitics-free free-running and injection-locked S_{21} responses. It was noticed however that the Master VCSEL is not modulated for these injection-locking experiments and hence needs not be on-chip. The employment of a fibered master VCSEL will facilitate the injection-locking experiments in the following ways:

- This will allow the utilization of only one probe-station instead of two thus reducing the test-bench size and minimizing its complexity.
- This will increase the magnitude of available optical power since the coupling losses on the master VCSEL side would be eliminated.

Also, injection-locking experiments in the static domain such as linewidth, polarization and RIN measurements could be carried out using fibered follower VCSEL without suffering from packaging parasitics performance penalties. BeamExpress VCSELs however were not available at that time in either fibered or TO-46 packaging. It was then decided to carry-out injection-locking experiments using commercially available RayCan VCSELs.

3.2.3.1 RayCan VCSELs Structure

The structure of a 1.3μm RayCan VCSEL is presented in figure 3.20. RayCan VCSELs are bottom-emitting type, as has been explained in 1.3.3 and in [4]. As far as the incorporation of a bottom-emitting VCSEL in an optical sub-assembly is concerned, the application of normal integration techniques such as wire-bonding or flip-chip designs are easily applicable. However, probe-station testing of bottom-emitting components poses some challenging problems. Bottom-emission implies the existence of electrodes on the reverse side of the VCSEL chip , as shown in figure 3.20. This means that in order to power-up the VCSEL, using coplanar probes, the chip has to be inverted. The chip-inversion, in turn, implies the impossibility of optical power collection with a single-mode or multimode fiber. On the other hand, if the chip is used in the top-emitting configuration, it becomes impossible to power-up the chip using probes.

Another problem was the distance between the two electrodes. The probes used for VCSEL testing have a pitch of 125 μm. However the distance between the two RayCan VCSEL electrodes is about 300 μm. Without using 300 μm pitch probes, it would have been impossible to power-up the VCSELs anyway. These two problems were solved by getting the VCSEL chip integrated to a sub-mount. The sub-mount was prepared by RayCan for VCSEL integration with a monitoring photodiode, inside a TO-46 package. As per our demand, the VCSEL chips were integrated to the sub-mounts and delivered to us unpackaged.

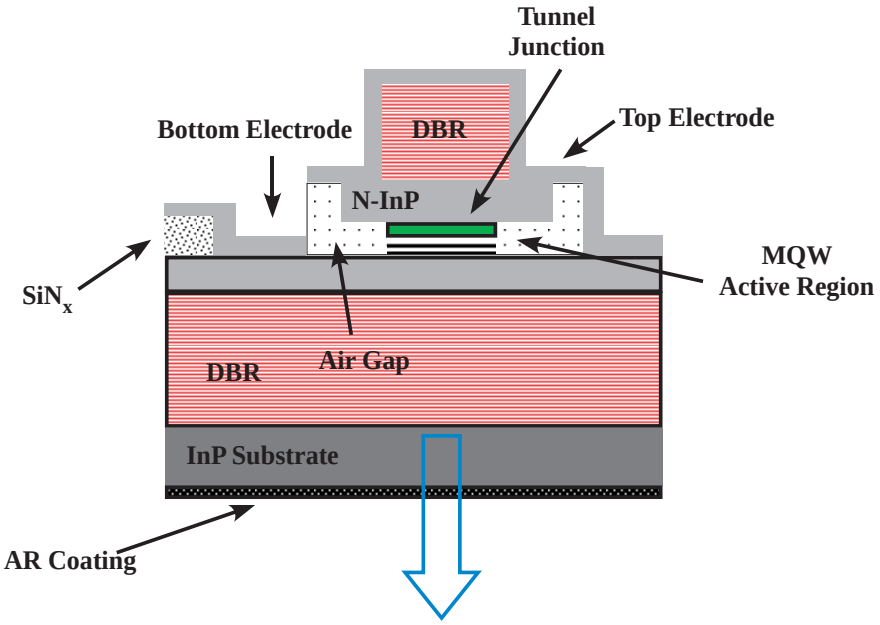

Figure 3.20: MOVCD Grown monolithic structure of a 1.5μm RayCan VCSEL.

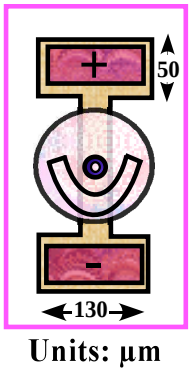

Figure 3.21: Bottom-emitting on-chip RayCan VCSEL with 1.3μm operation wavelength.

The VCSEL chip, integrated to the sub-mount is presented in figure 3.22. Integration to the sub-mount provided solution to the above-discussed problems.

It allowed:

- The utilization of the VCSEL-chip in top-emitting configuration that in turn made optical power collection using denuded single-mode and multimode optical fibers possible.

- The powering-up of the VCSEL-chip using 125 μm pitch GS probes already available in the laboratory.

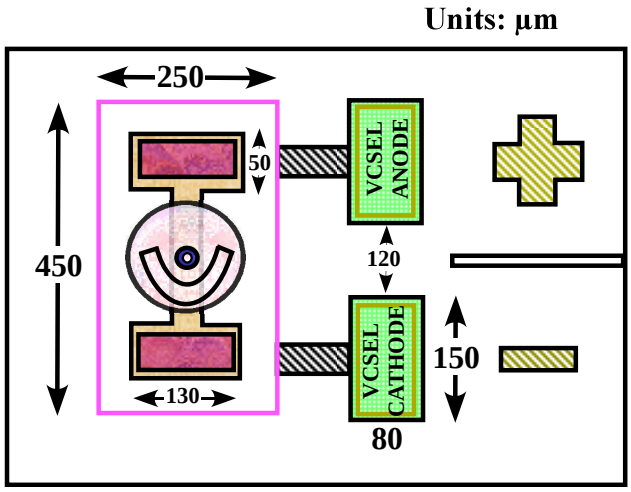

Figure 3.22: 1.3μm RayCan VCSEL with sub-mount.

Furthermore, the intent of optical injection-locking experiments was observation of the enhanced S_{21} response. This objective was compromised by the employment of the sub-mount, as the S_{21} response was limited by the parasitic transmission line frequency. Figure. 3.23 presents the free-running S_{21} response of a 1.3 μm RayCan VCSEL. It is clear that the resonance peak shifts toward higher frequencies with increasing bias currents but due to the presence of parasitics, introduced by the sub-mount assembly, the cut-off frequency does not increase significantly. The presence of air-gaps in the VCSEL structure implies lower intrinsic cut-off frequencies. The inevitable utilization of the sub-mount assembly, combined with the above-mentioned structural deficiency, render these VCSELs relatively low frequency operation devices. It is perhaps due to this reason that the 10 Gbps modules supplied by RayCan employ four VCSELs in parallel configuration to achieve 10Gbps bit rate, as opposed to Vertilas 10Gbps modules that are composed of only one VCSEL.

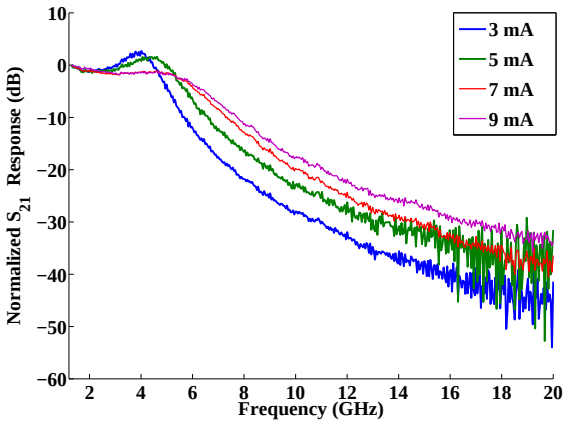

Figure 3.23: Free-running S_{21} response of a RayCan VCSEL emitting at 1.3μm.

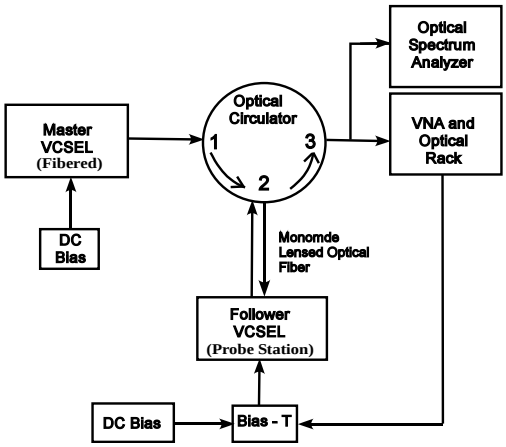

Figure 3.24: Schematic representation of the test-bench employed for injection-locking experiments using RayCan VCSELs emitting at 1.3μm.

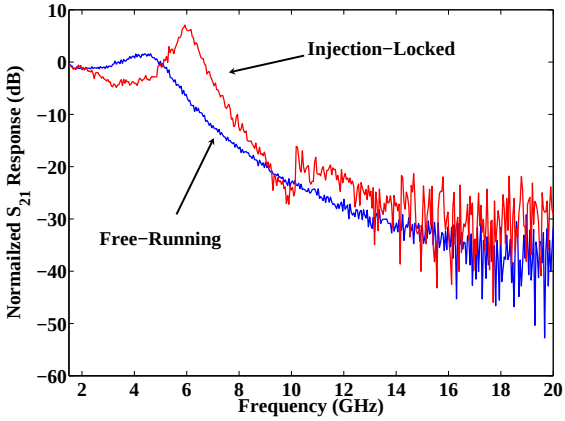

Figure 3.25: S_{21} response of an optically injection-locked RayCan VCSEL emitting at 1.3μm operating in the positive frequency detuning regime.

3.2.3.2 Injection Locking Experiments

The availability of fibered components however simplified the test-bench considerably. In stead of using two probe-stations for master and follower VCSELs respectively, only one probe-station was used since only the follower VCSEL was used in the on-chip configuration. The utilization of a pigtailed master VCSEL also increased the available optical power and allowed the elimination of the OSA from the injection-locking setup. Figure. 3.24 presents the optical injection-locking test-bench used for RayCan VCSEL experiments schematically.

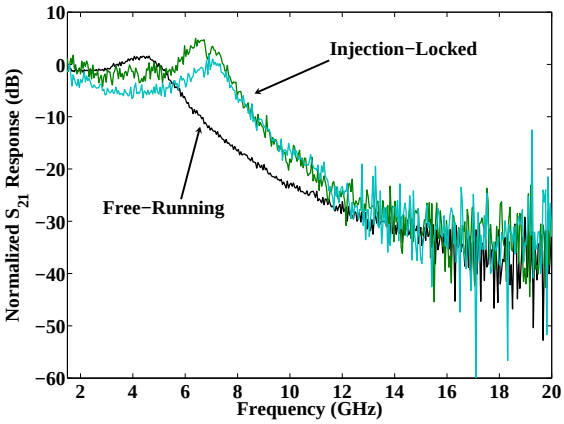

Figure 3.26: S_{21} response of an optically injection-locked RayCan VCSEL emitting at 1.3μm operating in the negative frequency detuning regime.

The utilization of a pigtailed master VCSEL made the test-bench considerably compact and increased the available optical power but despite these advantages, the follower VCSEL injection-locked S_{21} spectra do not exhibit very large resonance frequencies. Figure 3.25 presents the S_{21} response of an optically injection-locked RayCan follower VCSEL, in the positive frequency detuning regime. Compared to the free-running responses presented in figure 3.23, it is clear that an increased resonance frequency is observed. Also, due to operation in the positive frequency detuning regime, the S_{21} is undamped and therefore the resonance peak is very pronounced.

On the other hand, figure 3.26 presents the optically injection-locked RayCan follower VCSEL S_{21} response in negative frequency detuning regime. The response is damped and the resonance peaks are less prominent than the response given in figure 3.25. It must however be noticed that due to the air-gap based structure, the optical injection-locked RayCan VCSEL S_{21} responses do not exhibit resonance and cut-off frequencies as high as those obtained using BeamExpress VCSELs and presented in Figures. 3.14, 3.15, 3.17 and 3.19.

3.3 Measurement Simulation Comparison

We present the comparison between experimentally obtained S_{21} curves with the frequency response curves obtained using the mathematical model explained in the preceding chapter. Two important parameters of note, the frequency detuning ($\Delta\omega$) and the injected photon density (S_{inj}) have been varied in order to obtain the best-fit simulation curves. Figures 3.27, 3.28 and 3.29, give the comparison between measured and calculated frequency responses. Table 3.1 summarizes the values of detuning frequency and injected photon density, used to obtain the calculated S_{21} curves.

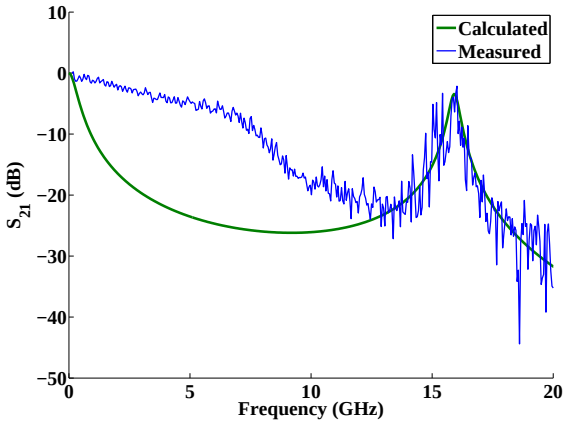

Figure 3.27: Comparison between the experimental and simulated S_{21} response of an optically injection-locked BeamExpress VCSEL emitting at 1.3μm.

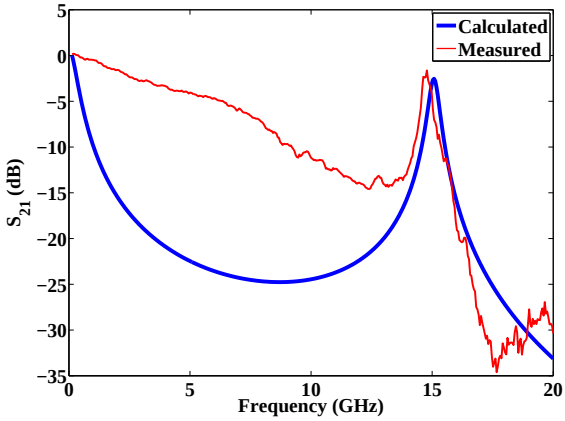

Figure 3.28: Comparison between the experimental and simulated S_{21} response of an optically injection-locked BeamExpress VCSEL emitting at 1.3μm.

The difference at low frequencies, between the calculated and experimental curves, is probably due to the insufficient injected optical power. During the experiments using on-chip VCSELs, injecting sufficient amounts of optical powers into the lensed single-mode optical fiber has consistently been identified as the most challenging aspect of the exercise.

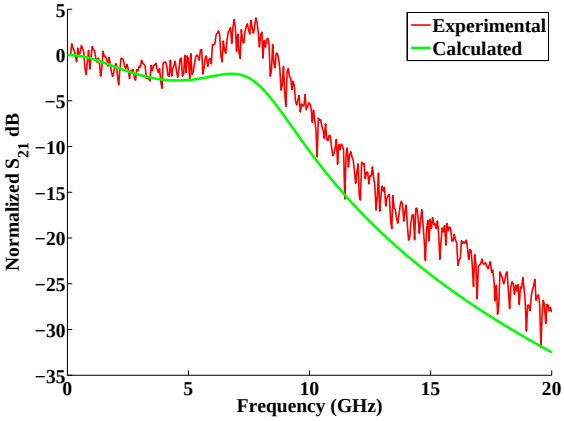

Figure 3.29: Comparison between the experimental and simulated S_{21} response of an optically injection-locked BeamExpress VCSEL emitting at 1.3μm.

Figure	Injected Photon Density (cm^{-3})	Frequency Detuning (GHz)
Figure 3.27	1.25x10^{10}	-80
Figure 3.28	1.05x10^{11}	-200
Figure 3.29	1.54x10^{10}	-80

Table 3.1: Injected photon density and frequency detuning values for the calculated curves presented in figures 3.27, 3.28 and 3.29.

3.4 Conclusion and Discussion

Experimental studies of VCSEL-by-VCSEL optical injection-locking phenomena were presented in this chapter. It was demonstrated that optical injection-locking suppresses only the Fabry-Pérot modes of an optical cavity. The transverse modes commonly found in VCSELs remain largely unaffected by optical injection-locking. VCSEL-by-VCSEL optical injection-locking was presented using fibered single-mode VCSELs and fundamental and side-mode suppression phenomena were demonstrated.

Optical injection-locking of on-chip VCSELs was suggested, in order to observe the parasitics free S_{21} response. Three different operation regimes were explored using VCSEL-by-VCSEL optical injection-locking. Resonance frequencies as high as 17 GHz were presented for follower VCSELs operating in positive frequency detuning regimes. It was however observed that positive frequency detuning increases the resonance frequency but limits the effective bandwidth of the injection-locking system which is not desirable for VCSEL employment in high bit rate telecommunication system.

The zero, or slightly negative detuning regime proposes flat, highly damped S_{21} curves. An increase in injected optical power, while remaining keeping the VCSELs in negative detuning configuration, results in the increase of effective bandwidth. Effective bandwidths as

high as 10 GHz, using optical injection-locking, have been demonstrated. It must be noted that the free-running cut-off frequency of the VCSELs used is about 5 GHz.

In order to simplify the optical injection-locking setup, the utilization of a fibered master VCSEL has been proposed. Such a configuration also increases the effective available optical power. Optically injection-locked follower VCSEL S_{21} response has been presented in different operating conditions. Experimental results and numerical calculations using the mathematical model have been compared.

Bibliography

[1] K. Iwashita and K. Nakagawa, "Suppression of Mode Partition Noise by Laser Diode Light Injection," *Microwave Theory and Techniques, IEEE Transactions on*, vol. 82, no. 10, pp. 1657–1662, Oct 1982.

[2] A. Bacou, "Caractérisation et Modélisation optoélectronique de VCSEL à grande longueur d'onde pour sous-ensembles optiques intégrés," Ph.D. dissertation, Institut Supérieur de l'Aéronautique et de l'Espace, 2008.

[3] C.-H. Chang, L. Chrostowski, and C. Chang-Hasnain, "Injection locking of VCSELs," *IEEE Journal of Selected Topics in Quantum Electronics*, vol. 9, no. 5, pp. 1386–1393, Sept.-Oct. 2003.

[4] M.-R. Park, O.-K. Kwon, W.-S. Han, K.-H. Lee, S.-J. Park, and B.-S. Yoo, "All-epitaxial InAlGaAs-InP VCSELs in the 1.3-1.6-μm Wavelength Range for CWDM Band Applications," *IEEE Photonics Technology Letters*, vol. 18, no. 16, pp. 1717–1719, Aug. 2006.

Chapter 4 Frequency Response Extraction and RIN Measurements

Direct modulation is preferred in modern telecommunication systems in order to avoid the costs presented by external modulators. Packaging and transmission line parasitics however degrade the device performance and limit the high frequency response. To estimate the VCSEL intrinsic frequency response, we have presented and utilized a rate equation based model in precedent chapters. In effect, the same model can be employed to separate the intrinsic device response from the overall observed packaged system response. The procedure is denoted as "Frequency Response Subtraction" and would be treated extensively here.

The second half of this chapter deals with RIN measurements of fibered free-running and injection-locked VCSELs. RIN variation as function of wavelength detuning is observed. A RIN improvement of about 10 dB is reported under injection-locking conditions.

4.1 Frequency Response Subtraction

Modulation of on-chip VCSELs allows us to observe the intrinsic frequency response but coupling optical power from the VCSEL into a single-mode denuded fiber can prove to be challenging. Modulation of fibered VCSELs allows to work with sufficiently high power levels but the packaging parasitics hinder the observation of intrinsic response. A technique has been proposed [1] to extract the intrinsic frequency response of a DFB laser using S_{21} measurements and the device mathematical model. A comprehensive mathematical model for long wavelength VCSELs was developed by A. Bacou and is presented in [2].

4.1.1 Extraction Procedure

The basic concept of the extraction procedure can be summarized as follows:

- By subtracting the S_{21} response for a bias current just above the threshold, from the S_{21} responses well above the threshold, the parasitic influences can effectively be eliminated since the result of the subtraction depends only on the bias current related S_{21} response variation.

- A mathematical model is defined and the subtraction procedure is repeated to obtain calculated S_{21} curves similar to those obtained experimentally.

- The experimentally obtained curves are fitted to the calculated curves by varying the mathematical model parameters.
- The S_{21} curves are reconstructed using the mathematical model parameters obtained after fitting.

4.1.1.1 Mathematical Model

The VCSEL resonance frequency response f_r can be expressed in terms of variables Y and Z that in turn depend upon VCSEL intrinsic parameters. Y corresponds to the laser frequency response damping factor and along with Z can be used to estimate the laser resonance frequency. Y and Z can be expressed mathematically as follows [1],

$$Y = v_g a_0 \frac{\overline{S}}{1+\epsilon\overline{S}} + \frac{1}{\tau_e} - \Gamma v_g a_0 (N_{th} - N_{tr}) \frac{1}{(1+\epsilon\overline{S})^2} + \frac{1}{\tau_P} \tag{4.1}$$

$$Z = v_g a_0 \frac{\overline{S}}{1+\epsilon\overline{S}} \frac{1}{\tau_P} + (\beta - 1) \frac{\Gamma v_g a_0}{\tau_N} (N_{th} - N_{tr}) \frac{1}{(1+\epsilon\overline{S})^2} + \frac{1}{\tau_e \tau_P} \tag{4.2}$$

Where N_{th} and N_{tr} are the electron threshold and transparency densities, a_0 the differential gain coefficient, S the photon density, v_g the group velocity, β the spontaneous emission coefficient and Γ the confinement factor. τ_N and τ_P are the the carrier and photon lifetimes respectively.

The system transfer function $H(f)$ and the resonance frequency f_r can be expressed in terms of Y and Z as follows:

$$f_r = \frac{1}{2\pi}\sqrt{Z - 0.5Y^2} \tag{4.3}$$

$$H(f) = \frac{{f_r}^2}{({f_r}^2 - f^2) + jfY\frac{\pi}{2}} \tag{4.4}$$

The transfer function of a VCSEL can therefore be calculated using the parameters presented in Table. 4.1.

Figure 4.1 presents the calculated normalized S_{21} response of a VCSEL, using the intrinsic parameters given in Table.4.1.

4.1.1.2 Experimental Results

The devices used are fibered, single-mode RayCan VCSELs emitting at 1.3μm wavelength. The experimentally obtained S_{21} curves for different bias currents have been presented in Fig. 4.2. The packaging cut-off frequency is about 4 GHz. The intrinsic response up to 4 GHz (i.e. for the bias current values of 3mA and 4mA) can be easily observed. S_{21} response

Parameter	Units	Value
τ_N	ns	0.61
N_{th}	cm^{-3}	5.33x10^{18}
N_{tr}	cm^{-3}	3.24x10^{18}
a_0	cm^2	4.8x10^{-16}
v_g	cm/s	7.7x10^{9}
ϵ	cm^3	2.2x10^{-17}
τ_P	ps	6.4
S	cm^{-3}	2.5x10^{15}

Table 4.1: Long wavelength VCSEL intrinsic parameters used to simulate the small-signal [3].

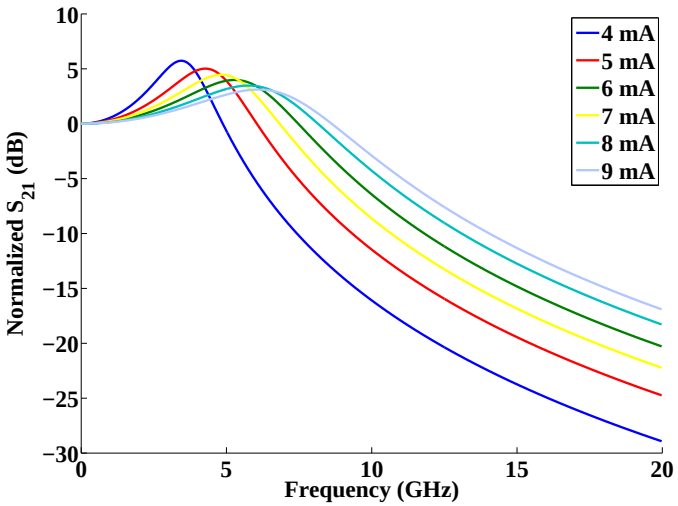

Figure 4.1: Calculated S_{21} response curves for different bias currents.

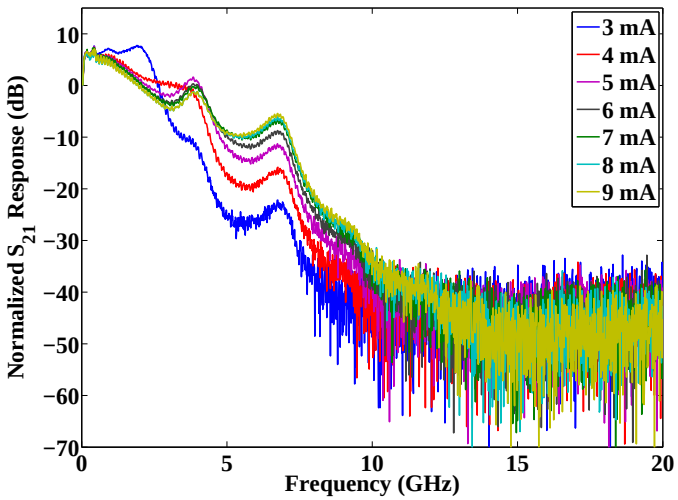

Figure 4.2: 1.3μm RayCan VCSEL experimental S_{21} response curves for different bias currents.

curves for higher bias current values therefore are not observable since the package cut-off frequency limits the device frequency response to 4 GHz.

Following the steps described in 4.1.1, we obtain the subtracted curves presented in Fig.4.3. The curves are obtained by subtracting the S_{21} response at 3mA from the S_{21} responses at 5mA, 6mA, 7mA and 8mA respectively. A smoothing filter is applied to the S_{21} data in order to remove the high frequency perturbations ($>$ 10 GHz) in the frequency response. Applying a similar procedure to the calculated curves presented in Fig. 4.1, we obtain the calculated subtracted response curves which will be used in the fitting procedure. The subtracted calculated curves are presented in Fig. 4.4. The parameters used to calculated these curves, presented in Table. 4.1 are then varied to obtain a fit to the experimental curves presented in figure 4.3.

4.1.1.3 Fitting Procedure

The fitting procedure consists of applying the "linear regression" fitting tool provided in MATLAB to the measured and modeled subtracted S_{21} responses. Figure 4.5 presents a comparison between measured and calculated S_{21} responses for a bias current of 8mA. The linear regression method tries to find the model parameters that fit best to the profile of measured data. The best-fit in this case is determined by using the "least squares method" incorporated in MATLAB.

The initial values provided to the fitting model are presented in Table. 4.2:

The resulting fit is presented in figure 4.6. A repetition of the fitting procedure for all bias currents yields the fitted values of Y and Z parameters for each bias current, that are then used to reconstruct the S_{21} response curves. Table. 4.3 presents the final values for Y and Z parameters obtained after the fitting procedure. The S_{21} curves for different bias

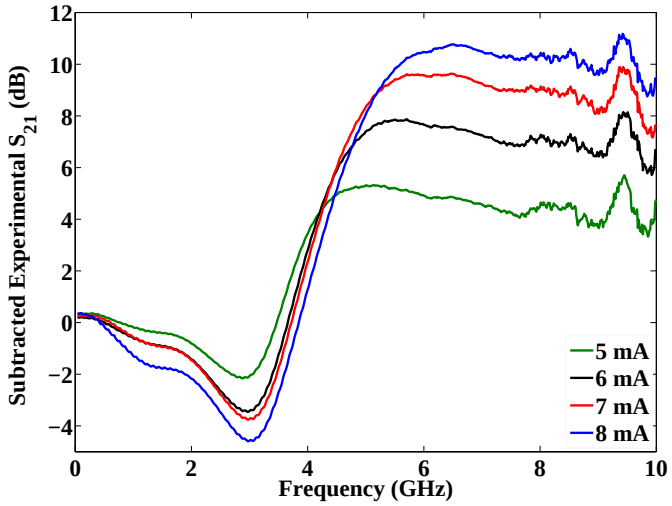

Figure 4.3: 1.3μm RayCan VCSEL subtracted experimental S_{21} response curves for different bias currents.

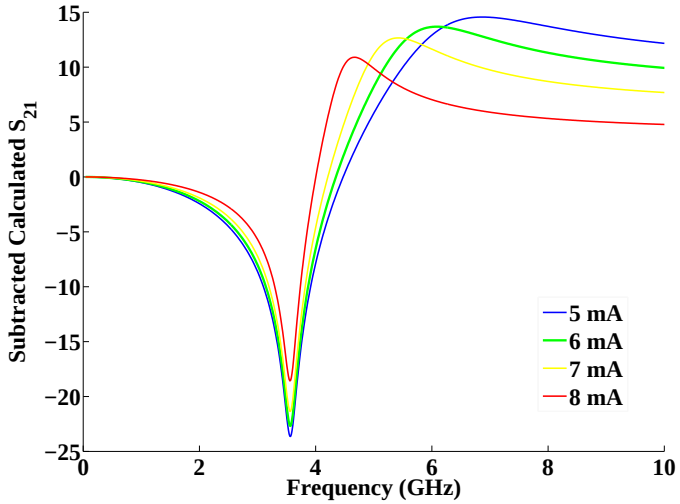

Figure 4.4: 1.3μm RayCan VCSEL subtracted calculated S_{21} response curves for different bias currents.

Parameter	Value
Y_{4mA}	1.057x10^9
Z_{4mA}	5.03x10^{20}
Y_{5mA}	5.16x10^9
Z_{5mA}	8.13x10^{20}

Table 4.2: Initial values used to calculate the best-fit between calculated and experimental curves.

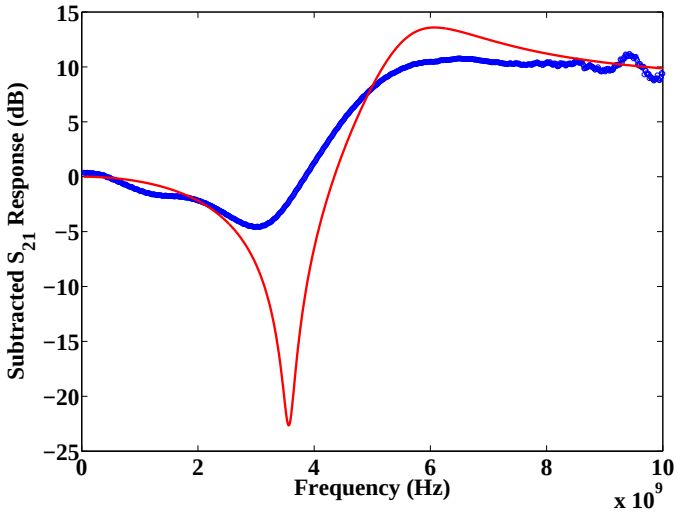

Figure 4.5: Comparison between measured and calculated subtracted responses for a bias current of 8mA before the application of fitting procedure.

current values obtained using these parameters are presented in figure 4.7.

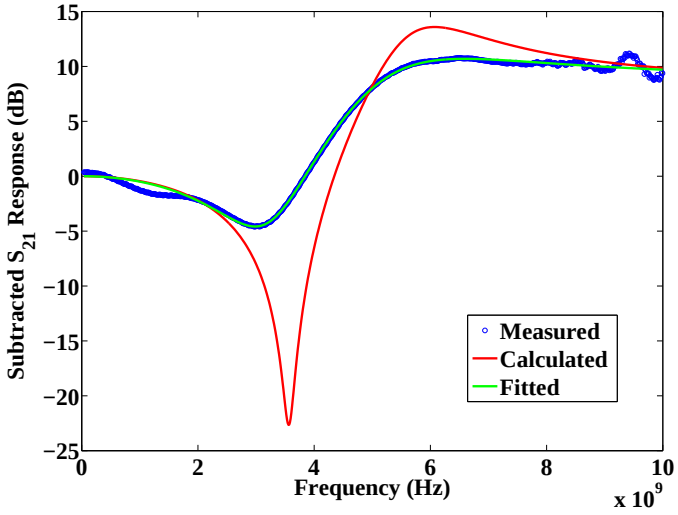

Figure 4.6: Comparison between measured, calculated and fitted subtracted responses for a bias current of 8mA after the application of fitting procedure.

4.1.1.4 1550 Fibered RayCan VCSELs

Application of a similar procedure on 1.5μm fibered RayCan VCSELs yields characteristic S_{21} curves. Figure 4.8 presents the parasitic limited S_{21} curves obtained using 1.5μm single-mode RayCan VCSELs. Table. 4.3 gives the values for Y and Z parameters obtained after employing the fitting procedure. Finally figure 4.9 presents the S_{21} curves reconstructed using the parameters presented in Table. 4.3.

Current	Y(1.3μm)	Z(1.3μm)	Y(1.5μm)	Z(1.5μm)
5 mA	1.30x10^{10}	7.5x10^{20}	9.16x10^{9}	3.4x10^{20}
6 mA	1.60x10^{10}	9.7x10^{20}	1.17x10^{10}	4.5x10^{20}
7 mA	1.79x10^{10}	1.15x10^{21}	1.73x10^{10}	5.21x10^{21}
8 mA	2.10x10^{10}	1.35x10^{21}	1.49x10^{10}	6.68x10^{21}

Table 4.3: Final values of Y and Z parameters for different bias currents after the fitting procedure.

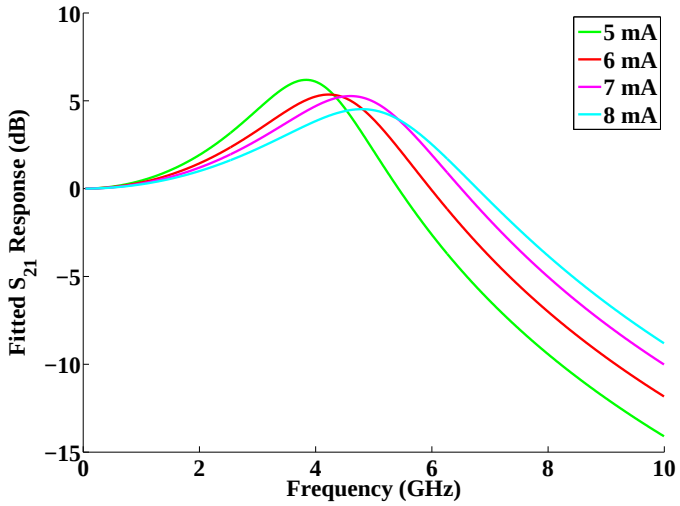

Figure 4.7: Reconstructed S_{21} response curves using the Y and Z values presented in Table. 4.3.

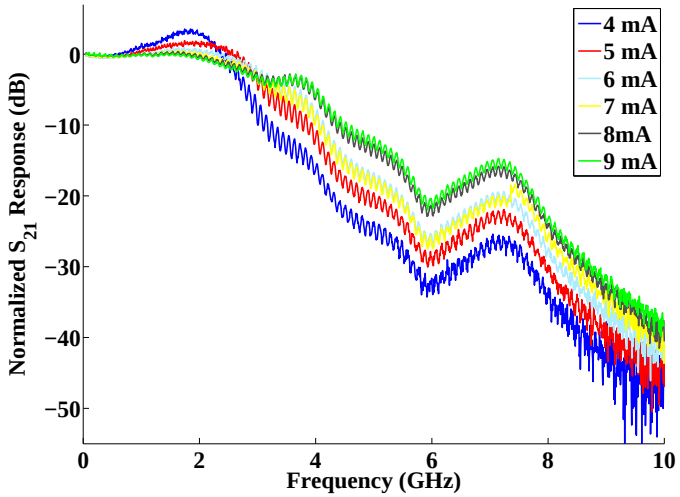

Figure 4.8: 1.5μm RayCan VCSEL experimental S_{21} response curves for different bias currents.

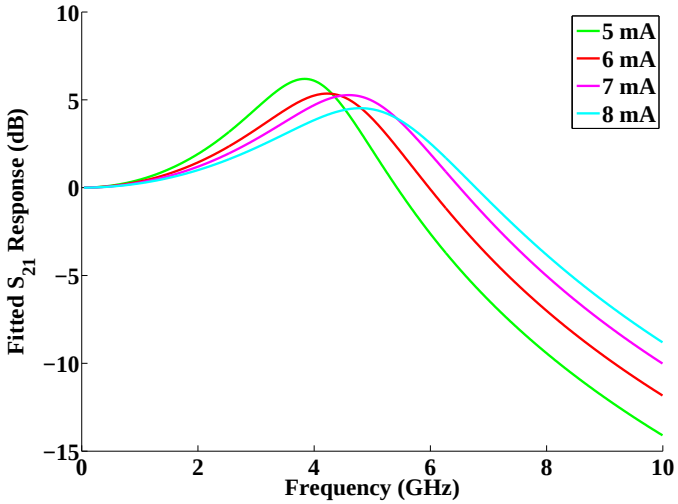

Figure 4.9: Reconstructed S_{21} response curves using the Y and Z values presented in Table. 4.3.

4.1.2 Injection-Locked VCSELs

Several research groups have demonstrated high resonance frequencies and bandwidths using optical injection-locking. If the device is unpackaged, the system frequency response is observable on the VNA, on the other hand, the frequency response of a packaged injection-locked diode must be post-treated in order to extract the useful information. The optically injection-locked follower VCSEL frequency responses presented in [4] and [5] have been obtained using unpackaged on-chip VCSELs and therefore require no post-experimental treatment. On-chip VCSEL utilization allows the observance of parasitics free S_{21} response but its benefits are countered by the particularly challenging issue of difficulty in coupling optical power from the VCSEL emission window to the denuded optical fiber. This reduces the available optical power and in turn limits the frequency response evolution with respect to optical power.

4.1.2.1 Injection-Locked Fibered RayCan VCSELs

Several pioneering VCSEL optical injection-locking publications, presenting very high resonance frequencies, use extraction to present the optically injection-locked VCSEL S_{21} response [7], [6]. Figure 4.10 presents the fitted optically injection-locked follower VCSEL S_{21} curves presented in [6]. Remarkably, the slopes of the injection-locked S_{21} responses and the free-running S_{21} response presented in [6] are identical and correspond to the slope of a classical second-order system. It must be noted that the curves presented in figure 4.10 are for an injection-locked system operating in a positive detuning frequency regime. Experiments with on-chip VCSELs [4], [5] however, have demonstrated the existence of low-frequency dips in the S_{21} response of optically injection-locked follower VCSELs, operating in the posi-

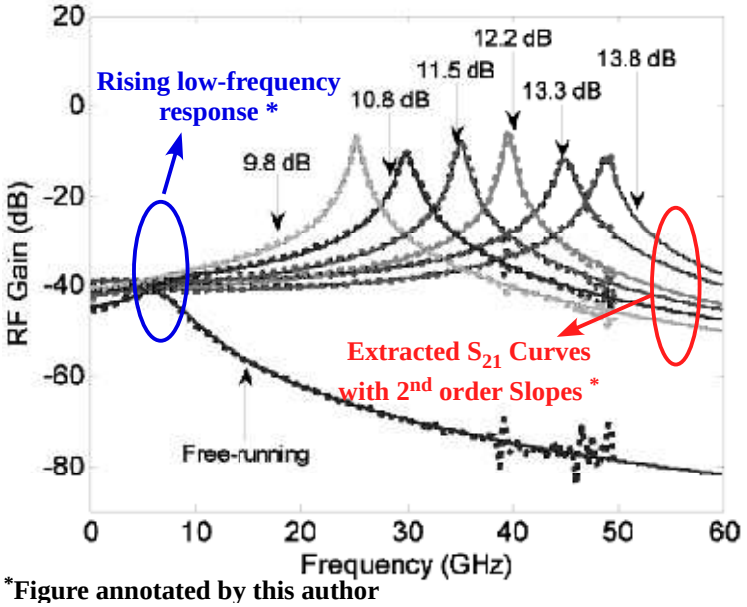

*Figure annotated by this author

Figure 4.10: Optically injection-locked follower VCSEL S_{21} response curves presented by Chrostowski et al. in [6].

tive frequency detuning regime. The extracted S_{21} curves, presented in figure 4.10 illustrate no low-frequency dips, even for very high values of negative wavelength detuning. In our opinion, the absence of an accurate model has led to extracted S_{21} responses, that are not representative of the optical injection-locking conditions.

Injection-locked S_{21} responses for 1.5μm RayCan VCSELs are presented in figure 4.11. The S_{21} response is limited by the presence of the packaging parasites. The mathematical model presented in Chapter. 2 is used to develop a fitting mechanism, in order to extract the S_{21} response of fibered injection-locked VCSELs. By following the steps described in 4.1.1, we obtain the subtracted S_{21} curves for an injection-locked system, in order to eliminate the parasitics influence. These subtracted responses are then fitted to the calculated subtracted responses in order to determine the appropriate injected optical power, that would fit to the experimental results.

Figure 4.12 presents a comparison between the experimental, calculated and fitted curves for 1.55μm injection-locked VCSELs. Figure 4.13 gives the extracted S_{21} responses for 1.55μm injection-locked VCSELs, calculated using the parameters obtained after the fit. A maximum resonance frequency value of 14 GHz is obtained.

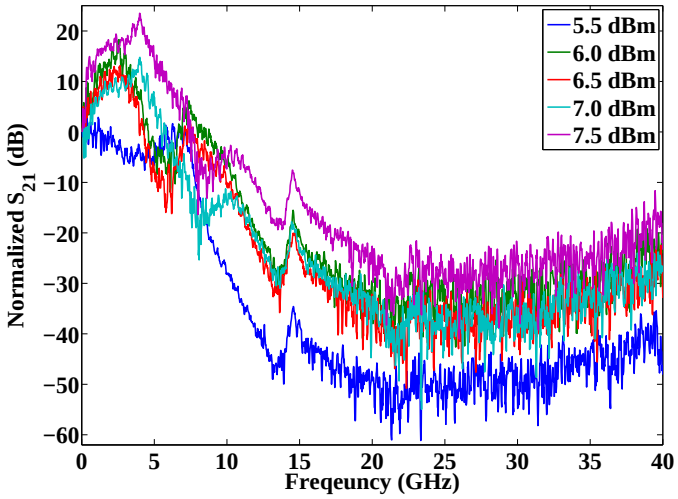

Figure 4.11: RayCan 1.5μm optically injection-locked follower VCSEL S_{21} response curves for different incident optical powers.

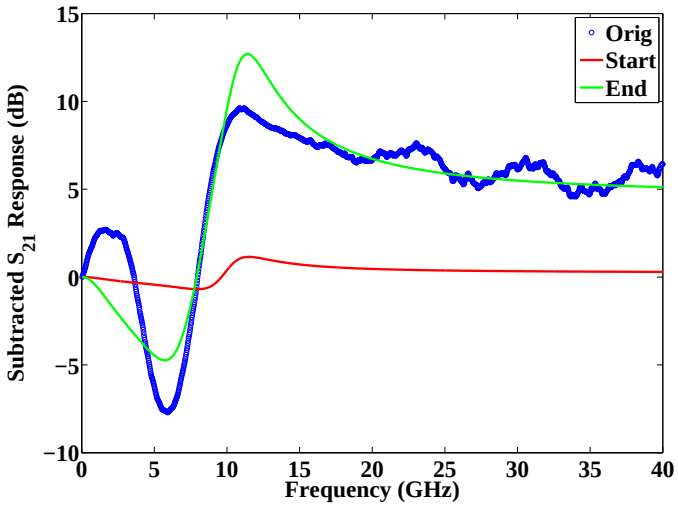

Figure 4.12: Subtracted calculated optically injection-locked follower VCSEL S_{21} response curves for different incident optical powers.

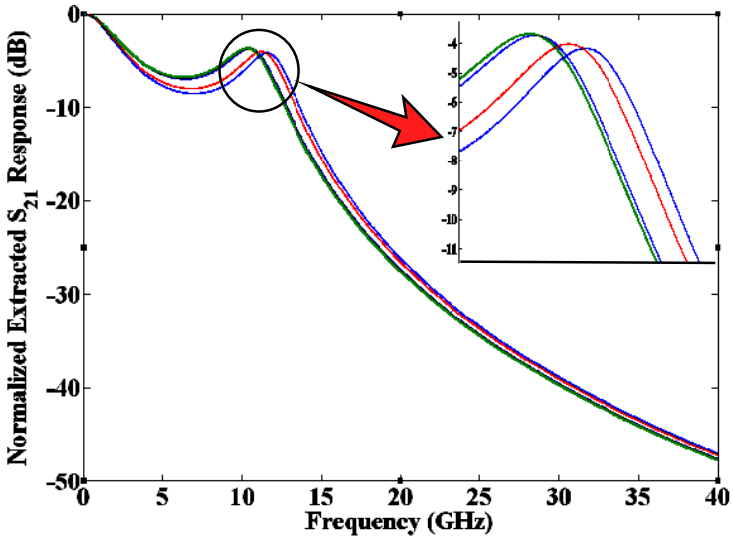

Figure 4.13: Reconstructed S_{21} response curves for injection-locked 1.5μm RayCan VCSELs. The detuning is kept constant at 10 GHz.

4.2 Relative Intensity Noise (RIN) measurements

The intensity of a laser signal undergoes small fluctuations around a constant value. The ratio of magnitude of these fluctuations to the intensity of emitted optical power is defined as relative intensity noise or "RIN". The Signal to Noise Ratio (SNR) of a laser can be expressed mathematically as [8]:

$$SNR = \frac{\langle {i_S}^2 \rangle}{\langle {i_N}^2 \rangle} \tag{4.5}$$

where $\langle i_S \rangle$ and $\langle i_N \rangle$ are mean-squared signal and noise currents. Substituting the values of $\langle i_S \rangle$ and $\langle i_N \rangle$ in eq. 4.5 for a modulated signal we have,

$$SNR = \frac{\langle (P_1 sin\omega t)^2 \rangle}{\langle \delta P(t)^2 \rangle} = \frac{m^2}{2} \frac{{P_0}^2}{\langle \delta P(t)^2 \rangle} \tag{4.6}$$

m is the modulation index and is given by $m = P_1/P_0$. Figure 4.14 presents the concept of intensity noise graphically. The relative intensity noise can the be expressed as,

$$RIN = \frac{\langle \delta P(t)^2 \rangle}{{P_0}^2} \tag{4.7}$$

where $\langle \delta P(t)^2 \rangle$ is the mean-square of the assumed Gaussian noise distribution. RIN is often expressed in dB. The expression for RIN in dB can be given as

$$RIN_{dB} = 10 \cdot log_{10} \frac{\langle \delta P(t)^2 \rangle}{{P_0}^2} \tag{4.8}$$

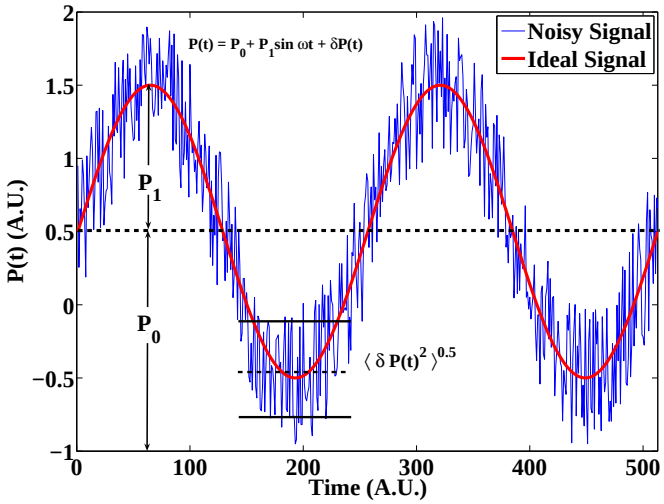

Figure 4.14: Example of noise in modulated laser signal for analog applications.

The test bench utilized for RIN measurements of free-running RayCan VCSELs emitting at 1.55μm is presented in figure 4.15. The fibered VCSELs are powered-up using a stable KEITHLEY DC power supply. The output optical power is converted into electrical power using a Lasertron high speed photodiode. The electrical output is amplified using a transimpedance amplifier and fed to the electrical spectrum analyzer.

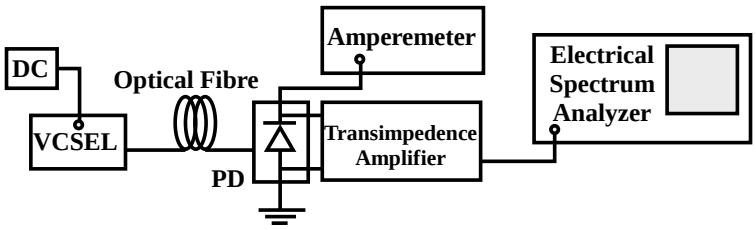

Figure 4.15: Testbench for RIN measurements of 1.5μm free-running Raycan VCSELs

The RIN of a laser diode is then calculated using the following mathematical expression:

$$RIN = \frac{\frac{P_{Obs}-P_{Analyzer}}{G} - 2qI_{PD}R_{Load}}{{I_{PD}}^2 R_{Load}} \tag{4.9}$$

where,

- P_{Obs} is the optical power observed on the electrical spectrum analyzer
- $P_{Analyzer}$ is the electrical spectrum analyzer noise floor power
- R_{Load} is the electrical spectrum analyzer load resistance

- I_{PD} is the photo diode current
- G is the transimpedance amplifier gain, and
- q is the electron charge

Since a photodiode is used for the O/E conversion, the photodiode shot noise contribution to the VCSEL RIN measurement must be taken into account. The expression $2qI_{PD}R_{Load}$ is the photodiode shot noise which must be subtracted from the VCSEL output power fluctuations before the RIN calculation. The $P_{Analyzer}$ comprises of the electircal spectrum analyzer noise floor which is defined by the intrinsic thermal noise of the instrument. The typical value of the noise floor power for the instrument used in these experiments is about -165dB/Hz. This value imposes a limit on the VCSEL observable noise and therefore noise level below this threshold can not be measured. Since typical VCSEL RIN values are found in the 145-150 dB/Hz range, this instrument noise floor value is sufficient enough to carry-out the RIN-related experiments. The RIN measurements of a 1.55μm free-running RayCan VCSEL are presented in figure 4.16.

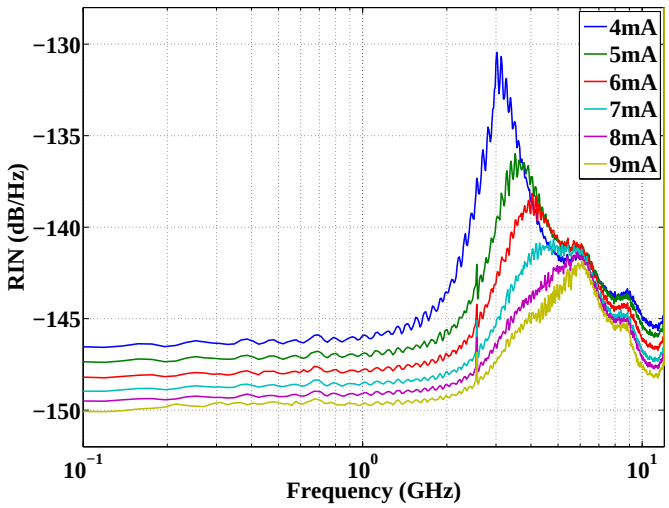

Figure 4.16: RIN measurements for a 1.55μm RayCan VCSEL for different bias currents.

The RIN measurements presented in figure 4.16 show the intrinsic resonance frequency peak of the VCSEL. They also give the intrinsic relaxation oscillation frequency's evolution with respect to increasing bias current. The resonance frequency increases with increasing bias current while the resonance peak damping is more pronounced with increasing bias currents. Since RIN measurements do not involve direct RF modulation of lasers, the problems associated with modulation frequency related parasitics are automatically eliminated. RIN curves serve therefore as excellent estimates of the intrinsic direct modulation bandwidths of lasers. The highest value of resonance frequency for the VCSELs under test is found to

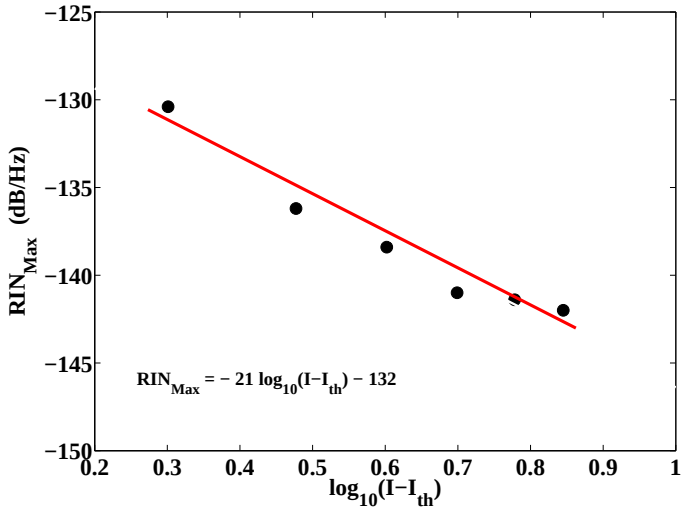

Figure 4.17: Peak RIN plotted as a function of increasing bias current. The black dots signify the peak RINs for different bias currents, while the solid red line is the mathematical fit.

be about 6 GHz. Equation 4.7 shows that for increasing optical output powers, the RIN decreases. Figure 4.16 demonstrates a decrease from -146 dB/Hz to -150 dB/Hz as a function of increasing bias currents.

The RIN dependence on laser bias current for conventional EELs can be mathematically characterized as [8]:

$$RIN(f_R) \propto (I_{bias} - I_{th})^{-3} \tag{4.10}$$

In order to compare the VCSEL RIN peak bias current dependence,to that of the EELs, the RIN is plotted against $log_{10}(I_{bias} - I_{th})$ [1]. The resulting plot is presented in figure 4.17

The equation for the linear fit of this plot is

$$RIN_{Max} = -21log_{10}(I_{bias} - I_{th}) - 132 \tag{4.11}$$

From equation 4.11, it can be deduced that the slope is -21, which when converted to linear scale results in:

$$RIN(f_R) \propto (I_{bias} - I_{th})^{-2} \tag{4.12}$$

which demonstrates that the VCSEL RIN decays slowly as compared to EEL RIN and the difference of order between the two respective decays is 1. This can be explained

[1]Since the RIN is generally measured and expressed in dB/Hz, for the reason of being consistent, it is plotted as the logarithm of the difference between the bias and threshold currents.

by the greater cavity size and consequently greater bias currents of the EEL lasers, which are responsible for production of a greater number of photons inside the EEL cavity. The EELs therefore have a better simultaneous to spontaneous emission ratio and hence a rapidly decreasing RIN with increasing bias currents. This also explains the generally low values of RIN for EELs when compared to that of VCSELs.

4.2.1 RIN Measurements of Injection-Locked VCSELs

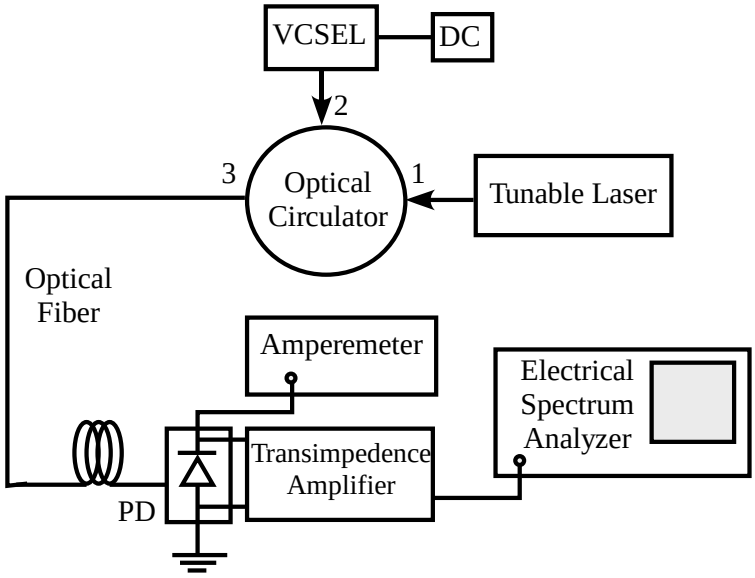

Figure 4.18: Testbench for RIN measurements of injection-locked 1.5μm Raycan VCSELs.

The RIN measurements of injection-locked VCSELs were undertaken with two specific objectives in mind.

- Observe the resonance frequency value and peak form variation with respect to wavelength detuning and incident optical power.
- Observe the influence of injected optical power on the RIN for a given bias current

The test bench for the RIN measurements of injection-locked VCSELs is presented in figure 4.18. This test bench is actually a combination of DC injection-locking experiments test bench and the free-running RIN measurements test bench presented previously. A tunable laser is used, via an optical circulator, to injection-lock a 1.55μm single-mode fibered RayCan VCSEL. The injection-locked output from the port 3 of the optical circulator is fed to the Lasertron photodiode for RIN measurements. Figure 4.19 presents the RIN curves for the master tunable laser. The master laser RIN is about 160 dB/Hz for a bias current of 100mA and an output optical power of 7 dBm.

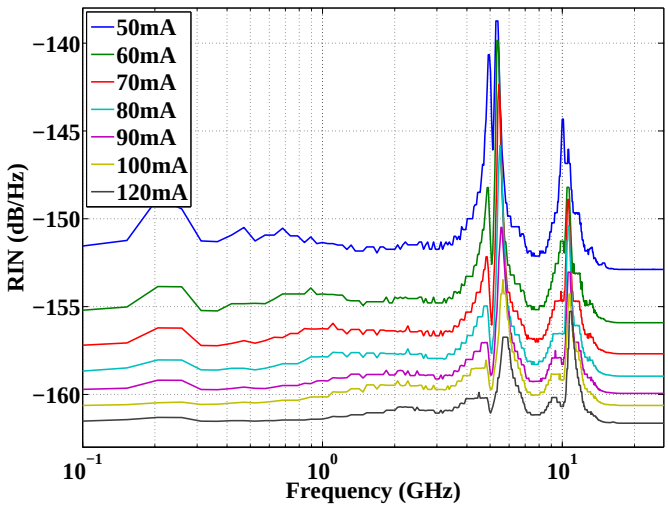

Figure 4.19: Tunable laser RIN curves for various bias currents

In previous chapters, we have discussed the frequency response of injection-locked VCSELs operating in positive or negative wavelength detuning regimes. As the resonance frequency of an injection-locked system increases, so does the complexity of a test bench, realized to observe the injection-locked follower VCSEL's S_{21} response. In case of fibered components, the parasitic limitations oblige us to utilize extraction techniques (developed and presented in preceding sections), for the observation of S_{21} response . RIN measurements however can be employed to observe the detuning response of an injection-locked system as the VCSEL is not modulated and works in the so called "Static" operating conditions.

4.2.1.1 Negative Wavelength Detuning Regime

Figure 4.20 presents the RIN of an injection-locked VCSEL under various injection-powers. A bias current of 5 mA has been maintained throughout this series of measurements, in order to eliminate the bias current dependent damping of RIN curves. The VCSELs are injection-locked at the negative wavelength detuning edge of the locking range.

The generation of high frequency beat notes, as a resulting of positive frequency detuning, inside the VCSEL optical cavity, results in an under-damped response. The injected optical power increases the effective locking-range which allows to sustain high values of $\Delta\omega = \omega_{Master} - \omega_{Follower}$ and hence high values of resonance frequency. The resonance frequency observed in figure 4.20 increases from 6 GHz to about 12 GHz under the influence of increasing optical power and detuning.

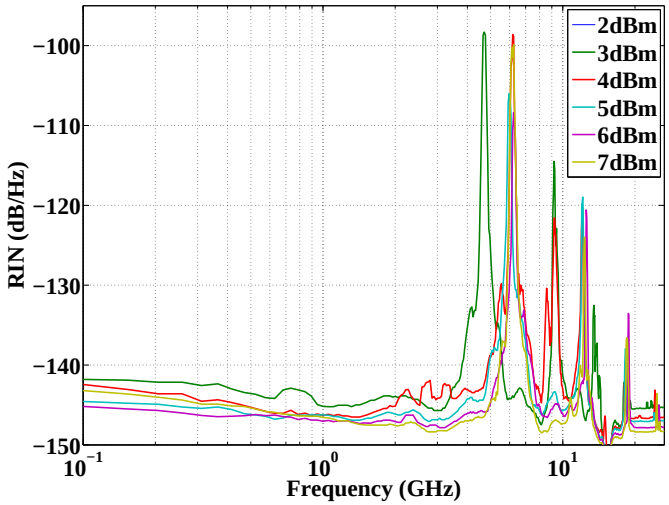

Figure 4.20: RIN measurements for an injection-locked 1.55μm RayCan VCSEL for different optical incident powers. The VCSEL is injection-locked on the positive frequency detuning edge of the locking-range.

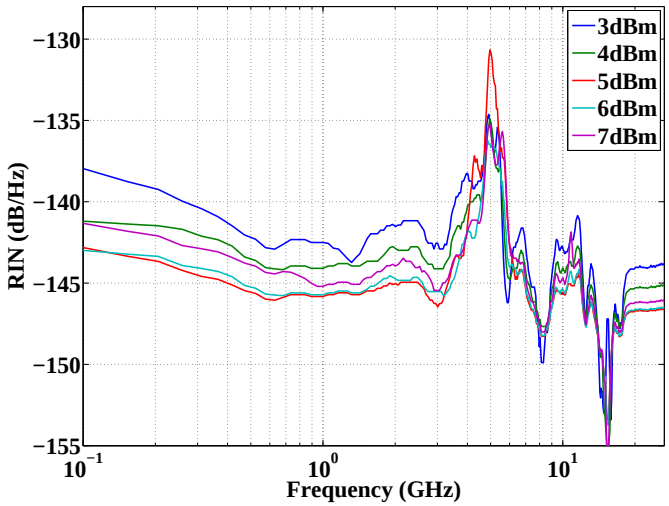

Figure 4.21: RIN measurements for an injection-locked 1.55μm RayCan VCSEL for different optical incident powers. The VCSEL is injection-locked on the negative frequency detuning edge of the locking-range.

4.2.1.2 Positive Wavelength Detuning Regime

On the other hand, when a VCSEL is injection-locked in the positive wavelength detuning mode, the beat note generated inside the optical cavity is smaller in value, and over-damped in shape. Moreover, the increase in locking-range due to increase in injected optical power is not symmetric due to the presence of α_H, the Henry factor. This asymmetry favors the locking-range extension in the negative wavelength detuning range. Consequently, the positive wavelength detuning curves are over-damped and exhibit little increase in resonance frequency value with increase in injected optical power. Figure 4.21 gives the RIN measurements for a 1.55μm fibered RayCan VCSEL, injection-locked at the edge of the positive frequency detuning regime. The resonance frequency peak is highly damped as compared to the curves obtained by working in the negative wavelength detuning regime. The bias current is kept constant at 5 mA through out this series of experiments, in order to eliminate the resonance frequency variation with respect to bias current variation.

Figure 4.22 compares different RIN curves obtained for a bias current of 5 mA. The three different curves present the VCSEL RIN in the free-running and injection-locked operating conditions. The injection-locked VCSEL resonance frequency is greater than the free-running VCSEL frequency. Moreover, the resonance frequency value and damping change as a function of wavelength detuning. For a bias current of 5 mA, the resonance frequency varies from 3.5 GHz to 6.5 GHz.

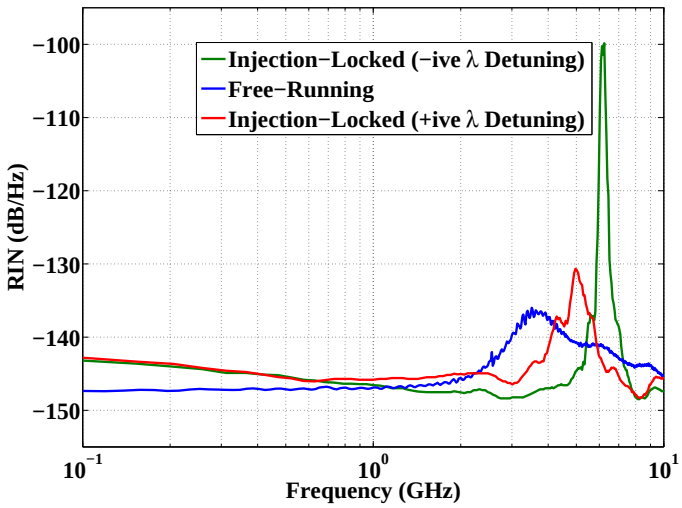

Figure 4.22: Comparison between the measured 1.5μm RayCan VCSEL RIN under different operating conditions. The three different curves present the RIN under free-running, positive wavelength detuning and negative wavelength detuning regimes.

A difference between the free-running VCSEL RIN and the injection-locked VCSEL RIN curves, apart from the changing resonance frequency values, is immediately visible. The injection-locked VCSEL RIN tends to have a higher low-frequency noise value than the free-

running VCSEL RIN. Two different explanations can be proposed for this phenomenon. As Sciamanna et al. have demonstrated that this might be due to the transvers-mode switching phenomenon visible in the optically injection-locked VCSELs [9], [10]. On the other hand, the optically injection-locked VCSEL RIN resemebles that of a multimode VCSEL which, due to mode competition, has a higher RIN at lower frequencies. The frequency-beating inside the single-mode injection-locked VCSEL optical cavity might be regarded as analogous to a multimode VCSEL cavity with mode competition resulting in an increased RIN at lower frequencies.

4.2.1.3 RIN Improvement

RIN improvement under optical injection-locking has been demonstrated previously by different research groups [11], [12]. The comparison between free-running and injection-locked spectra of a 1.55μm RayCan VCSEL are presented in figure 4.23. The RIN reduction is observed due to increased resonance frequency.

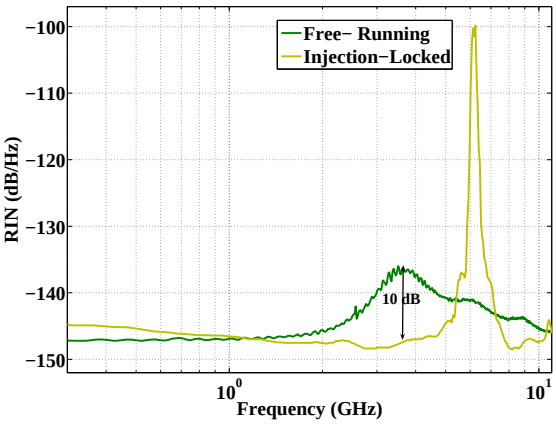

Figure 4.23: Comparison between the free-running and injection-locked 1.5μm RayCan VCSEL RIN spectra.

In other words, the low frequency (1-5 GHz) RIN improves because under the injection-locking influence, the noise peak shifts toward high frequencies, thus removing the effects of high RIN under the normal free-running conditions. The reduction of RIN can be explained qualitatively as well as quantitatively. Qualitatively speaking, under injection-locking conditions, fewer carriers are needed to achieve simultaneous emission and lasing action. The spontaneous emission contribution of the laser is lessened, hence reducing the noise. Mathematically, this phenomenon can be explained as increase in the value of ${P_0}^2$ in the equation 4.7, which has the effect of producing a diminished RIN measurement.

It must be noted however that when the term "RIN improvement using optical injection-locking"is employed, it effectively means the shifting of peak RIN to higher frequencies.

Consequently, the lower frequency bands benefit from this peak shifting and a relative lowered RIN is observed at the lower frequencies. Negative wavelength detuning can be employed to further push the RIN peak to higher frequencies, since negative wavelength detuning results in very high resonance frequencies. On the other hand, negative wavelength detuning produce a sharp, undamped resonance frequency peak, the value of RIN peak at these frequencies is several dBs higher than free-running RIN peak at the same frequency. This phenomenon can be observed in figures4.22 and 4.23.

4.3 Conclusion and Discussion

This chapter presents the injection-locking of fibered single-mode VCSELs. Component packaging is found to be problematic, since it reduces the effective observable bandwidth of the optical module, on the other hand it offers ease of manipulation and helps to avoid the problems related to optical power coupling in single-mode fibers. A procedure to extract the S_{21} response of free-running and injection-locked VCSELs is defined and implemented. This procedures requires the development of mathematical models for VCSELs operating in free-running and injection-locked conditions. Models already developed in [3] and Chapter. 2 are used in conjunction with experimentally obtained values, in order to reconstruct S_{21} response curves for free-running and injection-locked VCSELs.

RIN measurements of free-running and injection-locked VCSELs have been undertaken in order to study the injection-locking effects on RIN curves. An experimental test bench for RIN measurement of injection-locked VCSELs is setup. RIN measurements have allowed the observation of wavelength detuning and injected optical power influence on single-mode 1.55μm VCSELs. A comprehensive comparison of resonance frequency evolution of an injection-locked VCSEL for different wavelength tuning values is presented. The resonance peak shift toward high frequencies helps in achieving RIN improvements of about 10 dB under injection-locking conditions.

Bibliography

[1] J. Cartledge and R. Srinivasan, "Extraction of DFB laser rate equation parameters for system simulation purposes," *Journal of Lightwave Technology*, vol. 15, no. 5, pp. 852–860, May 1997.

[2] Bacou, A. and Hayat, A. and Rissons, A. and Iakovlev, V. and Syrbu, A. and Mollier, J.-C. and Kapon, E., "VCSEL Intrinsic Response Extraction Using T-Matrix Formalism," *IEEE Photonics Technology Letters*, vol. 21, no. 14, pp. 957–959, July15, 2009.

[3] A. Bacou, "Caractérisation et Modélisation optoélectronique de VCSEL à grande longueur d'onde pour sous-ensembles optiques intégrés," Ph.D. dissertation, Institut Supérieur de l'Aéronautique et de l'Espace, 2008.

[4] A. Hayat, A. Bacou, A. Rissons, J.-C. Mollier, V. Iakovlev, A. Syrbu, and E. Kapon, "Long Wavelength VCSEL-by-VCSEL Optical Injection Locking," *Accepted for publication in IEEE Transactions on Microwave Theory and Techniques*, 2009.

[5] ——, "1.3μm single-mode VCSEL-by-VCSEL optical injection-locking for enhanced microwave performance," in *21st Annual Meeting of the IEEE Lasers and Electro-Optics Society,2008. LEOS 2008.*, Nov. 2008, pp. 224–225.

[6] L. Chrostowski, X. Zhao, C. Chang-Hasnian, R. Shau, M. Ortsiefer, and M.-C. Amann, "Very High Resonance Frequency (>40 GHz) Optical Injection-Locked 1.55 μm VCSELs," in *IEEE International Topical Meeting on Microwave Photonics. MWP'04.*, 4-6 Oct. 2004, pp. 255 – 258.

[7] L. Chrostowski, X. Zhao, and C. Chang-Hasnain, "Microwave Performance of Optically Injection-locked VCSELs," *IEEE Transactions on Microwave Theory and Techniques*, vol. 54, no. 2, pp. 788–796, Feb. 2006.

[8] L. Coldren and S. Corzine, *Diode Lasers and Photonic Integrated Circuits*, K. Chang, Ed. John Wiley & Sons. Inc., 1995.

[9] I. Gatare, M. Sciamanna, A. Locquet and K. Panajotov, "Influence of polarization mode competition on the synchronization of two unidirectionally coupled vertical-cavity surface-emitting lasers," *Optics Letters*, vol. 32, pp. 1629–1631 no. 12, 2007.

[10] I. Gatare, M. Sciamanna, A. Locquet and K. Panajotov, "Transverse Mode Switching and Locking in Vertica-Cavity Surface-Emitting Lasers Subject to Orthogonal Injection," *IEEE Photonics Technology Letters*, vol. 43, no. 4, pp. 322–333, 2007.

[11] L. Chrostowski, C.-H. Chang, and C. Chang-Hasnain, "Reduction of Relative Intensity Noise and Improvement of Spur-Free Dynamic Range of an Injection-Locked VCSEL," *The 16th Annual Meeting of the IEEE Lasers and Electro-Optics Society. LEOS 2003.*, vol. 2, pp. 706–707 vol.2, Oct. 2003.

[12] X. Jin and S. L. Chuang, "Relative intensity noise characteristics of injection-locked semiconductor lasers," *Applied Physics Letters*, vol. 77, no. 9, pp. 1250–1252, 2000.

Conclusion and Future Prospects

The research work presented here is carried-out in the context of a trans-national project, in partnership with Ecole Polytechnique Fédérale de Lausanne (EPFL), BeamExpress (an EPFL spin-off) and D-Lightsys, a French company specializing in optical interconnects for harsh environments [2]. The project focus is on conception of optical sub-assemblies for deployment in 10Gbps links using 1.3μm and 1.5μm VCSELs. Three distinct functionalities namely, fabrication, characterization and product development are attributed respectively to EPFL/BeamExpress, MOSE-ISAE and D-Light Sys. Consequently the research work presented here has an emphasis on measurement and instrumentation, characterization and numerical modelling.

The experimental part of this work is unprecedented in nature, in the sense that MOSE laboratory had no tradition of injection-locking experimental research when the project kicked-off in early 2007. Modeling, mathematical as well as electronic, and characterization of VCSELs has however been MOSE's forte since long and therefore the mathematical models presented are an extension of previous free-running VCSEL models to the injection-locked domain [1], [2], [3].

We have presented a comprehensive mathematical model of optically injection-locked VCSELs. Free-running laser rate-equations have been modified to adapt to injection-locking environment. Injection-locked VCSEL frequency response has been simulated under various operating conditions. Three distinct operating regimes, on the basis of increasing and decreasing frequency detuning and increasing injected optical powers have been defined.

The simulations carried-out using the rate-equation based mathematical model are then validated by comparing to experimental results. The experimental data is obtained using both packaged and on-chip VCSELs. While the follower laser used in these experiments has always been a VCSEL, the master lasers have been changed according to the nature of experiment and ease of manipulation. Consequently DFB lasers and external cavity tunable lasers have been used along with VCSELs as master lasers. Resonance frequencies as high as 16 GHz and cut-off frequencies as high as 10 GHz for BeamExpress VCSELs have been presented.

[2]D-Lightsys is now acquired by the microwave and optical component manufacturer **Radiall**.

Although $S-$parameter measurements using on-chip VCSELs allow the observation of parasitics-free S_{21} response, optical injection-locking experiments using packaged VCSELs have also been carried-out. A method for extraction of component S_{21} response from the noisy packaged system response has been developed and applied to RayCan injection-locked VCSELs. This method allows the extraction of component frequency response using S_{21} measurements and a mathematical model.

Relative Intensity Noise (RIN) measurements, of free-running and optically injection-locked VCSELs, have been done in order to compare the influence of injection-locking phenomena on the component noise. The static nature of RIN measurements has allowed the observation of resonance frequency evolution under different injection-locking conditions. A RIN diminution of 10 dB has been presented for injection-locked VCSELs operating under positive frequency detuning regime.

The need for high bandwidths and link gains for faster and more demanding communication systems has led to research in optical injection-locking of semiconductor lasers. Although telecommunication systems appear to be the foremost application of optical injection locking , since it improves both the link linearity [4], [5], [6], [7] and link gain [8], [9], its applications are not limited to the telecommunication realm. One of the many emerging applications of optical injection-locking is millimeter wave generation. Since Goldberg et. al demonstrated microwave signal generation through injection-locking in 1983 [10], many research groups have utilized this technique for millimeter wave generation. Braun et. al have reported the generation of a 64GHz signal in 1998, using the side-band injection-locking [11]. Lately Jin et. al and Sung et. al have also carried out optical injection-locking based millimeter wave generation experiments [12], [13].

One of the biggest future applications of optically injection-locked VCSELs is the all optical signal processing. Although all optical signal processing was tried using injection-locked DFB lasers [14], side-mode injection-locked lasers [15] and a bi-mode injection-locked Fabry-Pérot laser [16], it really took-off after the developments in VCSEL technology. All-optical inverter [17], all-optical format conversion [18] and polarization controllers for all-optical signal processing [19], using optically injection-locked VCSELS have already been presented.

Optical injection-locking can also be used to synchronize incoherent lasers in homodyne and heterodyne systems. Although the synchronization can be achieved using a Phase-Locked Loop (PLL) in the electrical domain, injection-locking can be used to the effect while remaining in the optical domain [20], [21]. Bordonalli et. al have demonstrated the combined use of optical injection-locking and optical phase-locked loop [22]. Optical injection-locking techniques have equally been used for clock recovery up to 80 GHz [23].

Finally, it must be said that although optical injection-locking has proved to be beneficial in many ways, it enhances the system complexity. Injection-locking based applications can gain currency only if they benefit from the low module cost offered by integration and mass-production. The rapid development of VCSELs, which are intrinsically more integrable than their edge-emitting counterparts, is certainly a step in right direction. As novel integration technologies emerge, integration of optically injection-locked VCSELs would offer more and more possibilities of overcoming intrinsic limits of components as well as systems.

Bibliography

[1] A. Rissons, J. Perchoux, and J.-C. Mollier, "Small Signal and Noise Circuit Model of Vertical-Cavity Surface-Emitting Laser (VCSEL) Arrays for Short Range Optomicrowave Links," in *MWP 2003 Proceedings. International Topical Meeting on Microwave Photonics, 2003.*, Sept. 2003, pp. 211–214.

[2] A. Bacou, "Caractérisation et Modélisation optoélectronique de VCSEL à grande longueur d'onde pour sous-ensembles optiques intégrés," Ph.D. dissertation, Institut Supérieur de l'Aéronautique et de l'Espace, 2008.

[3] A. Bacou, A. Hayat, A. Rissons, V. Iakovlev, A. Syrbu, J.-C. Mollier, and E. Kapon, "Electrical Modeling of Long-Wavelength VCSELs for Intrinsic Parameters Extraction," *Submitted to IEEE Journal of Quantum Electronics*, 2009.

[4] I. Cox, C.H., E. Ackerman, G. Betts, and J. Prince, "Limits on the performance of RF-over-fiber links and their impact on device design," *Microwave Theory and Techniques, IEEE Transactions on*, vol. 54, no. 2, pp. 906–920, Feb. 2006.

[5] T. Darcie, R. Tucker, and G. Sullivan, "Intermodulation and harmonic distortion in InGaAsP lasers," *Electronics Letters*, vol. 21, no. 16, pp. 665–666, 1 1985.

[6] L. Chrostowski, C.-H. Chang, and C. Chang-Hasnain, "Enhancement of Dynamic Range in 1.55μm VCSELs Using Injection Locking," *IEEE Photonics Technology Letters*, vol. 15, no. 4, pp. 498–500, April 2003.

[7] X. J. Meng, T. Chau, and M. Wu, "Improved intrinsic dynamic distortions in directly modulated semiconductor lasers by optical injection locking," *Microwave Theory and Techniques, IEEE Transactions on*, vol. 47, no. 7, pp. 1172–1176, Jul 1999.

[8] N. M. Froberg and K. Y. Lau, "Ultrahigh-efficiency Microwave Signal Transmission Using Tandem-Contact Single Quantum Well GaAlAs Lasers," in *Optoelectronic Signal Processing for Phased-Array Antennas II*, vol. 1217, no. 1, 1990, pp. 2–5.

[9] K. J. Vahala, M. A. Newkirk, and T. R. Chen, "The Optical Gain Lever: A Novel Gain Mechanism in the Direct Modulation of Quantum Well Semiconductor Lasers," *Applied Physics Letters*, vol. 54, no. 25, pp. 2506–2508, 1989.

[10] L. Goldberg, H. Taylor, J. Weller, and D. Bloom, "Microwave signal generation with injection-locked laser diodes," *Electronics Letters*, vol. 19, no. 13, pp. 491–493, 23 1983.

[11] R.-P. Braun, G. Grosskopf, D. Rohde, and F. Schmidt, "Low-phase-noise millimeter-wave generation at 64 GHz and data transmission using optical sideband injection locking," *Photonics Technology Letters, IEEE*, vol. 10, no. 5, pp. 728–730, May 1998.

[12] J. Hong and R. Hui, "Tunable millimeter-wave generation with subharmonic injection locking in two-section strongly gain-coupled DFB lasers," *IEEE Photonics Technology Letters*, vol. 12, no. 5, pp. 543–545, May 2000.

[13] H. Kee-Sung, T. Jung, M. Wu, D. Tishinin, K. Liou, and W. Tsang, "Optical generation of millimeter-waves using monolithic sideband injection locking of a two-section DFB laser," *The 16th Annual Meeting of the IEEE Lasers and Electro-Optics Society. LEOS 2003.*, vol. 2, pp. 1005–1006 vol.2, Oct. 2003.

[14] B. K. Mathason and P. J. Delfyett, "Pulsed Injection Locking Dynamics of Passively Mode-Locked External-Cavity Semiconductor Laser Systems for All-Optical Clock Recovery," *J. Lightwave Technol.*, vol. 18, no. 8, p. 1111, 2000. [Online]. Available: http://jlt.osa.org/abstract.cfm?URI=JLT-18-8-1111

[15] A. Kuramoto and S. Yamashita, "All-Optical Regeneration Using a Side-Mode Injection-Locked Semiconductor Laser," *IEEE Journal of Selected Topics in Quantum Electronics*, vol. 9, no. 5, pp. 1283–1287, Sept.-Oct. 2003.

[16] S. Yamashita and J. Suzuki, "All-optical 2R Regeneration using a Two-Mode Injection-Locked Fabry-Perot Laser Diode," *IEEE Photonics Technology Letters*, vol. 16, no. 4, pp. 1176–1178, April 2004.

[17] Y. Onishi, N. Nishiyama, C. Caneau, F. Koyama, and C. en Zah, "Dynamic behavior of an all-optical inverter using transverse-mode switching in 1.55 μm vertical-cavity surface-emitting lasers," *Photonics Technology Letters, IEEE*, vol. 16, no. 5, pp. 1236–1238, May 2004.

[18] H. Kawaguchi, Y. Yamayoshi, and K. Tamura, "All-Optical Format Conversion Using an Ultrafast Polarization Bistable Vertical-Cavity Surface-Emitting Laser," *Lasers and Electro-Optics, 2000. (CLEO 2000). Conference on*, pp. 379–380, 2000.

[19] K. Hasebe, Y. Onishi, and F. Koyama, "Novel polarization controller based on injection-locked vertical-cavity surface-emitting laser," *IEICE Electronics Express*, vol. 2, no. 8, pp. 274–279, 2005.

[20] S. Kobayashi and T. Kimura, "Coherence of Injection Phase-Locked AlGaAs Semiconductor Laser," *Electronics Letters*, vol. 16, no. 17, pp. 668–670, 14 1980.

[21] J. Kahn, "1 Gbit/s PSK homodyne transmission system using phase-locked semiconductor lasers," *Photonics Technology Letters, IEEE*, vol. 1, no. 10, pp. 340–342, Oct 1989.

[22] A. C. Bordonalli, C. Walton, and A. J. Seeds, "High-Performance Phase Locking of Wide Linewidth Semiconductor Lasers by Combined Use of Optical Injection Locking and Optical Phase-Lock Loop," *J. Lightwave Technol.*, vol. 17, no. 2, p. 328, 1999.

[23] H. Kamitsuna, K. Sano, K. Kurishima, and M. Ida, "80 GHz electrical clock extraction from 80 Gbit/s RZ optical data stream using direct optical injection locking of InP/InGaAs HPT oscillator," *Electronics Letters*, vol. 40, no. 2, pp. 139–140, Jan. 2004.

List of Publications

Journal Publications

Ahmad Hayat, Alexandre Bacou, Angélique Rissons, Vladimir Iakovlev, Alexei Syrbu, Jean-Claude Mollier and Elie Kapon, "Long-Wavelength VCSEL by VCSEL Optical Injection-Locking", *IEEE Transactions on Microwave Theory and Techniques*, Accepeted for publication.

Alexandre Bacou, Ahmad Hayat, Angélique Rissons, Vladimir Iakovlev, Alexei Syrbu, Jean-Claude Mollier and Elie Kapon, "Optoelectronic T-Matrix Technique Applied to Efficient Deembedding of Intrinsic 1.3μm VCSEL Dynamic Behavior", *IEEE Photonics Technology Letters*, VOL. 21, No. 14, July 15, 2009.

Alexandre Bacou, Ahmad Hayat, Angélique Rissons, Vladimir Iakovlev, Alexei Syrbu, Jean-Claude Mollier and Elie Kapon, "Electrical Modeling of Long-Wavelength VCSELs for Intrinsic Parameters Extraction", *IEEE Jouranl of Quantum Electronics*, Submitted.

International Conferences

Ahmad Hayat, Alexandre Bacou, Angélique Rissons, Jean-Claude Mollier, "2.49GHz Low Phase-Noise Optoelectronic Oscillator using 1.55μm VCSEL for Avionics and Aerospace Applications", *in Proc. SPIE, vol.6908*, (San Jose, CA, USA), SPIE, Jan. 2009.

Ahmad Hayat, Margarita Varon, Alexandre Bacou, Angélique Rissons, Jean-Claude Mollier, "2.49GHz Low Phase-Noise Optoelectronic Oscillator using 1.55μm VCSEL for Avionics and Aerospace Applications", *in International Topical Meeting on Microwave Photonics, 2008. MWP 2008 Proceedings*, Oct. 2008.

Ahmad Hayat, Alexandre Bacou, Angélique Rissons, Jean-Claude Mollier, Vladimir Iakovlev, Alexei Syrbu and Eli Kapon, "1.3μm Single-Mode VCSEL-by-VCSEL Optical Injection-Locking for Enhanced Microwave Performance", *in The 15th Annual Meeting of the IEEE*

Lasers and Electro-Optics Society, LEOS, 2008.

Book Chapters

Ahmad Hayat, Alexandre Bacou, Angélique RISSONS and Jean-Claude MOLLIER, "Optical Injection-Locking: A Technique for VCSEL Operation Enhancement in "Advances in Lasers and Electro-Optics", ISBN 978-953- 7619-X-X.", Accepted for publication in Novemeber 2009.

Optical Injection-Locking of 1.3μm and 1.5μm VCSELs: Experiments and Modeling

Ahmad HAYAT

March 12, 2010

Contents

List of Figures

List of Tables

Introduction

Ces travaux de recherche ont pour but d'étudier les phénomènes du verrouillage optique dans les VCSELs à grandes longueurs d'onde, pour différent type de VCSELs et sous différents conditions de fonctionnement du composant. Ce travail s'effectue dans le cadre d'un projet Européen, en collaboration avec l'École Polytechnique Fédérale de Lausanne (EPFL), D-Lightsys, un fabriquant de sous-ensembles optiques Français et BeamExpress, une spin-off d'EPFL, fabriquant de VCSELs émettant à 1.3μm et à 1.55μm. La plupart des résultats des expériences de verrouillage optique présentées dans ce mémoire a été obtenue en utilisant les VCSELs de BeamExpress [**?**]. Des VCSELs fabriqués par une société Coréenne, RayCan, ont aussi été testés [**?**]. Un modèle théorique, se basant sur des paramètres intrinsèques des VCSELs émettant à grandes longueurs d'onde, a aussi été développer afin de compléter les travaux de recherche dans le domaine de verrouillage optique des VCSELs.

Le premier chapitre introduit l'évolution historique du verrouillage optique. Ensuite, nous expliquons l'évolution des expériences dans le domaine de verrouillage optique et les techniques utilisées. Le verrouillage optique, dans le contexte des lasers émettant par la tranche conventionnels (EEL) est présenté entraînant le verrouillage optique des VCSELs. Diverses applications du verrouilage optique par rapport à ces différents régimes de fonctionnement ont ensuite présentées. La seconde partie de ce chapitre introduit les diodes lasers VCSELs; ses particularités et les différentes structures en insistant sur les VCSELs émettant aux longueurs d'onde télécoms notamment celle que nous utilisons pour le verrouillage.

Le second chapitre est dédié à la modélisation mathématique des VCSELs optiquement verrouillés. Un modèle, adapté au verrouillage optique, basé sur les équations d'évolution a été présenté. Ce modèle emploie les valeurs des paramètres intrinsèques afin de calculer la réponse fréquenctielle du VCSEL verrouillé. La réponse S_{21} d'un VCSEL verrouillé sous différentes conditions d'injection ainsi que pour différentes valeurs de detuning de fréquence (longueur d'onde) a été présentée. La plage effective de verrouillage par rapport à la puissance optique injectée et au detuning employé est aussi calculée. Une comparaison entre la réponse S_{21} des VCSELs verrouillés et non-verrouillés est ensuite présentée.

Le troisième chapitre présente les résultats des expériences de verrouillage optique des VCSELs émettant à 1.3μm et à 1.5μm. Plusieurs régimes distincts de fonctionnement ont été définis. Finalement une comparaison entre les simulations développées précédemment et

les mesures S_{21} des VCSELs verrouillés est présentée.

Le quatrième chapitre, dans un premier temps, élabore une technique pour l'extraction de réponse S_{21} d'un VCSEL depuis les mesures bruitées. Cette technique est implémentée pour les VCSELs non verrouillés et verrouillés émettant à 1.3μm et à 1.5μm. Ensuite, les mesures de bruit d'intensité des VCSELs ont été effectuées. Nous présentons les mesures de bruit des VCSELs verrouillés et non verrouillés afin d'observer la variation du plancher de bruit et du pic de fréquence de relaxation sous différentes conditions de fonctionnement.

Chapter 1 Verrouillage Optique des VCSELs à 1.3μm et à 1.55μm

1.1 Verrouillage Optique

1.1.1 Introduction et Évolution Historique

La première observation de synchronisation (et donc de verrouillage) entre deux oscillateurs a été mise en évidence par l'éminent mathématicien Hollandais, Christaan Huygens, en 1665. Il a observé que les pendules des deux horloges de sa chambre, se synchronisaient, si les horloges étaient à la proximité l'une près de l'autre. Cette synchronisation se perdait avec l'augmentation de la distance entre les deux horloges. Il a conclu que les perturbation mécanique transférées d'une horloge à l'autre, via le mur, étaient responsables de cette synchronisation. Environ 300 ans après cette démonstration involontaire de verrouillage entre deux oscillateurs mécaniques, en 1946, Adler a publié ses travaux scientifiques, détaillant le verrouillage de deux oscillateurs électroniques.

La première mise en oeuvre de verrouillage optique a dû attendre encore 20 ans. Pantell a publié la théorie de verrouillage optique en 1965, mais c'est Stover et Stier qui ont démontré pour la première fois le verrouillage optique en utilisant deux laser Hélium-Néon, émettant à environ 650nm. Après cette première démonstration, la recherche dans le domaine du verrouillage optique a considérablement ralenti. Cela est dû à plusieurs raisons: les source lasers n'étaient ni très efficaces ni très faciles à manipuler. La communauté scientifique employait alors la majorité de ses ressources intellectuelles pour le développement des sources lasers elle-mêmes mais pas pour l'évolution des applications lasers. Cette situation a changé avec l'arrivée des lasers à semi-conducteur. Ces sources optiques, avec l'invention des fibres optiques, ont révolutionné le domaine des télécommunications et ont déclenché un cycle auto-renforçant, dont la conséquence était une amélioration rapide de la qualité des sources optiques.

La disponibilité des lasers de petite taille et à faible consommation, a relancé les travaux scientifiques dans le domaine du verrouillage optique pendant les année 80s. Kobayashi et Kimura ont fait la première démonstration de verrouilage optique en utilisant deux lasers AlGaAs émettant à 840nm en 1980 [**?**]. En même temps, le verrouillage optique a été utilisé dans plusieurs techniques de détection cohérente. En 1982 Kobayashi et Kasapi ont

présenté les méthodes de modulation de phase et de fréquence d'un signal en utilisant le verrouillage optique [?], [?] . En 1984, Lin et Mengel ont démontré la réduction de chirp d'un laser suiveur verrouillé optiquement [?]. Gallion a présenté, en 1985, la réduction de la largeur de raie d'un laser suiveur en utilisant le verrouillage optique [?]. Olsson a utilisé le phénomène de réduction de chirp d'un laser verrouillé pour atteindre un débit de 2 Gbps pour une longueur de fibre de 82.5 km [?].

Les principaux travaux théoriques ont aussi été fait pendant les années 80. En 1982, Lang a publié la théorie des lasers verrouillés [?]. Kurokawa a publié en 1973 [?], les formules pour calculer la plage de verrouillage des oscillateurs électroniques, mais c'est Lang qui a remarqué l'asymétrie de verrouillage vis-à-vis de désaccrod enre les deux longueurs d'onde (Detuning). Il l'a attribué aux perturbations de l'indice de réfraction du laser liées à l'injection des photons. Henry a détaillé le même concept mathématiquement, en prenant en compte le couplage phase-amplitude [?], en introduisant, actuellement, le très connu facteur d'Henri. L'application principale du verrouillage optique était la détection cohérente: avec l'apparition et le développement de l'EDFA au début et au milieu des années 90s, la détection directe est devenu le moyen préféré de démodulation, concluant momentanément la recherche dans le domaine du verrouillage optiques des lasers.

C'est vers la fin des années 90 que dans un premier temps Simpson [?] puis Meng [?] ont présenté l'augmentation de la bande-passante de modulation et de la fréquence de résonance intrinsèque. En combinant les propriétés de la réduction de largeur de raie et de chirp, le verrouillage optique proposait des très intéressantes possibilités dans le domaine des transmission de données à très haut débit. Malgré toutes ces avancées dans le domaine des télécommunications, le marché de transmission des données à haut débit s'est trouvé saturé au début du 21^{me} siècle. La raison principale était l'absence d'une source optique cohérente peu coûteuse pour déploiement dans les réseaux LAN, MAN et FTTX. En l'absence de cette source, le grand public était privé des bénéfices de la révolution de la fibre optique, qui dépendait des source optiques trop coûteuses pour l'utilisation d'un abonné individuel.

1.2 Lasers à Cavité Verticale Émettant par la Surface: Besoin, Conception et Évolution

1.2.1 Motivation et Historique

Au départ, ce n'était pas le besoin d'une source optique cohérente moins chère qui a motivé la communauté scientifique à développer les lasers à cavité verticale émettant par la surface(VCSELs). Les lasers conventionnels, émettant par la tranche (EELs), à part être relativement chers, engendré d'autre problèmes techniques pendant leur utilisation dans les systèmes de transmission des données. La caractérisation pendant et après la fabrication,

par exemple, de ces lasers n'était pas possible avant la séparation en puces. A cause de la longueur de cavité limitée, l'intégration monolitihic était rendue très difficile tandis que la longueur de la cavité impliquait la génération des modes latéraux insouhaitables. Finalement, il était impossible de fabriquer monolithiquement des barrettes et des matrices des ces lasers en utilisant les technologies existantes. C'était principalement pour donner remédier ces problèmes que Professeur K. Iga de Tokyo University a proposé la fabrication des VCSELs.
Les VCSELs promettaient d'avoir les avantages suivants:

- La caractérisation sous-pointes pendant la fabrication.
- La fabrication d'un grand nombre de composants, en utilisant les procédés complètment monolithique: ce qui réduit la coût final du composant.
- L'émission monomode grâce à une cavité très courte.
- La possibilité de fabrication en matrices et en barrettes.
- Un courant de seuil très faible du à la cavité optique ultra courte.
- La possibilité d'intégration monolithique avec d'autres composants.
- Un faisceau circulaire grâce à la présence d'une cavité optique cylindrique comparer à un faisceau elliptique des EELs.

En 1979, le fonctionnement pulsée d'un tel laser émettant à 1.33μm à 77K, a été démontré par Iga[**?**]. Dix ans plus tard Jewell a présenté un VCSEL émettant à 850nm fonctionnant en continue à température ambiante avec un courant de seuil de 2mA [**?**]. Baba a présenté un VCSEL émettant à 1.3μm et fonctionnant à température ambiante en 1993. Grabherr et son équipe ont présenté un VCSEL de puissance émettant à 960nm en 1996. Ce VCSEL pouvait atteindre un niveau de puissance jusqu'à 20mW. La technologie des VCSELs émettant à 850nm a très vite été maîtrisée et plusieurs société Européennes, Américaines et Asiatiques les fabriquent et les commercialisent pour diverses applications.

Le développement des VCSELs fonctionnant à la longueur d'onde dites "télécommunication" (entre 1.1μm et 1.6μm) a rencontré beaucoup de difficultés techniques. Le problème principal était la dissipation de chaleur dans les VCSELs à grande longueur d'onde qui est dû au choix de matériaux. La zone active des VCSELs à 850nm est composée de couches très fines de GaAs (ce qui correspond à une émission à 850nm). Pour avoir une réflectivité élevée (de l'ordre de 99.9%), les couches de GaAs et GaAlAs sont empilées en dessous et au dessus de la zone active en alternance. C'est la différence entre l'indice de réfraction des couches qui détermine le nombre de couches requises pour une réflectivité demandée. Par exemple, dans le cas de $AlAs$-$Al_{0.1}Ga_{0.9}As$, la différence entre l'indice de réfraction entre deux couche successives est 0.6 [**?**]. Pour une telle différence, seulement 12 couches suffisent

pour obtenir une réflectivité de plus de 99%.

Par contre la zone active des VCSELs à grande longueur d'onde est composée des alliages de $InGaAsP$-InP. La différence entre les indices de réfraction respectifs étant 0.3, il nous faudrait plus de 40 couches pour atteindre un réflectivité de 99%. Cela pose deux problèmes majeurs. Premièrement, la déposition d'un nombre de couches si élevé pose des difficultés techniques. Deuxièmement, l'$InGaAsP$-InP n'ayant pas un coefficient de dissipation thermique très élevé, un nombre élevé de couches a pour conséquence de rechauffer le composant. Ce rechauffement dégrade vite les performances des VCSELs à grande longueur d'onde, en augmentant la courant de seuil, en diminuant la puissance optique émise et en introduisant des non-linéarités imprévues dans le comportement du composant [**?**], [**?**]. A cause du désacorrd de maille, les miroirs de Bragg composés de matériaux $AlAs$-$AlGaAs$, ne peuvent pas être déposés sur une zone active composée de $InGaAsP$-InP.

Plusieurs solutions ont été proposées pour s'affranchir de ce problème, et en conséquence il existe trois différents types de VCSELs fonctionnant à grand longueurs d'onde, employant trois technologies différentes.

1.2.2 VCSELs fabriqués par Vertilas

Le fonctionnement des VCSELs à grandes longueurs d'onde, utlisant la jonction tunnel, a été démontré par Boucart et Jacquet [**?**] en 1999, mais c'était Ortsiefer et al. (société Vertilas))qui ont commencé la production en série des VCSELs émettant à 1.5μm en employant une variante de cette technique [**?**]. La même équipe a démontré le fonctionnement d'un VCSEL monomode à 1.55μm à température ambiante. Le miroir de Bragg inférieur a été remplacé par 2.5 paires de CaF_2-Si, accompagné d'une couche d'or très fine. Cette couche, hormis sa haute réflectivité, fait office d'un dissipateur de chaleur. Vertilas a commercialisé ces VCSELs, en 2002, pour application dans des réseaux 10 Gbps courte-distance.

1.2.3 BeamExpress VCSELs

1.2.3.1 Wafer Fusion

En 1996, Margalit et al. de l'université de Californie à Santa Barbara (UCSB) ont inventé un procédé pour intégrer les miroirs de Bragg à base de $AlAs$-$Al_xGa_{1-x}As$ sur une zone active en InP, malgré les difficultés présentées par le désaccord de maille. Cette procédure a été brevetée sous le nom de "Wafer Fusion" [**?**].

1.2.3.2 Wafer Fusion Localisé

En employant une variante de cette technique de "Wafer Fusion", Kapon et. al de l'Ecole Polytechnique Fédérale de Lausanne (EPFL) et de la société BeamExpress, ont démontré qu'il était possible de fabriquer les différentes parties d'un VCSEL séparément et ensuite les assembler. Le point fort de cette technique est la possibilité de fabrication des VCSELs en série, qui réduit le coût du composant tout en gardant des DBR en $AlAs$-$Al_xGa_{1-x}As$ qui présentaient une meilleur dissipation de chaleur [**?**], [**?**]. La présence d'une jonction tunnel assure le fonctionnement monomode. Un autre facteur qui contribue à la réduction du coût de ces composants est l'utilisation des matériaux $AlAs$-$Al_xGa_{1-x}As$ moins coûteux que des matériaux InP. Une majorité des résultats présenté dans ce manuscrit ont été obtenus en utilisant des VCSELs provenant de BeamExpress.

1.2.4 RayCan VCSELs

RayCan a adopté une approche plutôt directe pour concevoir les VCSELs à grandes longueur d'onde. Ils ont décidé de faire accroître les DBRs en $InAlGaAs$ directement sur une zone active en InP [**?**]. Les VCSELs RayCan, à cause de la présence des miroirs de Bragg en InP, ne sont pas très efficaces à hautes températures [**?**]. Depuis Novembre 2005, RayCan fournit des modules de télécommunication à 10Gbps, en faisant fonctionner quatre VCSELs à 2.5Gbps en parallèle.

1.3 Verrouillage Optique des VCSELs à Grandes Longueurs d'Onde

Les deux problèmes concernant les VCSELs à grandes longueurs d'onde aujourd'hui sont le chirp induit par la modulation directe qui réduit la bande-passante du lien et les fréquences de coupure relativement basses qui empêchent la transmission des débits très élevés. En 2003, la réduction de chirp et l'augmentation de la bande passante des VCSELs, en utilisant les techniques de verrouillage optique, ont été présenté par l'équipe de Professeur Chang-Hasnanin de l'université de Californie à Berkley (UCB) [**?**], [**?**], [**?**], [**?**]. Ils utilisent un laser EEL pour verrouiller un VCSEL ce qui augmente le coût éventuel du banc de mesure. En effet, le verrouillage optique d'un VCSEL par un autre VCSEL identique peut être très intéressant puisque cela va ouvrir les possibilités d'utilisation des systèmes optiquement verrouillées dans les divers projets tels que les réseaux LAN, MAN et FTTX.

Chapter 2 Simulations Numériques des VCSELs Verrouillés

2.1 Équations d'Évolution

La cavité optique d'un laser est un transducteur éléctro-optique, dont le paramètre d'entrée (la densité des électrons) et le paramètre de sortie (la densité des photons) sont liés l'un avec l'autre par les paramètre intrinsèques de la cavité. Les équations d'évolution pour les VCSELs expriment cette relation mathématiquement comme soit:

$$\frac{dN(t)}{dt} = \frac{\eta_i I}{qV_{act}} - (A + BN(t) + CN(t)^2)N(t) - v_g G S(t) \tag{2.1}$$

$$\frac{dS(t)}{dt} = \Gamma\beta BN(t)^2 + \Gamma v_g G S(t) - \frac{S(t)}{\tau_P} \tag{2.2}$$

Où $N(t)$ et $S(t)$ sont les densités des électrons et des photons , η_i le rendement quantique interne, q la charge d'un électron, V_{act} le volume de la zone active, v_g le vitesse de groupe, β le coefficient d'émission spontanée, Γ le facteur de confinement et τ_P la durée de vie des photons.

Le taux d'émission spontanée, R_{sp} peut être défini par les coefficients A, B et C ou A represente le coefficient de Shockley-Read-Hall relatif aux recombinaisons non-radiatives, B, le coefficient de recombinaison bimoléculaire et C, le coefficient relatif à l'effet d'Auger.

Le gain G est exprimé par

$$G = a_0 \frac{N(t) - N_{tr}}{1 + \epsilon S(t)} \tag{2.3}$$

où N_{tr} est la densité des porteurs à la transparence, a_0, le coefficient de gain différentiel et ϵ, le facteur de compression de gain.

Une troisième équation décrivant le comportement de phase du composant peut être introduit de la façon suivante:

$$\frac{d\phi(t)}{dt} = \frac{\alpha_H \Gamma v_g a_0}{2}(N(t) - N_{tr}) \tag{2.4}$$

α_H est le facteur de couplage "Phase-Amplitude" connu aussi comme le "Facteur d'Henry ".

Quand la puissance optique émise par le laser maître est injectée dans la cavité du laser suiveur, les équations sont modifiées de la façon suivante:

$$\frac{dN(t)}{dt} = \frac{\eta I}{qV_{act}} - (A + BN(t) + CN(t)^2)N(t) - v_g GS(t) \tag{2.5}$$

$$\frac{dS(t)}{dt} = \Gamma v_g GS(t) - \frac{S(t)}{\tau_P} + \frac{v_g}{L}\sqrt{S(t)S_{inj}}\cos(\theta) + \Gamma B\beta N(t)^2 \tag{2.6}$$

$$\frac{d\phi(t)}{dt} = \frac{\alpha_H \Gamma v_g a_0}{2}(N(t) - N_{tr}) - \Delta\omega - \frac{v_g}{2L}\sqrt{\frac{S_{inj}}{S(t)}}\sin(\theta) \tag{2.7}$$

Deux paramètres très importants, quantifiant les phénomènes de verrouillage, S_{inj} et θ, sont rajoutés aux équations 2.6 et 2.7. S_{inj} représente la densité des photons injectés dans la cavité du VCSEL suiveur et θ représente la différence de phase entre les champs optiques du laser maître et du laser suiveur:

$$\theta = \phi_{inj} - \phi(t) \tag{2.8}$$

Un autre paramètre important est $\Delta\omega$ ou le "Detuning en Fréquence". On peut le définir comme:

$$\Delta\omega = \omega_{Master} - \omega_{Follower} \tag{2.9}$$

En plus des trois paramètres décrits ci-dessus, le quatrième paramètre intervenant est le "coefficient de couplage". Il est nommé k_c et peut être défini par:

$$k_c = \frac{v_g}{2L} \tag{2.10}$$

L étant la longueur de la cavité optique.

2.2 Analyse Petit Signal

$$\frac{dN(t)}{dt} = \frac{\eta_i I}{qV_{act}} - (A + BN(t) + CN(t)^2)N(t) - v_g GS(t) \tag{2.11}$$

$$\frac{dS(t)}{dt} = \Gamma v_g GS(t) - \frac{S(t)}{\tau_P} + \frac{v_g}{L}\sqrt{S(t)S_{inj}}\cos(\theta) + \Gamma B\beta N(t)^2 \tag{2.12}$$

$$\frac{d\phi(t)}{dt} = \frac{\alpha_H \Gamma v_g a_0}{2}(N(t) - N_{tr}) - \Delta\omega - \frac{v_g}{2L}\sqrt{\frac{S_{inj}}{S(t)}}\sin(\theta) \tag{2.13}$$

Considérons qu'un signal sinusoïdal $\Delta I e^{j\omega t}$ module un VCSEL polarisé par un courant continu $\overline{I}$. L'expression finale du courant I devient donc:

$$I(t) = \overline{I} + \Delta I e^{j\omega t} \tag{2.14}$$

Ainsi les variations des porteur, des photons et de la phase peuvent être exprimées comme:

$$N(t) = \overline{N} + \Delta N e^{j\omega t} \tag{2.15}$$
$$S(t) = \overline{S} + \Delta S e^{j\omega t} \tag{2.16}$$
$$\phi(t) = \overline{\phi} + \Delta \phi e^{j\omega t} \tag{2.17}$$

En posant

$$\dot{N} = \frac{dN}{dt} \tag{2.18}$$
$$\dot{S} = \frac{dS}{dt} \tag{2.19}$$
$$\dot{\phi} = \frac{d\phi}{dt} \tag{2.20}$$

On a

$$\Delta\dot{N}(I,N,S) = \frac{\partial \dot{N}}{\partial I}\cdot\Delta I + \frac{\partial \dot{N}}{\partial N}\cdot\Delta N + \frac{\partial \dot{N}}{\partial S}\cdot\Delta S \tag{2.21}$$
$$\Delta\dot{S}(N,S,\phi) = \frac{\partial \dot{S}}{\partial N}\cdot\Delta N + \frac{\partial \dot{S}}{\partial S}\cdot\Delta S + \frac{\partial \dot{N}}{\partial \phi}\cdot\Delta\phi \tag{2.22}$$
$$\Delta\dot{\phi}(N,S,\phi) = \frac{\partial \dot{\phi}}{\partial N}\cdot\Delta N + \frac{\partial \dot{\phi}}{\partial S}\cdot\Delta S + \frac{\partial \dot{\phi}}{\partial \phi}\cdot\Delta\phi \tag{2.23}$$

Le gain, comme définit dans l'équation (2.3), contient les termes en fonction des photons ainsi que des porteurs. La dérivé partielle par rapport au densités des porteurs et des photons N et S, donne deux nouvelles variables G_N et G_S, ou G_N et G_S sont définis par:

$$G_N = \frac{\partial G}{\partial N} = \frac{a_0}{1+\epsilon S} \tag{2.24}$$
$$G_S = -\frac{\partial G}{\partial S} = \frac{a_0\epsilon(N-N_{tr})}{(1+\epsilon S)^2} \tag{2.25}$$

Prendre la dérivée partielle de l'équation (2.5) , par rapport à N, S et ϕ, donne les trois équations suivantes:

$$\frac{\partial \dot{N}}{\partial N} \cdot \Delta N = (-(A + 2BN + 3CN^2) - v_g G_N S)\Delta N \quad (2.26)$$

$$\frac{\partial \dot{N}}{\partial S} \cdot \Delta S = (-v_g G + v_g G_S S)\Delta S \quad (2.27)$$

$$\frac{\partial \dot{N}}{\partial I} \cdot \Delta I = \frac{\eta_i}{qV_{act}}\Delta I \quad (2.28)$$

En posant:

$$\rho = \frac{v_g}{2L}\sqrt{\frac{S_{inj}}{S}} \quad (2.29)$$

et en dérivant équation (2.6) par rapport à N, S and ϕ, nous obtenons les trois équations suivantes:

$$\frac{\partial \dot{S}}{\partial N} \cdot \Delta N = (\Gamma v_g G_N S - 2\beta BN)\Delta N \quad (2.30)$$

$$\frac{\partial \dot{S}}{\partial S} \cdot \Delta S = (-\Gamma v_g G_S S + \rho cos(\theta))\Delta S \quad (2.31)$$

$$\frac{\partial \dot{S}}{\partial \phi} \cdot \Delta \phi = (-2 \cdot \rho S sin(\theta))\Delta \phi \quad (2.32)$$

En suivant la même démarche pour l'équation (2.7), cela donne:

$$\frac{\partial \dot{\phi}}{\partial N} \cdot \Delta N = \frac{\alpha_H \Gamma v_g a_0}{2}\Delta N \quad (2.33)$$

$$\frac{\partial \dot{\phi}}{\partial S} \cdot \Delta S = \frac{\rho sin(\theta)}{2S}\Delta S \quad (2.34)$$

$$\frac{\partial \dot{\phi}}{\partial \phi} \cdot \Delta \phi = -\rho cos(\theta)\Delta \phi \quad (2.35)$$

Les équations d'évolutions linéarisées peuvent être exprimées de la manière suivante:

$$\Delta \dot{N} = \frac{\eta_i}{qV_{act}}\Delta I - \big(A + 2BN + 3CN^2 + v_g G_N S\big)\Delta N - \big(v_g G - v_g G_S S\big)\Delta S \quad (2.36)$$

$$\Delta \dot{S} = \big(\Gamma v_g G_N S - 2\beta BN\big)\Delta N - \big(\Gamma v_g G S - \rho cos(\theta)\big)\Delta S - \big(2 \cdot \rho S sin(\theta)\big)\Delta \phi \quad (2.37)$$

$$\Delta \dot{\phi} = \big(\frac{\alpha_H \Gamma v_g a_0}{2}\big)\Delta N + \big(\frac{\rho sin(\theta)}{2S}\big)\Delta S - \big(\rho cos(\theta)\big)\Delta \phi \quad (2.38)$$

En remplaçant les dérivées partielles par les variables intermédiaires, les équations deviennent

$$\Delta\dot{N} = \frac{\eta_i}{qV_{act}}\Delta I - \gamma_{NN}\Delta N - \gamma_{NS}\Delta S \tag{2.39}$$

$$\Delta\dot{S} = \gamma_{SN}\Delta N - \gamma_{SS}\Delta S - \gamma_{S\Phi}\Delta\phi \tag{2.40}$$

$$\Delta\dot{\phi} = \gamma_{\Phi N}\Delta N + \gamma_{\Phi S}\Delta S - \gamma_{\Phi\Phi}\Delta\phi \tag{2.41}$$

Ce système peut alors être exprimé sous la forme matricielle suivante:

$$\frac{d}{dt}\begin{bmatrix}\Delta S\\ \Delta N\\ \Delta\Phi\end{bmatrix} = \begin{bmatrix}-\gamma_{SS} & \gamma_{SN} & -\gamma_{S\Phi}\\ -\gamma_{NS} & -\gamma_{NN} & \gamma_{N\Phi}\\ \gamma_{\Phi N} & \gamma_{\Phi S} & -\gamma_{\Phi\Phi}\end{bmatrix}\cdot\begin{bmatrix}\Delta S\\ \Delta N\\ \Delta\Phi\end{bmatrix} + \frac{\eta_i}{qV_{act}}\cdot\begin{bmatrix}0\\ \Delta I\\ 0\end{bmatrix} \tag{2.42}$$

La transformée de Laplace de ce système d'équation donne

$$\begin{bmatrix}\gamma_{SS}+j\omega & -\gamma_{SN} & \gamma_{S\Phi}\\ \gamma_{NS} & \gamma_{NN}+j\omega & 0\\ -\gamma_{\Phi S} & -\gamma_{\Phi N} & \gamma_{\Phi\Phi}+j\omega\end{bmatrix}\cdot\begin{bmatrix}\Delta\widetilde{S}\\ \Delta\widetilde{N}\\ \Delta\widetilde{\Phi}\end{bmatrix} = \frac{\eta_i\widetilde{I}}{V_{act}}\cdot\begin{bmatrix}0\\ 1\\ 0\end{bmatrix} \tag{2.43}$$

La première étape de la résolution du système consiste à calculer le déterminant:

$$\Lambda = \begin{vmatrix}\gamma_{SS}+j\omega & -\gamma_{SN} & \gamma_{S\Phi}\\ \gamma_{NS} & \gamma_{NN}+j\omega & 0\\ -\gamma_{\Phi S} & -\gamma_{\Phi N} & \gamma_{\Phi\Phi}+j\omega\end{vmatrix} \tag{2.44}$$

soit

$$\begin{aligned}\Lambda = &-j\omega^3\\ &-\omega^2\left(\gamma_{NN}+\gamma_{SS}+\gamma_{\Phi\Phi}\right)\\ &+j\omega\left(\gamma_{S\Phi}\gamma_{\Phi S}+\gamma_{SS}\gamma_{NN}+\gamma_{NS}\gamma_{SN}+\gamma_{NN}\gamma_{\Phi\Phi}+\gamma_{SS}\gamma_{\Phi\Phi}\right)\\ &+\left(\gamma_{S\Phi}\gamma_{\Phi S}\gamma_{NN}-\gamma_{S\Phi}\gamma_{NS}\gamma_{\Phi N}+\gamma_{SS}\gamma_{NN}\gamma_{\Phi\Phi}+\gamma_{SN}\gamma_{NS}\gamma_{\Phi\Phi}\right)\end{aligned} \tag{2.45}$$

En appliquant la méthode de Krammer, la variation des densités de photons peut être exprimée de la façon suivante

$$\Delta\widetilde{S} = \frac{\eta_i\widetilde{I}}{qV_{act}}\cdot\frac{\begin{vmatrix}0 & -\gamma_{SN} & \gamma_{S\Phi}\\ 1 & \gamma_{NN}+j\omega & 0\\ 0 & -\gamma_{\Phi N} & \gamma_{\Phi\Phi}+j\omega\end{vmatrix}}{\Lambda} \tag{2.46}$$

Simplifier l'équation 2.46 entraîne

$$\Delta\widetilde{S} = \frac{\eta_i \widetilde{I}}{qV_{act}} \cdot \frac{(\gamma_{SN}\gamma_{\Phi\Phi} - \gamma_{\Phi N}\gamma_{N\Phi}) + j\omega\gamma_{SN}}{\Lambda} \tag{2.47}$$

la résolution des équations 2.6 et 2.7 permet d'aboutir à la relation suivante:

$$\theta = \sin^{-1}\left[\frac{\Delta\omega}{k_c\sqrt{\frac{S_{inj}}{S}}\sqrt{1+\alpha_H^2}} + \tan^{-1}\alpha_H\right] \tag{2.48}$$

En utilisant l'équation 2.48, on peut injecter les effets du detuning dans le modèle petit signal d'un système verrouillé, puisque $\gamma_{\Phi\Phi}$, $\gamma_{\Phi S}$, $\gamma_{S\Phi}$ and γ_{SS} dependent de θ.

2.3 Résultats des Simulations Numériques

Le modèle mathématique proposé précédemment est implémenté en utilisant MATLAB afin d'observer la réponse petit signal d'un système verrouillé. Les paramètres intrinsèques utilisés pour simuler les VCSELs verrouillés proviennent de [**?**].

La réponse petit-signal d'un VCSEL verrouillé peut avoir trois profils différents:

- Fréquence de résonance élevée , Band-Passante faible
- Fréquence de résonance élevée , Band-Passante élevée
- Fréquence de résonance basse, Band-Passante faible

2.3.0.1 Fréquence de résonance élevée , Band-Passante faible

Une réponse de ce type peut être obtenue en maintenant la différence entre la fréquence du laser maître et la fréquence du laser suiveur positive. Les figures 2.1 et 2.2 présentent la réponse du S_{21} simulée d'un VCSEL verrouillé, fonctionnant en régime du detuning positif. Ces figures confirment l'augmentation de la fréquence de résonance du VCSEL suiveur augmente avec l'augmentation de la différence de fréquence d'opération entre les deux lasers.

Figure 2.1: Réponse S_{21} calculée d'un VCSEL optiquement verrouillé, fonctionnant en régime de detuning positif.

Figure 2.2: Réponse S_{21} calculée d'un VCSEL optiquement verrouillé, fonctionnant en régime de detuning positif. La fréquence de résonance augmente avec l'augmentation de detuning.

2.3.0.2 Fréquence de résonance élevée , Band-Passante élevée

En maintenant la différence entre les fréquences de fonctionnement des deux lasers près de zéro, on peut obtenir les bande-passantes ainsi que des fréquences de résonances très élevées. La figure 2.3 présente la réponse S_{21} calculée d'un VCSEL fonctionnant en régime de detuning nul. Comme l'indique la figure 2.3 la fréquence de résonance du VCSEL suiveur peut dépasser 20 GHz lorsque l'on fait tendre le detuning vers zéro.

Figure 2.3: Réponse S_{21} simulée d'un VCSEL verrouillé démontrant l'augmentation de la bande-passante pour un detuning nul .

2.3.0.3 Fréquence de résonance basse, Bande-Passante faible

Le troisième régime de fonctionnement est défini par le detuning négatif. C'est à dire que la fréquence du laser suiveur est plus importante que celle du laser maître. La figure 2.4 présente une famille de courbes S_{21} simulées. D'après la figure, il apparaît clairement que la fréquence de résonance augmente lorsque le detuning augmente.

Figure 2.4: Réponse S_{21} simulée d'un VCSEL verrouillé optiquement fonctionnant en régime de detuning négatif.

2.4 Conclusion and Discussion

Un modèle mathématique, basé sur les équations d'évolution modifiées pour le verrouillage optique a été présenté. Les paramètres intrinsèques d'un VCSEL sont utilisés pour calculer la réponse S_{21} d'un VCSEL verrouillé. Trois régimes de fonctionnement ont été définis selon le désaccord entre les fréquences de fonctionnement des lasers maîtres et suiveurs. Les simulations d'un VCSEL verrouillé fonctionnant dans les trois régimes ont été présentées. La comparaison de ces simulations avec l'expérience sera présentée dans le chapitre suivant.

Chapter 3 Expériences Verrouillage Optique

Les résultats des expériences de verrouillage optique présentés ici ont été obtenus en travaillant avec trois différents types de VCSELs. Les VCSELs de la société Vertilas émettant à 1.55μm sont fibrés et ont un spectre d'émission monomode. Les VCSELs provenant de la société BeamExpress et de la société RayCan émettent à 1.3μm et à 1.55μm, et sont en puce. Ces VCSELs aussi ont un spectre d'émission monomode.

3.1 Expériences avec les VCSELs Vertilas

Figure 3.1: Banc de mesure utilisé pour le verrouillage optique des VCSELs Vertilas émettant à 1.55μm.

Le banc de mesure employé pour ces expériences est présenté dans la figure 3.1. La puissance optique émise du laser maître est injectée dans la cavité optique du laser suiveur en utilisant un circulateur optique. L'isolation entre le port 1 et le port 2 de cet isolateur à maintien de polarisation est de plus de 40 dB. Le laser suiveur est dans un boîtier TO-46 dont la fréquence de coupure est à peu près de 5 GHz. La fréquence de coupure intrinsèque des VCSELs Vertilas est approximatievement de 11 GHz. A cause de la fréquence de coupure du boîtier, qui est inférieure à celle du composant, il est impossible d'observer la réponse dynamique de ce VCSEL. Le VCSEL suiveur n'a donc pas été modulé. Le verrouillage optique de ce VCSEL, fonctionnant en régime statique, nous a permis de démontrer la suppression des modes satellites sous verrouillage.

La figure 3.2 présente les spectre optique du VCSEL suiveur verrouillé. Le verrouillage optique due mode fondamentale supprime le mode satellite (dont le niveau de puissance est inférieur à 35 dB de celui du mode fondamental) et le verrouillage du mode satellite a pour conséquence de disparaître le mode fondamental. Ceci montre que sous verrouillage, la cavité optique suiveur ne lase pas sur sa propre fréquence de résonance intrinsèque mais suit la fréquence du laser maître.

(a)\(b)

Figure 3.2: (a) Spectre optique d'un VCSEL Vertilas verrouillé. (Le verrouilage du mode fondamentale supprime le mode satellite).(b) Spectre optique d'un VCSEL Vertilas verrouillé. (Le verrouilage du mode satellite supprime le mode fondamentale). Noter le positionnement des modes supprimés selon les deux différents cas.

3.1.1 Expériences avec les VCSELs de BeamExpress

Afin d'observer la réponse dynamique (la réponse S_{21}) de VCSELs verrouillés, il a été décidé d'utiliser des VCSELs en puce. Cela permet de s'affranchir des problèmes liés aux éléments parasites. La disponibilité des VCSELs provenant du même wafer a permis d'observer les phénomènes de verrouillage VCSEL-par-VCSEL. Le verrouillage optique de VCSELs en puce a présenté beaucoup de possibilités intéressantes mais cela a aussi engendré des difficultés pour la manipulation des composants, surtout lors de l'injection de la puissance optique émise par le VCSEL dans une fibre monomode dénudée a été assez difficile. Le banc de mesure utilisé pour ces expériences est similaire conceptuellement à celui présenté précédemment comme l'indique la figure 3.3.

Pour faire varier la puissance optique émise du laser maître, tout en gardant la longueur d'onde d'émission constante, un amplificateur optique à semi-conduteur a été utilisé. Les VCSELs utilisés émettent à une longueur d'onde de 1.3μm et proviennent du même wafer. Un analyseur de réseau vectoriel est utilisé pour modulé le VCSEL suiveur et observer sa réponse S_{21} sous verrouillage simultanément.

Figure 3.3: Le banc de mesure pour les expériences du verrouillage optique utilisant les VCSEL de la société Vertilas.

3.1.2 Résultats du Verrouillage Optique des VCSELs de BeamExpress

Les trois régimes de fonctionnement définis dans le chapitre précédent ont été identifiés lors de ces expériences. Ces trois régimes sont:

- Fréquence de résonance élevée , Bande-Passante élevée
- Fréquence de résonance basse, Bande-Passante faible
- Fréquence de résonance élevée, Bande-Passante faible

3.1.2.1 Fréquence de résonance élevée , Bande-Passante élevée

La figure 3.4 présente la comparaison de la réponse S_{21} d'un VCSEL suiveur verrouillé optiquement dans un régime de detuning négatif avec sa réponse non-verrouillée. En gardant les fréquences d'émission des lasers très proches l'une de l'autre, on peut obtenir les courbes amorties ayant des fréquences de coupure supérieures à celle du VCSEL non verrouillé. Dans ce cas particulier, la fréquence de coupure est multipliée par 3 avec le verrouillage. Si l'amplitude de la puissance optique injectée dans la cavité optique du laser suiveur augmente, la fréquence de coupure augmente. La figure 3.5 présente ce phénomène. La réponse du même VCSEL fonctionnant dans le régime non-verrouillé (dit "Free-Running") est aussi présentée pour comparaison.

Figure 3.4: Réponse S_{21} d'un VCSEL verrouillé BeamExpress émettant à 1.3μm. Ce VCSEL est verrouillé dans le régime detuning négatif.

Figure 3.5: Réponse S_{21} d'un VCSEL verrouillé BeamExpress émettant à 1.3μm. La famille de courbes S_{21} est obtenue tel que $P_1 > P_2 > P_3 > P_4$.

3.1.2.2 Fréquence de résonance basse, Band-Passante faible

Figure 3.6: Réponse S_{21} d'un VCSEL verrouillé BeamExpress émettant à 1.3μm. Ce VCSEL est verrouillé dans le régime de detuning positif.

Ce fonctionnement correspond à un VCSEL verrouillé dans le régime de detuning positif, comme le met en évidence la figure 3.6. Ce mode de fonctionnement a pour conséquence de réduire la fréquence de résonance et donc la bande-passante.

3.1.2.3 Fréquence de résonance élevée, Bande-Passante faible

Ce fonctionnement correspond à un VCSEL verrouillé dans le régime de detuning positif. Le battement des fréquence dans la cavité optique du laser suiveur a pour conséquence de générer les pics de résonance des fréquences très élevées. Mais en même temps, la réponse S_{21} du VCSEL suiveur subit des chutes à basses fréquences qui réduisent la bande-passante en gardant la fréquence de résonance très élevée. La figure. 3.7 présente la réponse S_{21} d'un VCSEL verrouillé fonctionnant en régime de detuning positif pour laquelle on peut observer une vallée à basse fréquence, limitant la bande-passante de ce VCSEL.

Figure 3.7: Réponse S_{21} d'un VCSEL verrouillé BeamExpress émettant à 1.3μm. Ce VCSEL est verrouillé dans le régime de detuning positif.

3.1.3 Expéreinces avec les VCSELs RayCan

Les VCSELs fabriqués par la société RayCan ne sont pas les VCSELs en puce strictement parlant. Ils sont, en fait, des VCSELs émettant par la surface inférieure à la zone active. Il est donc impossible de les tester sous-pointes. A notre demande, RayCan les a monté sur un microcircuit d'alimentation, qu'ils avaient développé pour intégrer les photodiodes dans les systèmes optiques et qui correspondait presque parfaitement à la taille des pointes utilisées dans notre laboratoire. De plus, il a été décidé d'utiliser les VCSELs fibrés RayCan pour le laser maître pour éviter les problèmes liés au couplage optique. Un VCSEL Raycan monté sur le microcircuit d'alimentation est présenté schématiquement dans la figure 3.8.

Figure 3.8: 1.3μm RayCan VCSEL avec le microcircuit d'alimentation.

Malheureusement, ce circuit d'alimentation avait ses propres limitations limitant l'observation des réponses S_{21} des VCSELs optiquement verrouillés à très hautes fréquences. En plus la présence de gap d'air dans la structure de ces VCSELs a pour effet de diminuer la fréquence de résonance. C'est pour cette raison que le module 10 Gbps RayCan utilise quatre VCSELs en parallèle au lieu d'utiliser un seul VCSEL comme Vertilas.

Figure 3.9: Réponse S_{21} d'un VCSEL RayCan émettant à 1.3μm verrouillé dans le régime de detuning positif.

Les réponses S_{21}, en travaillant avec les VCSELs Raycan en puce sont présentées dans les figures 3.9 et 3.10.

Ces courbes ont la même allure que celles présentées précédemment.

3.2 Comparaison Simulations Mesures

Ce parapgraphe présente la comparaison entre les réponses S_{21} simulées et mesurées des VCSELs BeamExpress uniquement, pour deux raisons:

- Dans le cadre d'un partenariat avec cette société nous avons accès à certains paramètres intrinsèques utiles pour la simulation.

- La structure en puce à accès coplanaire direct permet la minimisation des parasites électriques dans la mesure.

Figure 3.10: Réponse S_{21} d'un VCSEL RayCan émettant à 1.3μm verrouillé dans le régime de detuning négatif.

Le désaccord a basse fréquence, entre les mesures et les simulations, dans les figures 3.11 et 3.12, semble être dû aux problèmes liés à l'injection de la puissance optique. Probablement, les très faibles niveaux de puissance optique couplée entraînent la perte de contrôle de polarisation qui change le profil des courbes S_{21} aux basses fréquences.

Figure 3.11: Comparaison entre les réponses S_{21} mesurées et simulées de VCSEL BeamExpress émettant 1.3μm verrouillés optiquement.

Figure 3.12: Comparison between the experimental and simulated S_{21} response of an optically injection-locked BeamExpress VCSEL emitting at 1.3μm.

3.3 Conclusion

Dans ce chapitre, les effets du verrouillage sur les réponses S_{21} ont été mis en évidence pour trois type VCSEL (Vertilas, BeamExpress et RayCan). Une comparaison entre la mesure et la simulation des VCSELs BeamExpress a permis de valider en partie le modèle à haute fréquence.

Figure 3.13: Comparison between the experimental and simulated S_{21} response of an optically injection-locked BeamExpress VCSEL emitting at 1.3μm.

Chapter 4 Extraction de Réponse S_{21} et les Mesures de RIN

On présente l'extraction de la réponse dynamique intrinsèque des VCSELs (non-verrouillé et verrouillé) fibrés en utilisant le modèle mathématique développé dans les chapitres précédents. Ensuite, les mesures de bruit d'intensité (dit "Relative Intensity Noise (RIN)") des VCSELs verrouillés et non verrouillés sont présentées afin d'observer l'évolution de la fréquence de résonance intrinsèque en fonction de certains paramètres.

4.1 Extraction de la Réponse S_{21}

La modulation directe d'un VCSEL en boîtier donne une réponse dynamique bruitée à cause de la présence des parasites de la ligne de transmission. Ces parasites peuvent être retranchés des mesures pour extraire la réponse intrinsèque du composant à l'aide d'un modèle mathématique [**?**]. La procédure d'extraction est la suivante:

- Soustraire la réponse S_{21} obtenue en polarisant le VCSEL au seuil des réponses S_{21} obtenues en polarisant le VCSEL très au dessus de seuil. Pour éliminer les contributions des parasites électriques de la réponse intrinsèque et montre la variation de la réponse par rapport à la variation de courant de polarisation.

- La même procédure est répétée pour les courbes obtenues en utilisant un modèle mathématique.

- Les courbes expérimentales sont ajustées aux courbes calculées en faisant varier les valeurs des paramètres du modèle mathématique.

- Les courbes S_{21} sont reconstruites en utilisant les valeurs d'ajustement.

Les paramètres intrinsèques utilisés pour simuler un VCSEL proviennent de [**?**]. La figure 4.1 présente les réponses S_{21} calculées pour plusieurs courants de polarisation. Les VCSELs utilisés dans ces expériences sont les VCSELs RayCan fibrés émettant à 1.3μm et à 1.5μm. La réponse expérimentale S_{21} pour les VCSELs émettant à 1.3μm sont présentées dans la figure 4.2. A cause des parasites de boîtier les courbes sont bruitées et la fréquence de coupure est réduite à 4GHz.

Figure 4.1: Réponse S_{21} du VCSEL émettant à 1.3μm calculée pour plusieurs courants de polarisation.

Figure 4.2: Réponse S_{21} du VCSEL émettant à 1.3μm expérimentale pour plusieurs courants de polarisation.

Les figures 4.3 et 4.4 présentent des courbes soustraites expérimentales et calculées respectivement.

La figure 4.5 présente la comparaison entre les courbes soustraites expérimentales et les courbes calculées. La courbe ajustée est aussi présentée dans la même figure. Elle se superpose bien à la courbe mesurée.

Les figures 4.6, et 4.8 présentent les réponses extraites pour les VCSELs émettant à 1.3μm, à 1.5μm et pour les VCSELs verrouillés émettant à 1.5μm.

La figure 4.8 montre que la fréquence de résonance augmente avec l'augmentation de l'amplitude de la puissance optique injectée. Cependant, cette augmentation étant très faible (le laser maître est un VCSEL identique émettant à 1.5μm) la fréquence de résonance n'est pas très élevée.

Figure 4.3: Réponse expérimentale soutraite S_{21} du VCSEL émettant à 1.3μm pour plusieurs courants de polarisation.

Figure 4.4: Réponse calculée soustraite S_{21} du VCSEL émettant à 1.3μm pour plusieurs courants de polarisation.

Figure 4.5: Comparaison entre les réponses S_{21} soustraites mesurées, calculées et ajustées pour un courant de polarisation de 8mA. Le VCSEL émet à 1.3μm.

4.2 Mesures de RIN

Le rapport signal sur bruit d'un laser peut être défini comme [**?**]:

$$SNR = \frac{\langle {i_S}^2 \rangle}{\langle {i_N}^2 \rangle} \tag{4.1}$$

où $\langle i_S \rangle$ et $\langle i_N \rangle$ sont les moyennes des carrés des courant de signal et de bruit. En remplaçant les valeurs de $\langle i_S \rangle$ et $\langle i_N \rangle$ dans l'équation 4.1 pour un signal modulé, on en déduit:

$$SNR = \frac{\langle (P_1 sin\omega t)^2 \rangle}{\langle \delta P(t)^2 \rangle} = \frac{m^2}{2} \frac{{P_0}^2}{\langle \delta P(t)^2 \rangle} \tag{4.2}$$

m est l'indice de modulation et peut être défini comme $m = P_1/P_0$. La figure 4.9 présente le concept de RIN graphiquement. Le RIN peut être exprimé par la relation suivante:

$$RIN = \frac{\langle \delta P(t)^2 \rangle}{{P_0}^2} \tag{4.3}$$

où $\langle \delta P(t)^2 \rangle$ est la moyenne du carré qui suit la loi de distribution normale. L'expression de RIN en dB est:

$$RIN_{dB} = 10 \cdot log_{10} \frac{\langle \delta P(t)^2 \rangle}{{P_0}^2} \tag{4.4}$$

La figure 4.10 présente le banc de mesure utilisé pour effectuer les mesures de RIN.
Le RIN d'une diode laser est calculé en utilisant l'expression mathématique suivante:

$$RIN = \frac{\frac{P_{Obs} - P_{Analyzer}}{G} - 2qI_{PD}R_{Load}}{{I_{PD}}^2 R_{Load}} \tag{4.5}$$

où,

Figure 4.6: Les courbes S_{21} reconstruites en utilisant les paramètres d'ajustement d'un VCSEL émettant à 1.3μm.

Figure 4.7: Les courbes S_{21} reconstruites en utilisant les paramètres d'ajustement d'un VCSEL émettant à 1.55μm.

Figure 4.8: Les courbes S_{21} reconstruites en utilisant les paramètres d'ajustement d'un VCSEL émettant à 1.55μm. Le detuning est fixé à 10GHz.

- P_{Obs} est la puissance optique observée sur l'analyseur de spectre électrique
- $P_{Analyzer}$ est le plancher de bruit de l'analyseur
- R_{Load} est la résistance de charge de l'analyseur
- I_{PD} est le courant photo-détecté
- G est le gain transimpédance
- q est la charge d'électron

Les mesures de RIN d'un VCSEL non-verrouillé RayCan à 1.55μm sont présentés dans la figure 4.11.

La figure 4.12 présente le banc de mesure employé pour les mesures de RIN des VCSELs verrouillés. Ce banc de mesure est une combinaison des deux bancs, présenté précédemment et utilisés pour les expériences de verrouillages et de RIN.

Puisque les mesures de RIN se font dans le régime statique, c'est à dire que le laser suiveur n'est pas modulé, les parasites associés avec le boîtier n'interviennent pas dans les mesures. Par contre, on peut très bien observer la fréquence de résonance naturelle d'un composant et son évolution par rapport au courant de polarisation et au detuning. La figure 4.13 présente les mesures de RIN d'un VCSEL fibré émettant à une longueur d'onde de 1.55μm. Ce VCSEL a été verrouillé pour fonctionner en régime de detuning négatif, ce qui montre des fréquences de résonance pas très élevées et des courbes plutôt amorties.

La figure 4.14, par contre montre les mesures de RIN d'un VCSEL fonctionnant en régime de detuning positif des pics de résonance très prononcés et des courbes non-amorties peuvent être observées.

La figure 4.15 présente la comparaison entre différentes mesures de RIN. Les trois mesures différentes présentent le RIN non-verrouillé, le RIN verrouillé en régime detuning positif et le RIN verrouillé en régime detuning négatif. Les mesures de RIN peuvent être identifiées avec les trois régimes de fonctionnement décrits précédemment . On voit que grace à l'augmentation de la fréquence de relaxation dû au verrouillage le RIN est inférieur à -140dB/Hz sur une plus grande plage de fréquence.

Figure 4.9: Exemple de bruit d'intensité dans un laser modulé.

Figure 4.10: Banc de mesure de RIN de VCSELs non-verrouillés.

Figure 4.11: Mesures de RIN pour un VCSEL émettant à 1.55μm.

4.3 Conclusion and Discussion

Ce chapitre a présenté, dans un premier temps, une méthode pour l'extraction de la réponse S_{21} d'un VCSEL fibré en utilisant la technique de soustraction et un modèle mathématique. Ainsi, les réponses S_{21} ont été extraites pour les VCSELs non-verrouillés émettant à 1.3μm et 1.55μm et pour les VCSELs verrouillés émettant à 1.55μm.

Dans un deuxième temps, les mesures de RIN de VCSELs verrouillés et non-verrouillés ont été présentées. Les fréquences de résonance en fonction du courant de polarisation et de différent régimes de detuning sont étudiées. Une amélioration de RIN d'à peu près 10 dB est présentée pour les VCSELs verrouillés fonctionnant en régime de detuning positif.

Figure 4.12: Banc de mesure de RIN de VCSELs verrouillés.

Figure 4.13: Mesures de RIN d'un VCSEL émettant à 1.55μm fonctionnant en régime de detuning positif.

Figure 4.14: Mesures de RIN d'un VCSEL émettant à 1.55μm fonctionnant en régime de detuning négatif.

Figure 4.15: Comparison entre RIN des VCSELs RayCAn émettant à 1.5μm sous difféérents conditions de fonctionnement. Les trois différents courbes présentent le RIN non-verrouillé, le RIN sous detuning en λ positif et sous detuning en λ négatif.

Conclusion et Perspectives

Les travaux de recherche présentés ont été effectués dans le cadre d'un projet Européen, en partenariat avec l'Ecole Polytechnique Fédérale de Lausanne (EPFL), BeamExpress (un spin-off de l'EPFL) et D-Lightsys, une société Française fabriquant des sous-ensembles optiques [1]. L'objectif de ce projet est la conception des sous-ensembles optiques pour déploiement dans les réseaux haut-débits (10Gbps) en utilisant les VCSEL émettant à 1.3μm et à 1.5μm. Trois rôles distincts, la fabrication, la caractérisation et le développement du produit final ont resectivement été attribués à l'EPFL, à l'ISAE/MOSE et au D-Light Sys. En conséquence les travaux de recherche présentés ici mettent l'accent sur la dimension caractérisation et modélisation numérique du projet.

La partie expérimentale présentée n'a pas de précédent dans le sens que le laboratoire MOSE n'avait pas l'expérience de travailler dans le domaine de verruillage optique quand le projet a démarré au début de l'année 2007. La modélisation mathématique ainsi qu'électronique et la caractérisation des VCSELs ont toujours été un fort de MOSE. C'est pour cette raison que le modèle mathématique du verrouillage optique présenté ici est une extension des modèles développés pour les VCSELs non-verrouillés, au sein de ce laboratoire précédemment [**?**], [**?**], [**?**].

Nous avons présenté un modèle mathématique complet de VCSELs optiquement verrouillés. Les équations d'évolution classiques, décrivant le comportement des VCSELs non-verrouillés, ont été adaptées au verrouillage optique. La réponse S_{21} des VCSELs verrouillés a été simulée sous différentes conditions de fonctionnement. Trois régimes distincts, en fonction de la variation de la puissance optique injectée et le désaccord de fréquence entre le laser maître et le laser suiveur, ont été identifiés.

Les simulations ont été validées par comparaison avec les mesures effectuées. Les résultats expérimentaux ont été obtenues en utilisant des VCSELs en puce ainsi que fibrés. Les fréquences de résonance élevée jusqu'à 16 GHz et les fréquences de coupure jusqu'à 10 GHz ont été observées. Une méthode d'extraction de la réponse du composant des mesures bruitées observées à l'analyseur de réseau vectoriel, a aussi été présentée.

Les mesures de RIN des VCSELs verrouillés et non-verrouillés ont été présentées. Ces

[1] D-Light Sys est depuis racheté par le fabriquant des connecteurs microondes et optiques **Radiall**.

mesures nous ont aidé à étudier l'évolution de la fréquence de relaxation en fonction de variation de detuning entre les deux lasers. Le fonctionnement d'un VCSEL verrouillé en régime de detuning positif (en longueur d'onde) entraîne une amélioration du plancher du bruit en déplaçant le pic de relaxation vers les fréquences plus hautes.

Le verrouillage optique a beaucoup d'applications notamment dans les systèmes de télécommunications, comme il a été démontré par plusieurs équipes de recherche [**?**], [**?**], [**?**], [**?**], [**?**], [**?**]. Mais ces applications ne sont pas limitées au domaine de télécommunications. Le verrouillage optique est utilisé pour la génération des signaux millimétriques [**?**], [**?**], [**?**], [**?**] et pour le traitement optique des signaux [**?**], [**?**], [**?**].

Le verrouillage optique a démontré son utilité dans plusieurs domaines, pourtant cela augmente la complexité des systèmes. Les applications de verrouillage optique seront utilisées quand nous pourrons bénéficier des modules produits en masse peu coûteux. Le développement rapide des VCSEL, qui sont intrinsèquement moins coûteux et plus intégrables que des EELs, est certainement un pas dans la bonne direction. L'émergence des nouvelles technologies d'intégration offrira plus de possibilités de produire des modules des VCSELs verrouillés optiquement intégrés.

List of Publications

Journal Publications

Ahmad Hayat, Alexandre Bacou, Angélique Rissons, Vladimir Iakovlev, Alexei Syrbu, Jean-Claude Mollier and Elie Kapon, "Long-Wavelength VCSEL by VCSEL Optical Injection-Locking", *IEEE Transactions on Microwave Theory and Techniques*, Accepeted for publication.

Alexandre Bacou, Ahmad Hayat, Angélique Rissons, Vladimir Iakovlev, Alexei Syrbu, Jean-Claude Mollier and Elie Kapon, "Optoelectronic T-Matrix Technique Applied to Efficient Deembedding of Intrinsic 1.3μm VCSEL Dynamic Behavior", *IEEE Photonics Technology Letters*, VOL. 21, No. 14, July 15, 2009.

Alexandre Bacou, Ahmad Hayat, Angélique Rissons, Vladimir Iakovlev, Alexei Syrbu, Jean-Claude Mollier and Elie Kapon, "Electrical Modeling of Long-Wavelength VCSELs for Intrinsic Parameters Extraction", *IEEE Jouranl of Quantum Electronics*, Submitted.

International Conferences

Ahmad Hayat, Alexandre Bacou, Angélique Rissons, Jean-Claude Mollier, "2.49GHz Low Phase-Noise Optoelectronic Oscillator using 1.55μm VCSEL for Avionics and Aerospace Applications", *in Proc. SPIE, vol.6908*, (San Jose, CA, USA), SPIE, Jan. 2009.

Ahmad Hayat, Margarita Varon, Alexandre Bacou, Angélique Rissons, Jean-Claude Mollier, "2.49GHz Low Phase-Noise Optoelectronic Oscillator using 1.55μm VCSEL for Avionics and Aerospace Applications", *in International Topical Meeting on Microwave Photonics, 2008. MWP 2008 Proceedings*, Oct. 2008.

Ahmad Hayat, Alexandre Bacou, Angélique Rissons, Jean-Claude Mollier, Vladimir Iakovlev, Alexei Syrbu and Eli Kapon, "1.3μm Single-Mode VCSEL-by-VCSEL Optical Injection-Locking for Enhanced Microwave Performance", *in The 15th Annual Meeting of the IEEE*

Lasers and Electro-Optics Society, LEOS, 2008.

Book Chapters

Ahmad Hayat, Alexandre Bacou, Angélique RISSONS and Jean-Claude MOLLIER, "Optical Injection-Locking: A Technique for VCSEL Operation Enhancement in "Advances in Lasers and Electro-Optics", ISBN 978-953- 7619-X-X.", Accepted for publication in Novemeber 2009.